Forschungszentrum Jülich
in der Helmholtz-Gemeinschaft

The structure of magnetic field in the TEXTOR-DED

K.H. Finken, S.S. Abdullaev, M. Jakubowski,
M. Lehnen, A. Nicolai, K.H. Spatschek

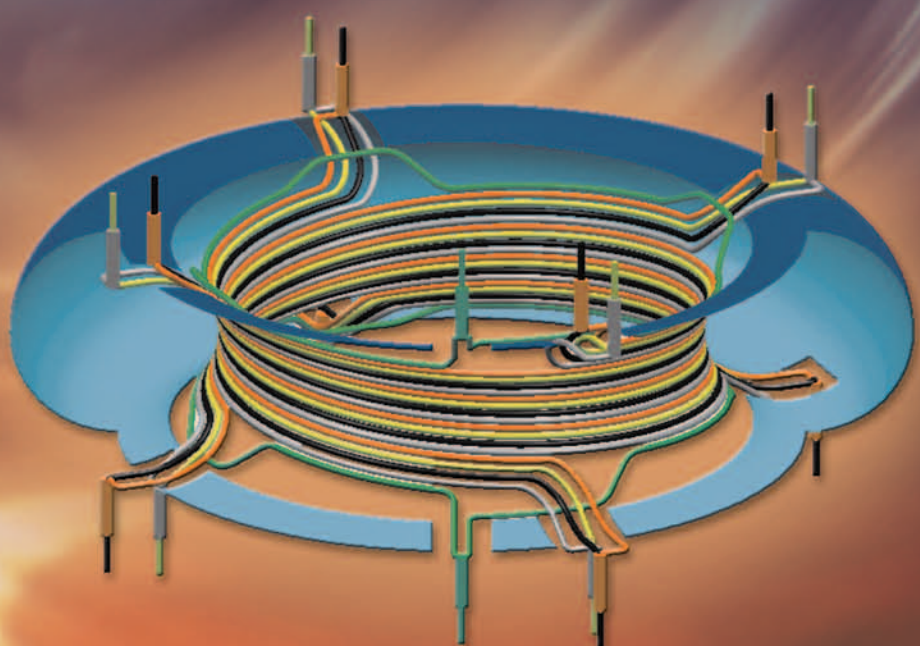

Energietechnik
Energy Technology

Schriften des Forschungszentrums Jülich
Reihe Energietechnik / Energy Technology Band / Volume 45

Forschungszentrum Jülich GmbH
Institut für Plasmaphysik

The structure of magnetic field in the TEXTOR-DED

K.H. Finken, S.S. Abdullaev, M. Jakubowski, M. Lehnen,
A. Nicolai, K.H. Spatschek

Schriften des Forschungszentrums Jülich
Reihe Energietechnik / Energy Technology Band / Volume 45

ISSN 1433-5522 ISBN 3-89336-418-8

Bibliographic information published by Die Deutsche Bibliothek.
Die Deutsche Bibliothek lists this publication in the Deutsche Nationalbibliografie; detailed bibliographic data are available in the Internet at <http://dnb.ddb.de>.

Publisher and Distributor: Forschungszentrum Jülich GmbH
Zentralbibliothek
D-52425 Jülich
Telefon (02461) 61-5368 · Telefax (02461) 61-6103
e-mail: zb-publikation@fz-juelich.de
Internet: http://www.fz-juelich.de/zb

Cover Design: Grafische Medien, Forschungszentrum Jülich GmbH

Printer: Grafische Medien, Forschungszentrum Jülich GmbH

Schriften des Forschungszentrums Jülich
Reihe Energietechnik / Energy Technology Band / Volume 45

ISSN 1433-5522
ISBN 3-89336-418-8

Published in full on the internet
Persistent Identifier: urn:nbn:de:0001-00312
http://nbn-resolving.de/resolver.pl?urn= urn:nbn:de:0001-00312

Abstract

The main component of the Dynamic Ergodic Divertor (DED) consists of a set of coils installed in the TEXTOR tokamak which creates resonant magnetic perturbations, preferentially at the plasma edge. The main purpose of the DED is a study the effect of the magnetic perturbations on the tokamak plasma. In particular, on the transport of the heat and particles to wall, the plasma confinement and rotation. This report is devoted to the systematic theoretical study of magnetic field and its structure in the TEXTOR-DED. It contains the description of the DED coil system in different operational regimes, the magnetic field created by this coil system, the study of formation of chaotic magnetic field lines and the structure of stochastic (ergodic) zone of field lines at the plasma edge and on the divertor plates, determination of field line diffusion coefficients and the Kolmogorov lengths. The modern mapping method for integration of Hamiltonian field line equations is employed for these studies. A description of the numerical Gourdon code to study the ergodic zone of the DED is also given. The experimental observations of the structure magnetic field lines performed recently in the TEXTOR-DED and their comparison with the modelling are also briefly discussed.

Contents

1

Introduction

1.1 Control of the plasma by the edge ergodization

During the last two decades, considerable progress has been made in improving the plasma confinement. The sufficiently low error margin from the different devices makes it now possible to extrapolate the confinement data to a reactor scenario such it can be expected that the plasma of the proposed ITER experiment will most likely ignite. The essential ingredient for a good confinement is the existence of magnetic flux surfaces which form - typically eccentric - onion shell like structures inside the fusion devices. Magnetic field lines stay always on "their" magnetic surface and these surfaces also form isobars.

A key element for obtaining the good plasma confinement quality is the poloidal divertor which allows for a relatively easy access of the high confinement mode (H-mode) of a tokamak. The H-mode operation is considered the standard scenario for ITER. In the H-mode, a barrier is formed at the plasma edge which - together with an observed profile stiffness -leads to the overall improvement of the confinement. However, the confinement in the plasma edge tends to be so good, that new edge instabilities develop, the so called Edge Localized Modes, ELMs. The ELMs affect only the plasma pedestal and therefore at a first glance not harmful with respect of the confinement. However, the ELMs show a sharp rise in the characteristics of ejected energy and particle efflux and a short duration. At present day tokamaks, ELMs are disturbing but not harmful. For ITER, however, the power to the walls is so high that it may determine the lifetime of the device. Recent experiments in the DIII-D tokamak by Evans et.al. (2004, 2005a); Moyer et.al. (2005) show that the ELMs can be eliminated reproducibly in the presence of external resonant magnetic perturbations. This is one of the reasons why ergodicity and ergodic divertors attract recently high attention to the fusion community.

Ergodization of magnetic field lines is used in this context in contrast to "good magnetic surfaces" where a magnetic field line remains on one surface; ergodic magnetic field lines span up a whole volume. In particular, ergodicity

means that any magnetic field line comes infinitely close to any point in an ergodized volume. Ergodization results from perturbations which are resonant to specific values of the safety factor q. When using an external perturbation, one can select whether one ergodizes preferentially the inner surfaces or surfaces closer to the edge. In the first case, the "woven" magnetic field lines form an internal ergodic layer which is typically characterized by an enhanced radial transport of particles and energy. In the second case one generates in addition to the ergodic field lines those which leave the plasma and intersect the walls. These field lines will carry enhanced fluxes of particles and energy to the wall and will lead to areas of enhanced plasma-wall interaction. In this way, an open chaotic system is formed.

The open magnetic field lines, i.e. those which intersect the wall twice, form the so called laminar zone. This zone is equivalent to the scrape-off layer (SOL) of a poloidal divertor; however, in contrast to the conventional SOL, the connection lengths of the magnetic field lines is not uniform but consists of magnetic flux bundles with multiples of a poloidal turn. The investigation of structure of the laminar zone, of the ergodic zone and the consequences for the transport are of particular interest.

Below we give a definitions and fix notations which are used in the main part of the report.

1.2 Description of magnetic field lines

Magnetic field lines in a toroidal system are conveniently presented in a Hamiltonian form. It gives the most convenient way to describe the regular and chaotic field lines in the presence of non–axisymmetric magnetic perturbations. Below we shortly recall this description.

In magnetically confined plasmas, like tokamaks and stellarators, magnetic field lines lie on nested toroidal surfaces, *magnetic surfaces*, wound around a circular closed magnetic field line, *magnetic axis*. The magnetic surfaces are labeled by a so-called *toroidal flux*, $\psi = \psi(x, y, z) = \text{const}$, equal to a magnetic flux through the surface perpendicularly to the magnetic axis where $\psi = 0$. The position of field lines on the magnetic surface is uniquely given by a *poloidal angle*, ϑ, (the short way around the torus) and *toroidal angle*, φ (the long way around the torus).

In terms of toroidal flux ψ, poloidal and toroidal angles ϑ, φ a divergence – free magnetic field $\mathbf{B}$ can be presented in the Clebsch form (see, e.g., Boozer (1983); Balescu (1988); Boozer (1992))

$$\mathbf{B} = \nabla\psi \times \nabla\vartheta + \nabla\varphi \times \nabla H, \tag{1.1}$$

and the equations for magnetic field lines take the Hamiltonian form

$$\frac{d\psi}{d\varphi} = -\frac{\partial H}{\partial \vartheta}, \qquad \frac{d\vartheta}{d\varphi} = \frac{\partial H}{\partial \psi}, \tag{1.2}$$

with (ϑ, ψ) as canonical variables, φ as independent time– like variable, and the function $H = H(\vartheta, \psi, \varphi)$, a *poloidal flux*, plays role of Hamiltonian. It is a $2\pi-$ periodic function of ϑ, φ. The formulation of magnetic field line equations in these variables corresponds to the formulation of Hamiltonian equations in action – angle variables (I, ϑ) [1].

The equilibrium magnetic field configuration with the nested magnetic surfaces, $\psi(x, y, z) =$ constant, the poloidal flux is $H = H(\psi)$, and the field line equations (1.2) are given

$$\psi = \text{const}, \qquad \vartheta = \varphi/q(\psi) + \vartheta_0, \tag{1.3}$$

where

$$q(\psi) = \left(\frac{\partial H_0(\psi)}{\partial \psi}\right)^{-1}$$

is the *safety factor*. The latter has a meaning of the number of turns along the toroidal angle φ per one turn along the poloidal angle ϑ.

In the presence of these non-axisymmetric magnetic perturbation the poloidal flux H can be presented as a sum of the unperturbed flux $H_0(\psi)$ and the perturbed part of the flux $\epsilon H_1 = \epsilon H_1(\psi, \vartheta, \varphi)$ depending on the poloidal and toroidal angles:

$$H = H_0(\psi) + \epsilon H_1(\psi, \vartheta, \varphi), \qquad H_0(\psi) = \int \frac{d\psi}{q(\psi)}. \tag{1.4}$$

The dimensionless perturbation parameter ϵ introduced in (1.4) stands for the relative strength of the magnetic perturbations. Since the perturbed part of Hamiltonian (or the perturbation Hamiltonian) H_1 is a 2π periodic function of ϑ, φ, it can be always presented as Fourier series:

$$H_1(\psi, \vartheta, \varphi) = \sum_{m,n} H_{mn}(\psi) \cos(m\vartheta - n\varphi + \chi_{mn}). \tag{1.5}$$

The integer numbers m and n are called the *poloidal* and *toroidal mode numbers*, respectively, and the constants χ_{mn} represent their phases.

1.3 Onset of ergodic zone of field lines

The qualitative picture of formation of the ergodic zone of magnetic field lines is following. Each harmonics of magnetic perturbations, $H_{mn}(\psi)\cos(m\vartheta - n\varphi + \chi_{mn})$, in Eq. (1.5) destroys the resonant magnetic surface ψ_{mn}, i.e., $q(\psi_{mn}) = m/n$, forming the magnetic island. Its width, $\Delta\psi_{mn}$, is determined by

[1] A definition of action–angle variables can be found in the textbook by Arnold (1989).

$$\Delta\psi_{mn} = 4\left|\frac{\epsilon H_{mn}(\psi)}{dq^{-1}/d\psi}\right|^{1/2}. \tag{1.6}$$

At the sufficiently small level of magnetic perturbation magnetic islands corresponding to the different poloidal mode numbers m are isolated. In this case there exist un-destroyed (non-resonant) magnetic surfaces, located between magnetic islands, which act as transport barriers for magnetic field lines.

With increasing the magnetic perturbation the radial width of islands $\Delta\psi_{mn}$ grow which results in overlapping the neighboring islands at the certain level of magnetic perturbation. It destroys all intact magnetic surfaces between magnetic islands and leads to the global chaos of field lines in a certain region of the plasma. The onset of this region called *ergodic zone* can be established by the qualitative Chirikov's criteria of overlapping resonances, i.e.,

$$\sigma_{Chir} = \frac{\Delta\psi_{mn} + \Delta\psi_{m+1,n}}{2|\psi_{m+1,n} - \psi_{mn}|} \geq 1, \tag{1.7}$$

which means that the average width of neighboring resonances is larger than the distance between corresponding resonance magnetic surfaces.

1.4 The DED and its operational regimes

The Dynamic Ergodic Divertor (DED) is a new set of coils installed in the Jülich tokamak, TEXTOR which creates resonant magnetic perturbations of type (1.5) at the plasma edge. The main purpose of this device is a study the effect of these magnetic perturbations on the tokamak plasma, particularly, on the transport heat and particles to wall, the plasma confinement and rotation.

The DED has been designed such that it can operate in different modes such as static or dynamic, in perturbation modes: $m/n = 12/4$, $m/n = 6/2$ and $m/n = 3/1$:

1. *"12:4" mode.* This *standard operational regime* describes the case when the spectra of magnetic perturbation, $H_{mn}(\psi)$, in Eq. (1.5) contains only on the dominant toroidal mode number $n = 4$ and a group of several poloidal modes m ($10 \leq m \leq 14$) which are resonant near the magnetic surface $q = 3$.
2. *"6:2" mode.* In this regime the toroidal mode is $n = 2$. The ergodic zone may be formed due to overlapping the group of magnetic islands located near the magnetic surface $q = 3$ with poloidal modes $m = 5 \div 8$.
3. *"3:1" mode.* The dominant toroidal mode number is $n = 1$. This operational regime of the DED is employed to study a deep penetration of the perturbed field into the plasma, and associated with this MHD phenomena.

1.5 Goals and a short description of the report

The goal of this report is to describe the magnetic field structure of the TEXTOR–DED. It includes the description of the DED coil system in different operational regimes and the magnetic field created by this coil system, the study of formation of chaotic magnetic field lines, the structure of stochastic (ergodic) zone of field lines at the plasma edge and on the divertor plates. We also briefly discuss the experimental observations of the structure magnetic field lines performed recently in the TEXTOR and their comparison with the modeling.

The content of the report is follow. Chapter 2 is devoted to the description of coil configurations in different operational regimes of DED and analytical calculations of the perturbation magnetic field. A Hamiltonian formulation of the equations for magnetic field lines in a toroidal system is given in Chapter 3. A model for the equilibrium magnetic field and spectra of perturbation magnetic field, a mapping method to integrate the Hamiltonian equations for field lines are also described in this chapter. The structure of ergodic and laminar zones of field lines at the plasma edge and statistical property of chaotic field lines are studied in Chapter 4. Finally, a brief description of the Gourdon code to study the ergodic zone of the DED is given in Chapter 5. Details of some lengthy calculations are prescribed in Appendices A-F.

1.6 Bibliographic notes

The influence of the external resonant helical fields on the tokamak plasma has been first studied in the tokamak PULSATOR (Karger et.al. (1975)). The concept of ergodic divertor (or limiter) has been first proposed by Engelhardt and Feneberg (1978); Feneberg and Wolf (1981); Samain et.al. (1982) to control the plasma edge by creating ergodic magnetic field lines using the external coils. It has been later implemented in several tokamaks, like TEXT (see, Gentle (1981); McCool et.al. (1990)), Tore-Supra (Samain et.al. (1984, 1990); Ghendrih et.al. (1992); Nguyen (1995); de Michelis (1995); Ghendrih et.al. (1996)), JFT-2M (Shoji et.al. (1992); Evans et.al. (1989)), CSTN-II (Takamura et.al. (1987, 1989)), HYBTOK-II (Shen et.al. (1989)), TBR-1 Caldas et.al. (2002), TCABR (Pires et.al. (2005)), and other small fusion devices (Kawamura et. al. (1982); Hattori et.al. (1984)).

The scheme of the TEXTOR-DED has been first proposed by Finken et.al. (1995) (see also a special issue of *Fusion Engineering and Design* edited by Finken (1997)). It started the operation since 2003. It is a first medium size tokamak which has a new feature, namely, beside the conventional concept of the ergodic divertor (or limiter) with a static perturbation field already implemented in the above mentioned tokamaks, the DED also permits operation with a rotating (time–varying) perturbation magnetic field. Previously, such a time–varying perturbations have been studied in small-size tokamaks

CSTN-III (Takamura et.al. (1988)), CSTN-IV (Kobayashi et.al. (2000a,b)) and HYBTOK-II (Kikuchi et.al. (2004)).

External perturbation magnetic fields have been also used in poloidal divertor tokamaks. Particularly the DIII-D tokamak was supplied with external compensating coils (C-coils), installed in 1994, and internal coils (I-coils), installed in 2002-2003. These coils are employed to control resistive wall mode (Okabayashi et.al. (2001); Jackson et.al. (2003); Strait et.al. (2003); Okabayashi et.al. (2004)) and to mitigate the edge localized mode in the H-mode regime of the plasmas (Evans et.al. (2004, 2005a); Moyer et.al. (2005)).

2

DED coil system and magnetic perturbations

2.1 The DED arrangements

The sketch of the DED coils for the two different operational mode, $m : n = 3 : 1$ and $12 : 4$, are shown in Fig. 2.1 (see Finken (1997)). It consists of a quadruple set of four helical conductors, installed on the inboard side of the TEXTOR vessel and aligned parallel to the magnetic field lines (for $\beta_{pol} \sim 1$) at the nearby $q = 3$ surface. The coils are bundled such that the outlets are at 4 toroidal locations, 4 on top of TEXTOR and 4 at the bottom. This grouping of the coils is technically favorable, but it requires the installation of a pair of compensation coils which are indicated in green color. The coils are covered by ceramic tiles and by 2D shaped graphite tiles forming a smooth toroidal surface, the divertor target plate.

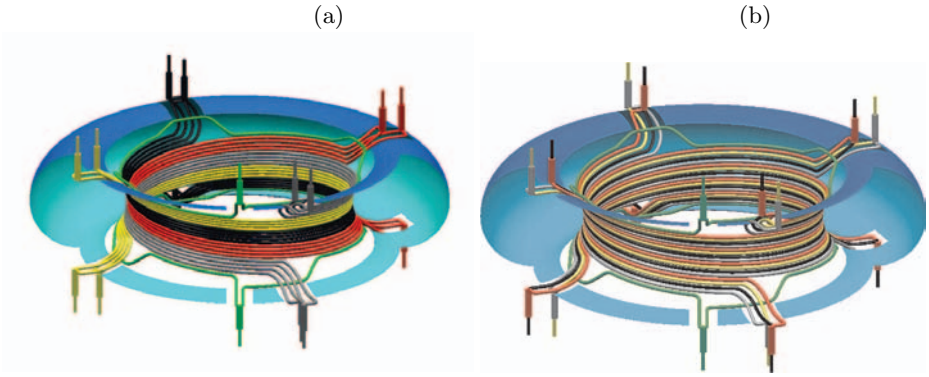

Fig. 2.1. Sketch of the DED coils: a) for the 3:1 mode configuration; b) for the 12:4 mode configuration.

The quadruple set of 16 helical coils are located at the minor radius $r_c = 53.25$ cm. The geometry of coils on the (θ, φ) plane is presented in

Fig. 2.9, where θ is poloidal angle (along a small circumference of the torus) and φ is toroidal angle (along a long circumference of the torus). Coils cover a poloidal section $\Delta\theta \approx 70^\circ$ (including compensation coils $\Delta\theta \approx 80^\circ$). Coils are numbered by j which extends from 1 to 16 as shown on the top of Figure 2.2.

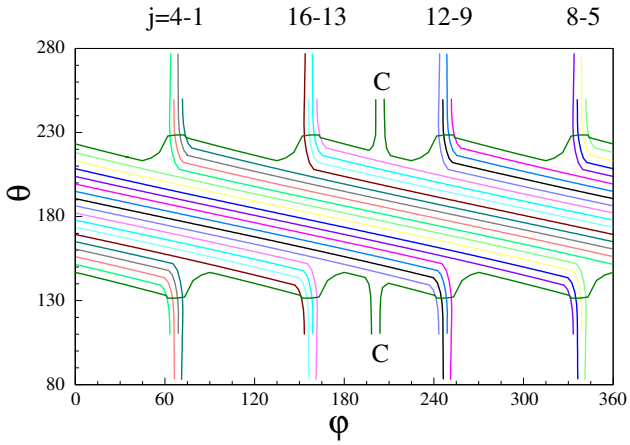

Fig. 2.2. Coil configuration in the (θ, φ) plane.

There are two compensation coils, C, which are switched on during the 12:4 mode operation. These conductors compensate the net perturbation field of $n = 0$ toroidal mode.

In the area covered by coils the poloidal position, θ_j of coils can be described by a linear function of the toroidal angle, φ, i.e.,

$$\theta_j(\varphi) = \theta_{j0} - \frac{\theta_c}{\pi}\varphi \qquad 0 < \varphi < 2\pi, \qquad j = 1, \ldots, 16, \tag{2.1}$$

where $\delta\theta$ is an angular distance between coils, $2\theta_c$ is a poloidal extension of a set of coils, θ_{j0} is a maximum poloidal position of the $j-$ coil, and φ_j is a starting toroidal position of the $j-$ coil.

$$\begin{aligned} \theta_{j0} &= \theta_0 - 4\{(j-1)/4\}\delta\theta, \\ \varphi_j &= \varphi_0 + \frac{\pi}{2}\left[\frac{j-1}{4}\right] (\bmod 2\pi), \qquad j = 1, \ldots, 16, \end{aligned} \tag{2.2}$$

where $\{x\}$ is a fractional part of x ($\{1\} = 0$), $[x]$ is an integer part of x, and θ_0 is a starting poloidal angle of the first coil.

The values of θ_0, $\delta\theta$ and φ_0 are

$$\theta_0 = 224.662^\circ, \qquad \delta\theta = 4.3364^\circ, \qquad \varphi_0 = 337.2^\circ.$$

2.2 Basic distribution of current over coils

We call the following current distribution over coils given by

$$I_j^{(n)} = I_d \sin\left(n\frac{2\pi j}{16} \mp \omega t + \chi_n\right), \qquad (j = 1, 2, \ldots, 16), \tag{2.3}$$

as a *basic current distribution*, where n is the integer number. The quantity I_d stands for the amplitude of current, and ω is a frequency of rotation of the magnetic field perturbation. The sign (-) in Eq. (2.3) describes the co-rotating magnetic field perturbation, while (+) describes the counter-rotating one. In the DC operation $\omega = 0$.

As we will see in Section 2.3.3 such a current distribution creates magnetic perturbations with toroidal mode numbers $\hat{n} = n + 4p$, $(p = 0, 1, 2, \ldots)$. Therefore, the basic current distribution $I_j^{(n)}$ with values of $n = 1, 2, 4$ will create the $3:1$, $6:2$, and $12:4$ operational modes, respectively.

The arbitrary current distribution I_j can be presented as a linear combinations of $I_j^{(n)}$ (2.3):

$$I_j = \sum_n \iota_n I_j^{(n)} = I_d \sum_n \iota_n \sin\left(n\frac{2\pi j}{16} \mp \omega t + \chi_n\right), \qquad j = 1, 2, \ldots, 16. \tag{2.4}$$

Below we consider a several current distribution in the DED coils system. The calculations of the Fourier amplitudes ι_n and the phase χ_n for the different current distributions, I_j, are given in Appendix A.

2.2.1 Current distribution for the 3:1 mode: DC operation

We consider the two kind of current distributions on the DED coils.

The case 1 is given by

$$I_j = I_d \begin{cases} 1, & \text{for } 1 \le j \le 8, \\ -1, & \text{for } 9 \le j \le 12\ . \end{cases} \tag{2.5}$$

In this case the current distribution can be exactly presented as a Fourier series (see Eqs. A.3)

$$I_j = I_d \sum_{l=0}^{3} \iota_{2l+1} \sin\left((2l+1)\frac{2\pi j}{16} + \chi_{2l+1}\right), \qquad 1 \le j \le 16, \tag{2.6}$$

where the coefficients ι_{2l+1} and χ_{2l+1}, $(l = 0, 1, 2, 3)$ are given by

$$\iota_{2l+1} = \frac{1}{4\sin((2l+1)\pi/16)}, \qquad \chi_{2l+1} = -\frac{(2l+1)\pi}{16}. \tag{2.7}$$

The leading term $l = 0$ has the following amplitude and phase

$$\iota_1 = \frac{1}{4\sin(\pi/16)} = 1.28146, \qquad \chi_1 = -\frac{\pi}{16}. \tag{2.8}$$

The case 2 is given by

$$I_j = I_d \begin{cases} 1, & \text{for } 1 \le j \le 4, \\ 0, & \text{for } 5 \le j \le 8 \text{ and } 13 \le j \le 16, \\ -1, & \text{for } 9 \le j \le 12. \end{cases} \tag{2.9}$$

The Fourier coefficients τ_{2l+1} and phases χ_{2l+1} in Eq. (2.6) for this current distribution are

$$\iota_{2l+1} = \frac{\sin((2l+1)\pi/4)}{4\sin((2l+1)\pi/16)}, \qquad \chi_{2l+1} = \frac{\pi}{16}(3-10l). \tag{2.10}$$

Particularly,

$$\iota_1 = \frac{\sin(\pi/4)}{4\sin(\pi/16)} = 0.9061, \qquad \chi_1 = \frac{3\pi}{16}. \tag{2.11}$$

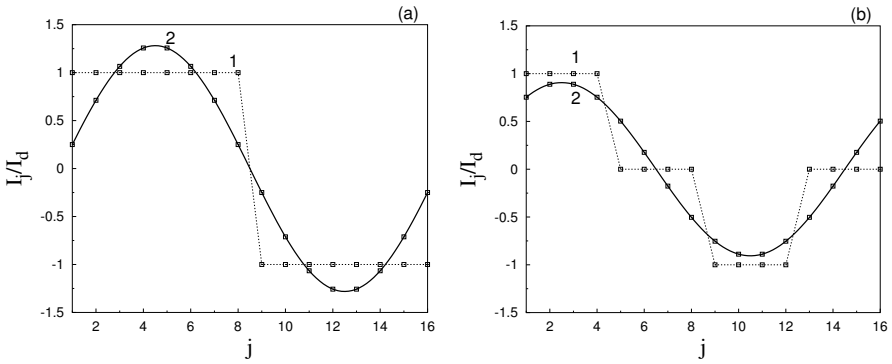

Fig. 2.3. A current distribution over coils (curve 1). The smooth curve 2 corresponds to the first term $n = 1$ in Eq. (2.6): (a) corresponds to the case 1; (b) − the case 2.

The first term with $l = 0$ in (2.6) is responsible for the generation of magnetic perturbation with the toroidal modes $\hat{n} = (2l+1) = 1, 5, 9, \ldots$, the second term with $l = 1$ − for toroidal modes $\hat{n} = 3, 7, 11, \ldots$, the third term with $l = 2$ − for toroidal modes $\hat{n} = 5, 9, 13, \ldots$, and the last term with $l = 3$ − for toroidal modes $\hat{n} = 7, 11, 15, \ldots$.

2.2.2 Current distribution for the 3:1 mode: AC operation

In this case the current distribution is given by

$$I_j = I_d \begin{cases} \sin\omega t, & \text{for } 1 \le j \le 4, \\ \sin(\omega t + \pi/2), & \text{for } 5 \le j \le 8, \\ \sin(\omega t + \pi), & \text{for } 9 \le j \le 12\ , \\ \sin(\omega t + 3\pi/2), & \text{for } 13 \le j \le 16. \end{cases} \tag{2.12}$$

It can be presented as

$$I_j = I_d \sum_{l=0}^{3} \iota_{4l+1} \sin\left((4l+1)\frac{2\pi j}{16} \mp \omega t + \chi_{4l+1}\right), \quad (1 \le j \le 16), \tag{2.13}$$

where

$$\iota_{4l+1} = (-1)^l \frac{\sin[(4l+1)\pi/4]}{4\sin[(4l+1)\pi/16]},$$

$$\chi_{4l+1} = -\frac{\pi}{16}(4l+5), \qquad l = 0, 1, 2, 3. \tag{2.14}$$

For the leading coefficients ι_1 and χ_1 we have

$$\iota_1 = \frac{\sin[\pi/4]}{4\sin[\pi/16]} = 0.9061, \qquad \chi_1 = -\frac{5\pi}{16}. \tag{2.15}$$

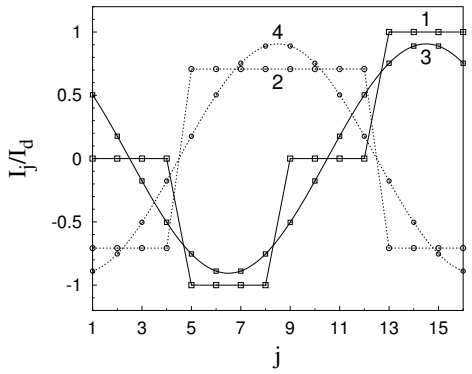

Fig. 2.4. A current distribution over coils in the 3:1 mode in the AC operation at different phases ωt: curve 1 corresponds to $\omega t = \pi$; curve 2 – $\omega t = -\pi/4$. Curves 3 and 4 describe the first terms $n = 1$ in Eq. (2.13) with the phases $\omega t = \pi$ and $\omega t = -\pi/4$, respectively.

The distribution (2.12) and the first term in Eq. (2.13) are plotted in Fig. 2.4 for the two values of the phase ωt: curve 1 corresponds to $\omega t = \pi$; curve 2 – $\omega t = -\pi/4$; curves 3 and 4 describe the first terms $s = 0$ in Eq. (2.13) with the phases $\omega t = \pi$ and $\omega t = -\pi/4$, respectively.

One should note that the ratio of the leading amplitudes, ι_1, corresponding to the DC operation with the current distribution (2.5) and AC operation with Eq. (2.12) is

$$\frac{\iota_1(DC)}{\iota_1(AC)} = \frac{1}{\sin[\pi/4]} = \sqrt{2} = 1.4142. \tag{2.16}$$

2.2.3 A coil configuration for the 6:2 mode: DC operation

The case 1. In this case the current distribution is following (see Fig. 2.5a)

$$I_j = I_d \begin{cases} 1, & \text{for } j = 1,2,7,8,9,10,15,16, \\ -1, & \text{for } j = 3,4,5,6,11,12,13,14\ . \end{cases} \tag{2.17}$$

This distribution is given by a sum

$$I_j = I_d \left[\iota_2 \sin\left(\frac{\pi j}{4} + \chi_2\right) + \iota_4 \sin\left(\frac{3\pi j}{4} + \chi_6\right)\right], \quad (1 \le j \le 16), \tag{2.18}$$

where

$$\begin{aligned} \iota_2 &= \frac{1}{2\sin(\pi/8)} = 1.30656; & \chi_2 &= 19\pi/8 \equiv 3\pi/8, \\ \iota_6 &= \frac{1}{2\sin(3\pi/8)} = 0.5411961; & \chi_6 &= 41\pi/8 \equiv 9\pi/8. \end{aligned}$$

The case 2. Current distribution on coils (see Figure 2.5b) is given by

$$I_j = I_d \begin{cases} 1, & \text{for } j = 4,5,12,13, \\ 0, & \text{for } j = 2,3,6,7,10,11,14,15, \\ -1, & \text{for } j = 1,8,9,16\ . \end{cases} \tag{2.19}$$

It can be presented as a sum

$$I_j = I_d \left[\iota_2 \sin\left(\frac{\pi j}{4} + \chi_2\right) + \iota_6 \sin\left(\frac{3\pi j}{4} + \chi_6\right)\right], \qquad 1 \le j \le 16, \tag{2.20}$$

where

$$\begin{aligned} \iota_2 &= -\sin(3\pi/8) = -0.92387953, & \chi_2 &= 3\pi/8, \\ \iota_6 &= \sin(9\pi/8) = -0.38268343, & \chi_6 &= \pi/8. \end{aligned}$$

The first term in Eq. (2.20) generates a magnetic perturbation with toroidal modes $\hat{n} = 2, 6, \ldots$, while the second term $-\ \hat{n} = 6, 10, \ldots$.

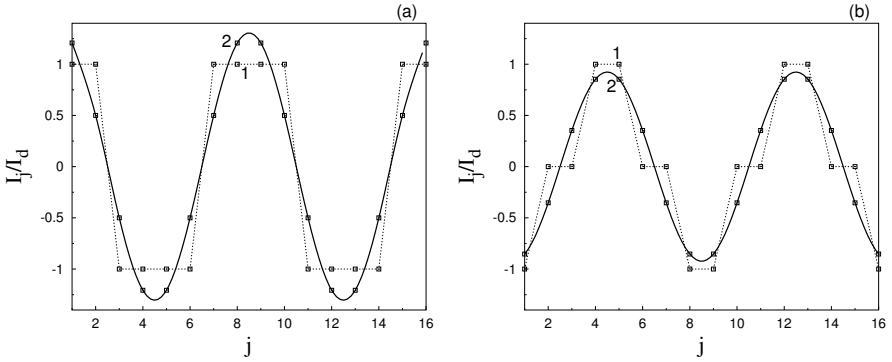

Fig. 2.5. A current distribution over coils (2.19) (curve 1). The smooth curve 2 describes the first term in Eq. (2.20): a) Case 1, b) case 2.

2.2.4 A coil configuration for the 6:2 mode: AC operation

Current distribution on coils is given by

$$I_j = I_d \begin{cases} \sin\omega t, & \text{for } j = 1,2,9,10, \\ \sin(\omega t + \pi/2), & \text{for } j = 3,4,11,12\ , \\ \sin(\omega t + \pi), & \text{for } j = 5,6,13,14\ , \\ \sin(\omega t + 3\pi/2), & \text{for } j = 7,8,15,16\ . \end{cases} \tag{2.21}$$

For this case the current is presented as a sum

$$I_j = I_d \left[\iota_2 \sin\left(\frac{\pi j}{4} + \omega t + \chi_2\right) + \iota_{10} \sin\left(\frac{5\pi j}{4} + \omega t + \chi_{10}\right)\right], \quad (1 \le j \le 16), \tag{2.22}$$

where

$$\iota_2 = \cos\left(\frac{\pi}{8}\right), \qquad \chi_2 = -\frac{3\pi}{8},$$
$$\iota_{10} = \cos\left(\frac{5\pi}{8}\right), \qquad \chi_{10} = -\frac{15\pi}{8}.$$

The distribution (2.21) and the first term in Eq. (2.22) are plotted in Fig. 2.6 for the two values of the phase ωt: curve 1 corresponds to $\omega t = 0$; curve 2 – $\omega t = 3\pi/4$; curves 3 and 4 describe the first terms in Eq. (2.22) with the phases $\omega t = 0$ and $\omega t = 3\pi/4$, respectively.

In the 6:2 mode the ratio of leading amplitudes ι_2, corresponding to the DC operation with Eq. (2.17) and AC operation with Eq. (2.21) is

$$\frac{\iota_2(DC)}{\iota_2(AC)} = \frac{1}{\sin[\pi/4]} = \sqrt{2} = 1.4142, \tag{2.23}$$

which coincides with the corresponding ratio (2.16) for the 3:1 mode.

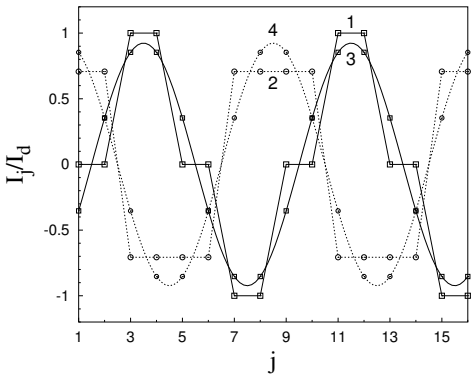

Fig. 2.6. A current distribution over coils in the 6:2 mode in the AC operation at different phases ωt: curve 1 corresponds to $\omega t = 0$; curve 2 – $\omega t = 3\pi/4$. Curves 3 and 4 describe the first terms in Eq. (2.22) with the phases $\omega t = 0$ and $\omega t = 3\pi/4$, respectively.

2.2.5 A coil configuration for the 12:4 mode: DC operation

The current distribution on coils for this operational mode is given by

$$I_j = I_d \begin{cases} -1, & \text{for } j = 1,4,5,8,9,12,13,16, \\ 1, & \text{for } j = 2,3,6,7,10,11,14,15. \end{cases} \tag{2.24}$$

One can show that this distribution can be exactly presented as

$$I_j = I_d \iota \sin\left(j\frac{\pi}{2} + \chi\right), \qquad (1 \le j \le 16)$$
$$\iota = 2\sin(\pi/4) = \sqrt{2}, \qquad \chi = \frac{5\pi}{4}, \tag{2.25}$$

which generates magnetic perturbations with $\hat{n} = 4, 8, \ldots$. The distribution (2.24) is plotted in Fig. 2.7.

2.2.6 A coil configuration for the 12:4 mode: AC operation

In this case we have the following current distribution:

$$I_j = I_d \begin{cases} \sin\omega t, & \text{for } j = 1,5,9,13, \\ \sin(\omega t + \pi/2), & \text{for } j = 2,6,10,14\ , \\ \sin(\omega t + \pi), & \text{for } j = 3,7,11,15\ , \\ \sin(\omega t + 3\pi/2), & \text{for } j = 4,8,12,16\ . \end{cases} \tag{2.26}$$

Such a distribution is presented by only one term,

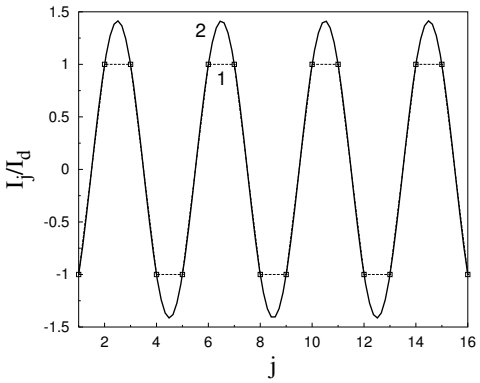

Fig. 2.7. A current distribution over coils (2.24) (curve 1) and the sinusoidal distribution (2.25) (a smooth curve 2).

$$I_j = I_d \sin\left(\frac{\pi(j-1)}{2} + \omega t\right), \qquad 1 \le j \le 16. \tag{2.27}$$

The distribution (2.27) is plotted in Fig. 2.8 for the two values of the phase ωt: curve 1 corresponds to $\omega t = 0$; curve 2 – $\omega t = 5\pi/4$.

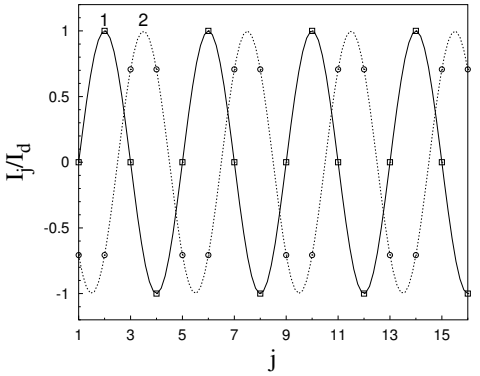

Fig. 2.8. A current distribution over coils in the 12:4 mode in the AC operation at different phases ωt: curve 1 corresponds to $\omega t = 0$; curve 2 – $\omega t = 5\pi/4$.

In this mode the ratio of amplitudes ι, corresponding to the DC operation and AC operation coincides with the corresponding ratios (2.16) for the 3:1 and 6:2 modes, i.e.,

$$\frac{\iota(DC)}{\iota(AC)} = \sqrt{2}. \tag{2.28}$$

2.3 Density of DED current

It is convenient to introduce the density of DED perturbation currents in order to find the magnetic perturbations. The current density $\mathbf{j}(r,\theta,\varphi)$ is introduced as

$$\mathbf{j} = j_r\mathbf{e}_r + j_\theta\mathbf{e}_\theta + j_\varphi\mathbf{e}_\varphi, \tag{2.29}$$

where $\mathbf{e}_r, \mathbf{e}_\theta, \mathbf{e}_\varphi$ are unit vectors along the coordinates r, θ, φ, respectively. The corresponding components, j_r, j_θ, and j_φ, are defined as

$$(j_r, j_\theta, j_\varphi) = (0, j(r,\theta,\varphi)\sin\alpha_0, j(r,\theta,\varphi)\cos\alpha_0),$$

where

$$j(r,\theta,\varphi) = \delta(r-r_c)\sum_{j=1}^{16} I_j r_c^{-1}\delta(\theta-\theta_j(\varphi)), \tag{2.30}$$

and $\alpha_0 = \theta_c r_c/\pi R_c$ is an angle between current direction and toroidal axis φ, $\theta_j(\varphi)$ is a poloidal position of the $j-$th coil at the toroidal section φ.

For the basic coil distributions (2.3), Eq. (2.30) may be written as

$$j^{(n)}(r,\theta,\varphi) = \delta(r-r_c)g(\theta,\varphi)\frac{I_d}{r_c}\sum_{j=-\infty}^{\infty}\sin\left(n\frac{2\pi j}{16}+\chi_n\right)\delta\Big(\theta-\theta_j(\varphi)\Big), \tag{2.31}$$

where $g(\theta,\varphi)$ is a step function equal to 1 in the area covered by coils and zero elsewhere (see Eqs. (2.37), (2.44)).

Using the properties of the delta function, $\delta(x)$, the current density (2.31) can be transformed the sum of continuous distributions (see Section B.1 in Appendix B)

$$j^{(n)}(r,\theta,\varphi) = \delta(r-r_c)g(\theta,\varphi)J_0 \times\sum_{s=-\infty}^{\infty}\cos\left(\frac{m_0(16s-n)}{4}\theta+\frac{n_0(16s-n)}{4}\varphi+\chi_s^{(n)}\right), \tag{2.32}$$

where

$$\chi_s^{(n)} = -\frac{m_0(16s-n)}{4}\theta_0+\chi_n-\frac{\pi}{2}. \tag{2.33}$$

In (2.32) the following notations are introduced:

$$J_0 = \frac{I_d}{\delta\theta r_c} = \frac{2m_0 I_d}{\pi r_c},$$
$$m_0 = \frac{\pi}{2\delta\theta}, \qquad n_0 = \frac{m_0\theta_c}{\pi} = \frac{\theta_c}{2\delta\theta}, \qquad \theta_0 = \theta_{01}+\delta\theta. \tag{2.34}$$

The angle θ_{01} is a poloidal position of the first coil at the toroidal section $\varphi = 0$.

Because of periodicity of $J(\theta, \varphi)$ along φ with a period 2π follows that n_0 must be an integer number equal to $n_0 = 4l$, where $l = 1, 2, \ldots$. Putting $n_0 = 4$, the term $s = 0$ in Eq. (2.32) which gives the main contribution the perturbed magnetic field in the plasma can be presented as

$$j_0^{(n)}(r,\theta,\varphi) = \delta(r-r_c)g(\theta,\varphi)J_0 \cos\left(\frac{nm_0}{4}\,\theta + n\varphi - \chi_0^{(n)}\right) = \mathrm{Re}\tilde{j}^{(n)}(r,\theta,\varphi),$$

$$\tilde{j}^{(n)}(r,\theta,\varphi) = \delta(r-r_c)g(\theta,\varphi)J_0 e^{i\left(\frac{nm_0}{4}\,\theta + n\varphi - \chi_0^{(n)}\right)}. \tag{2.35}$$

2.3.1 Fourier expansion of the current density

For calculations of the magnetic field created by helical coils it is convenient to present the current density $j_0^{(k)}(r,\theta,\varphi)$ in Fourier series in θ, φ:

$$\tilde{j}^{(n)}(r,\theta,\varphi) = \sum_{m,\hat{n}} j_{m\hat{n}}(r) e^{i(m\theta + \hat{n}\varphi + \chi_{m\hat{n}})}$$

$$j_{m\hat{n}}(r)e^{i\chi_{m\hat{n}}} = \delta(r-r_c)e^{-i\chi_0^{(n)}}\frac{J_0}{(2\pi)^2}\int_0^{2\pi}\int_0^{2\pi} d\theta d\varphi g(\theta,\varphi) e^{-i(m-\frac{nm_0}{4})\theta - i(\hat{n}-n)\varphi}. \tag{2.36}$$

The content of Fourier spectrum, $j_{mn}(r)$, depends on the function $g(\theta, \varphi)$ which determined by the coil configurations. The ideal and real configurations of coils are shown in Fig. 2.9. Below we consider these cases separately.

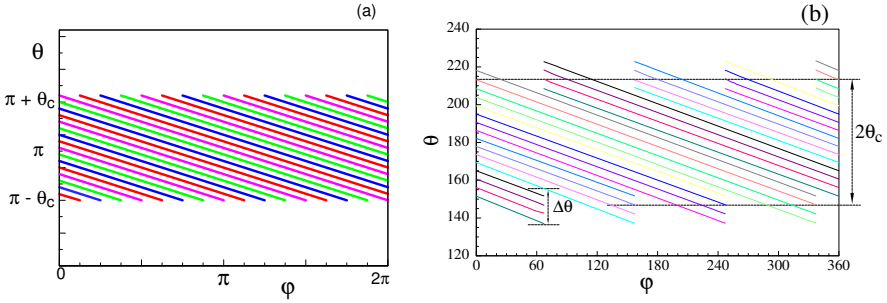

Fig. 2.9. Models of the DED coil configuration: (a) ideal configuration, (b) real configuration.

2.3.2 Ideal coil configuration

For the ideal coil configuration (see Figure 2.9a) the function $g(\theta,\varphi)$ is a is given by:

$$g(\theta,\varphi)=\begin{cases}1 & \text{for } \pi-\theta_c<\theta<\pi+\theta_c,\\ 0 & \text{otherwise.}\end{cases} \tag{2.37}$$

The current density (2.32) can be presented as a Fourier series:

$$j^{(n)}(r,\theta,\varphi)=J_0\delta(r-r_c)\sum_{m=-\infty}^{\infty}\sum_{s=-\infty}^{\infty}g_m^{(s)}\cos\left[m\theta+(16s-n)\varphi+\chi_{ns}\right], \tag{2.38}$$

where

$$g_m^{(s)}=(-1)^m\frac{\sin([m-m_0(4s-n/4)]\theta_c)}{[m-m_0(n/4-4s)]\pi}, \tag{2.39}$$

$$\chi_{ns}=\chi_s^{(n)}+\pi\frac{m_0(16s-n)}{4}=\frac{m_0(16s-n)}{4}(\pi-\theta_0)+\chi_n-\frac{\pi}{2}. \tag{2.40}$$

The main contribution to the magnetic field comes from the term $s=0$ which can be rewritten as (by changing the summation over m to $-m$)

$$j_0^{(n)}(r,\theta,\varphi)=J_0\delta(r-r_c)\sum_{m=-\infty}^{\infty}g_m\cos\left(m\theta+n\varphi+\bar{\chi}_{n0}\right), \tag{2.41}$$

where

$$g_m\equiv g_m^{(0)}=(-1)^m\frac{\sin[(m-m_0n/4)\theta_c]}{(m-m_0n/4)\pi}, \tag{2.42}$$

$$\bar{\chi}_{n0}=-\chi_{n0}=\frac{m_0n}{4}(\pi-\theta_0)-\chi_n+\frac{\pi}{2}. \tag{2.43}$$

2.3.3 Non-ideal coil configuration

For the non-ideal configuration of coils (see Figure 2.9b) the step function $g(\theta,\varphi)$ should be replaced by

$$g(\theta,\varphi)=\begin{cases}1, & \text{for } \pi-\theta_c(\varphi)<\theta<\pi+\theta_c(\varphi),\\ 0, & \text{elsewhere,}\end{cases} \tag{2.44}$$

where

$$\theta_c(\varphi)=\theta_{c0}-\frac{2\Delta\theta}{\pi}(\varphi-\varphi_l)\qquad\text{for } \varphi_l<\varphi<\varphi_{l+1}, \tag{2.45}$$

and

$$\varphi_l = \varphi_c + (l-1)\frac{\pi}{2}, \qquad 0 < \varphi_c < \frac{\pi}{2}, \qquad l = 0, 1, 2, 3, 4. \tag{2.46}$$

For the sake of simplicity we consider the term $s = 0$ in Eq. (2.32), i.e., Eq. (2.35). One can show that (see Section B.2 in Appendix B)

$$j_0^{(n)}(\theta, \varphi) = \sum_{m=-\infty}^{\infty} \sum_{s=-\infty}^{\infty} J_{m,s} \cos(m\theta + (4s+n)\varphi + \chi_{ms}). \tag{2.47}$$

The Fourier coefficients, $J_{m,0}$, corresponding to the term $s = 0$ which gives the main contribution to the perturbed field is given by

$$J_{m,0} = J_0 g_m C_m, \qquad \chi_{m0} = \frac{m_0 n}{4}(\pi - \theta_0) - \chi_n + \frac{\pi}{2}, \tag{2.48}$$

where g_m is defined by Eq. (2.42), and

$$C_m = \frac{\sin[(m - nm_0/4)\Delta\theta/2]}{(m - nm_0/4)\Delta\theta/2}$$

is a correction factor due to non-ideal configuration. For the ideal configuration $\Delta\theta = 0$ and therefore $C_m = 1$.

As was shown in Section B.2 that in the case $n = 4$ it appears the components of helical current distributions with the toroidal mode number $\hat{n} = 0$ which may disturb the plasma equilibrium. These components are compensated using the currents on the compensation coils.

2.4 Magnetic field perturbations

In this section we present the formulae for the magnetic field created by the surface current (2.29). Each term in the Fourier expansion (2.47) of this perturbation current describes a helical current on the toroidal surface of radius $r = r_c$. Consider a single helical current vector $\boldsymbol{j}_{mn}$ corresponding to the (m, n) mode

$$\begin{aligned} \boldsymbol{j}_{mn}(r, \theta, \varphi) &= \delta(r - r_c) j_{mn} \boldsymbol{e}_{mn} \cos(m\theta + n\varphi + \phi_{mn}), \\ \boldsymbol{e}_{mn} &= \Big(0,\ \boldsymbol{e}_\theta \sin\alpha_{mn},\ \boldsymbol{e}_\varphi \cos\alpha_{mn}\Big), \end{aligned} \tag{2.49}$$

where $\boldsymbol{e}_\theta$ and $\boldsymbol{e}_\varphi$ are unit vectors along the poloidal and toroidal directions, respectively, and $\alpha_{mn} = nr_c/mR_c$ is a helicity, i.e., the angle between a helical current direction and toroidal axis.

The total DED current (2.29) can be presented as a sum of helical currents (2.49), i.e.,

$$\boldsymbol{j}_h(r,\theta,\varphi) = \sum_{mn} \boldsymbol{j}_{mn}(r,\theta,\varphi). \tag{2.50}$$

with the same toroidal components of the vector $\boldsymbol{j}_{mn}$ but different poloidal components, i.e.,

$$\begin{aligned} j_{mn}\cos\alpha_{mn} &= J_{m,(n-k)/4}\cos\alpha_0, \\ j_{mn}\sin\alpha_{mn} &\neq J_{m,(n-k)/4}\sin\alpha_0. \end{aligned}$$

For the coefficients j_{mn} and the phases, phi_{mn}, of the helical current we have

$$j_{mn} = \frac{J_{m,(n-k)/4}\cos\alpha_0}{\cos\alpha_{mn}}, \qquad \phi_{mn} = \chi_{m,(n-k)/4}. \tag{2.51}$$

The difference between $\boldsymbol{j}_h(r,\theta,\varphi)$ (2.50) and $\boldsymbol{j}(r,\theta,\varphi)$ (2.29) can be neglected, since the sum of differences of poloidal modes is negligible small, i.e.,

$$\begin{aligned} &\sum_{m=-\infty}^{\infty} \left(j_{mn}\sin\alpha_{mn} - J_{m,(n-k)/4}\sin\alpha_0\right) \\ &= \sum_{m=-\infty}^{\infty} J_{m,(n-k)/4}\frac{\sin(\alpha_0-\alpha_{mn})}{\cos\alpha_{mn}} \approx 0. \end{aligned} \tag{2.52}$$

2.4.1 Cylindrical approximation

Here we consider the magnetic field created by a single component of the helical current $\boldsymbol{j}_{mn}(r,\theta,\varphi)$ (2.49) in a cylindrical geometry. The magnetic field $\mathbf{B}$ of this helical current can be expressed by the scalar potential $\Phi(r,\theta,\varphi)$ ($\mathbf{B} = \nabla\Phi(r,\theta,\varphi)$) (see e.g., Morozov and Solovev (1966))

$$\Phi = \begin{cases} a^i I_m\left(\frac{nr}{R_c}\right)\sin(m\theta + n\varphi + \phi_{mn}), & \text{for } r < r_c, \\ a^e K_m\left(\frac{nr}{R_c}\right)\sin(m\theta + n\varphi + \phi_{mn}), & \text{for } r > r_c, \end{cases} \tag{2.53}$$

where $I_m(z)$ and $K_m(z)$ are modified Bessel functions (see Appendix C). Coefficients a^i, a^e are found by the boundary conditions at the $r = r_c$:

$$B_r\Big|_{r=r_c-0} - B_r\Big|_{r=r_c+0} = 0,$$

$$B_\theta\Big|_{r=r_c-0} - B_\theta\Big|_{r=r_c+0} = \mu_o j_{mn}\cos(m\theta + n\varphi + \phi_{mn})\cos\alpha_{mn}.$$

Using the relations in Eqs. (2.51) we have

$$a^i = -\mu_\circ J_{m,(n-k)/4} r_c \cos\alpha_o K'_m\left(\frac{nr_c}{R_c}\right).$$

Further we consider only the leading terms $s = 0$ (2.48) for helical currents. For them we have the following formula for the scalar potential $\Phi(r, \theta, \varphi)$ of the magnetic field created by a set of helical currents (2.50) inside the toroidal surface $r < r_c$:

$$\Phi(r, \theta, \varphi) = \sum_m \Phi_{mn}(r) \cos(m\theta + n\varphi + \chi_{m0}),$$
$$\Phi_{mn}(r) = -B_c C_m g_m f_{mn}(r) \frac{r_c}{m}, \tag{2.54}$$

where a quantity

$$B_c = \frac{\mu_\circ I_d m_0 \cos\alpha_0}{\pi r_c} \tag{2.55}$$

is the characteristic value of the DED magnetic field perturbation.

For the DED-TEXTOR parameters, r_c = 53.25 cm, R_c = 130 cm, $m_0 \approx 20$, I_d = 15 kA and n= 4 the value of B_c is 0.22535 T (or 2253.5 G).

The radial dependence of magnetic perturbations is described by the function $f_{mn}(r)$:

$$f_{mn}(r) = -\frac{2nr_c}{R_c} K'_m\left(\frac{nr_c}{R_c}\right) I_m\left(\frac{nr}{R_c}\right). \tag{2.56}$$

This function and its radial derivative have the following asymptotics at $r < r_c$ (see Eq. C.1 in Appendix C)

$$f_{mn}(r) \approx \left(\frac{r}{r_c}\right)^m, \qquad f'_{mn}(r) \approx \frac{m}{r_c}\left(\frac{r}{r_c}\right)^{m-1}. \tag{2.57}$$

The radial magnetic field $B_r(r, \theta, \varphi)$ is given by

$$B_r(r, \theta, \varphi) = \frac{\partial \Phi}{\partial r} = \sum_m B_{mn}(r) \sin(m\theta + n\varphi + \chi_{mn}), \tag{2.58}$$

where

$$B_{mn}(r) = -B_c C_m g_m \frac{r_c}{m} \frac{df_{mn}(r)}{dr} \approx -B_c C_m g_m \left(\frac{r}{r_c}\right)^{m-1}. \tag{2.59}$$

The φ-component of the vector potential A_φ related the magnetic field as

$$B_r(r, \theta, \varphi) = \frac{1}{r}\frac{\partial A_\varphi}{\partial \theta}, \qquad B_\theta(r, \theta, \varphi) = -\frac{\partial A_\varphi}{\partial r}, \tag{2.60}$$

is determined by

$$A_\varphi(r, \theta, \varphi) = \sum_m A_{mn}(r) \cos(m\theta + n\varphi + \chi_{mn}), \tag{2.61}$$

where

$$A_{mn}(r) = -m^{-1} r B_{mn}(r) \approx B_c C_m g_m \frac{r_c}{m}\left(\frac{r}{r_c}\right)^m.$$

2.4.2 Toroidal corrections

According to Ref. Morozov and Solovev (1966) the effect of toroidicity on the magnetic field can be taken into account, multiplying the scalar potential $\Phi(r,\theta,\varphi)$ by a factor $\sqrt{R_0/R}$, if the small corrections $(n_0 r_c/2R_0)^{m+3}$ are neglected for each poloidal component m. In this approximations we have

$$\Phi(r,\theta,\varphi) = \sqrt{\frac{R_0}{R_0 + r\cos\theta}} \sum_m \Phi_{mn}(r,\theta)\cos(m\theta + n\varphi + \chi_{m0}), \quad (2.62)$$

where the amplitudes $\Phi_{mn}(r,\theta)$ are given by Eq. (2.54). Then, one can show that the vector potential $A_\varphi(r,\theta,\varphi)$ is determined by

$$\begin{aligned} A_\varphi(r,\theta,\varphi) &= \epsilon B_0 R_0 a(r,\theta,\varphi), \\ a(r,\theta,\varphi) &= \sum_m a_{mn}(r,\theta)\cos(m\theta + n\varphi + \chi_{m0}), \end{aligned} \quad (2.63)$$

where ϵ is a *dimensionless perturbation parameter* defined by

$$\epsilon = \frac{B_c}{B_0}, \quad (2.64)$$

B_0 is the toroidal magnetic field at the center of torus R_0, and

$$\begin{aligned} a_{mn}(r,\theta) &= -\frac{1}{B_c R_0}\frac{r}{m}\frac{\partial}{\partial r}\left(\sqrt{\frac{R_0}{R}}\Phi_{mn}(r)\right) \\ &\approx C_m g_m \frac{r_c}{mR_0}\left(\frac{r}{r_c}\right)^m \sqrt{\frac{R_0}{R_0 + r\cos\theta}}\left(1 - \frac{r\cos\theta}{2m(R_0 + r\cos\theta)}\right). \end{aligned} \quad (2.65)$$

For the radial component of the magnetic field, $B_r(r,\theta,\varphi)$, we have

$$\begin{aligned} B_r(r,\theta,\varphi) &= \frac{1}{r}\frac{\partial A_\varphi(r,\theta,\varphi)}{\partial\theta} = \sum_m B_{mn}(r,\theta)\sin(m\theta + n\varphi + \chi_{m0}), \\ B_{mn}(r,\theta) &\approx B_c C_m g_m \left(\frac{r}{r_c}\right)^{m-1} \sqrt{\frac{R_0}{R_0 + r\cos\theta}}\left(1 - \frac{r\cos\theta}{2m(R_0 + r\cos\theta)}\right). \end{aligned} \quad (2.66)$$

The examples of spatial dependence of the perturbation field are shown in Figs. 2.10a-c and 2.11a-c. Particularly, contour plots of $B_r(r,\theta,\varphi)$ in the (θ, r) plane at the fixed toroidal section φ = constant are plotted in Figs. 2.10a-c for the three operational mode $m:n$, 3:1, 6:2, and 12:4, respectively. The poloidal variation $B_r(r,\theta,\varphi)$ at the fixed radius r and toroidal angle φ are plotted in 2.11a-c. The perturbation DED current is taken I_d=15 kA.

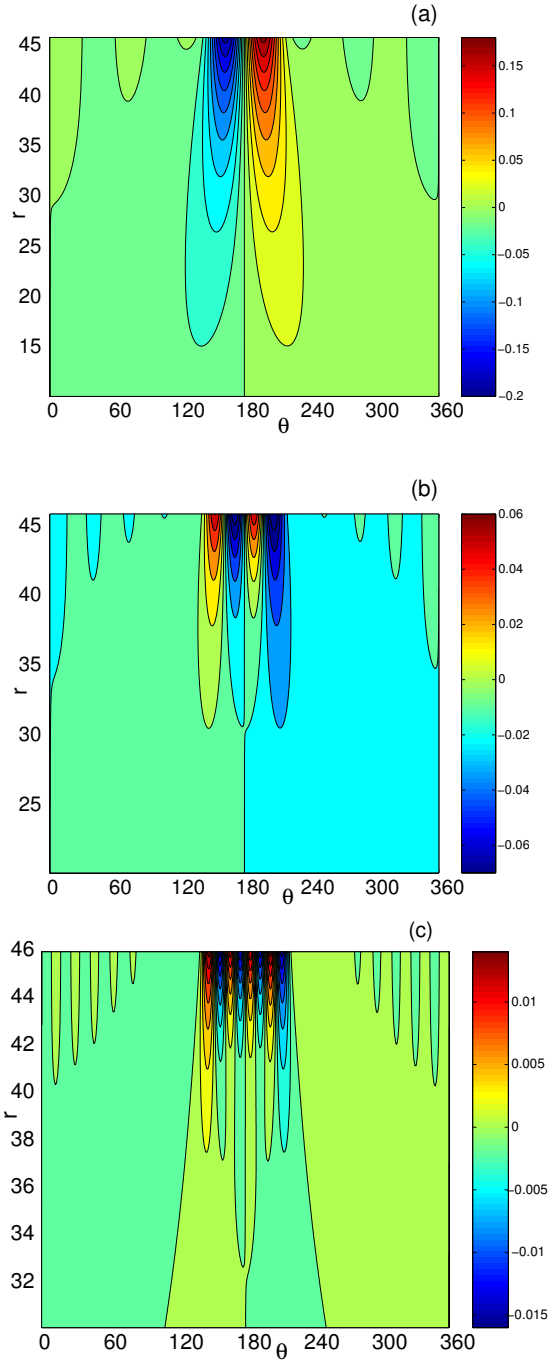

Fig. 2.10. Contour plot of the radial magnetic field perturbation $B_r(r, \theta, \varphi)$ in (θ, r) plane at the cross section $\varphi = 204.4°$: a) the $m : n = 3 : 1$ mode operation; b) $m : n = 6 : 2$ mode; c) $m : n = 12 : 4$ mode. The perturbation DED current is I_d=15 kA.

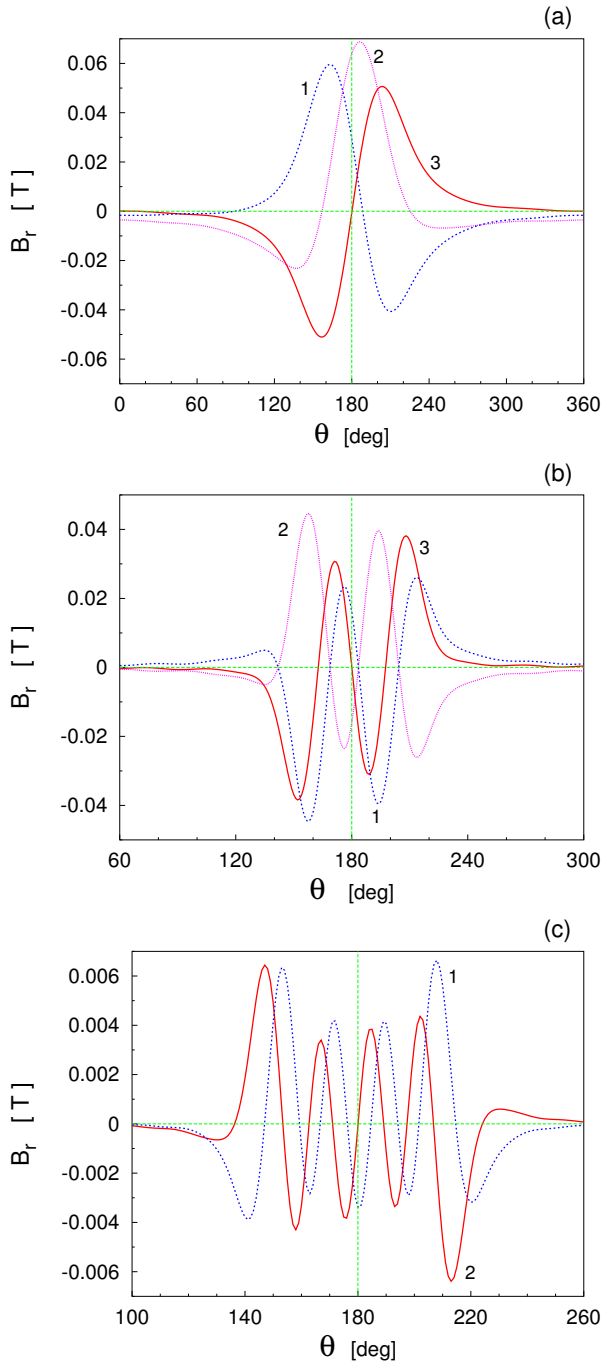

Fig. 2.11. Poloidal dependence of the magnetic field perturbation $B_r(r, \theta, \varphi)$ at the given radial coordinate r and at several the cross sections: a) $m : n = 3 : 1$ mode, $r = 30$ cm: curve 1 – $\varphi = 0°$, curve 2 – $\varphi = 90°$, curve 3 – $\varphi = 204.4°$; b) $m : n = 6 : 2$ mode, $r = 43$ cm: curve 1 – $\varphi = 0°$, curve 2 – $\varphi = 90°$, curve 3 – $\varphi = 204.4°$; c) the $m : n = 12 : 4$ mode, $r = 43$ cm: curve 1 – $\varphi = 0°$, curve 2 – $\varphi = 204.4°$. The perturbation DED current is I_d=15 kA.

3

Hamiltonian field line equations in a toroidal system and the field lines mapping

In a study of field lines the most important is the fact that a divergence free magnetic field is equivalent to Hamiltonian system with $1+1/2$ degrees of freedom (see, e.g., Cary and Littlejohn (1983); Boozer (1983); Morrison (2000)). In this section, first, we shall give a Hamiltonian formulation of magnetic field line equations in a toroidal system, the mapping method to integrate field line equations. Then the spectra of magnetic perturbations in the TEXTOR–DED will be analyzed using some analytical models of the equilibrium magnetic field.

3.1 Hamiltonian formulation of field line equations in a toroidal system

Consider a cylindrical coordinate system (R, φ, Z) where R is a major radius, φ is a toroidal angle, and Z is a vertical coordinate. Field line equations in this coordinate system is given by

$$\frac{1}{R}\frac{dZ}{d\varphi} = \frac{B_Z}{B_\varphi}, \qquad \frac{1}{R}\frac{dR}{d\varphi} = \frac{B_R}{B_\varphi}. \tag{3.1}$$

The magnetic field components B_R, B_φ, B_Z can be determined by the vector potential $\mathbf{A}$: $\mathbf{B} = \nabla \times \mathbf{A}$.

The coordinates (R, φ, Z) are related to the toroidal coordinates (r, θ, φ) as

$$R = R_0 + r\cos\theta, \qquad Z = r\sin\theta. \tag{3.2}$$

Field line equations can be also formulated in a Hamiltonian form. We choose the radial component of the vector potential, A_R, to be zero, i.e., $A_R = 0$, because of a gauge invariant of the vector potential, and suppose that the $z-$ component of the vector potential A_Z which determines the toroidal field $B_\varphi = -\partial A_Z/\partial R$ be in form $A_Z = -B_0 R_0/R$, i.e., $B_\varphi = B_0 R_0/R$, where

B_0 is a strength of magnetic field at the major radius of torus $R = R_0$. We also assume that the equilibrium poloidal magnetic field of the plasma (B_R, B_Z) and the perturbed magnetic field created by the external coils may completely be described by the toroidal component of the vector potential $A_\varphi(R, \varphi, Z)$:

$$B_Z = \frac{1}{R}\frac{\partial(RA_\varphi)}{\partial R}, \qquad B_R = -\frac{\partial A_\varphi}{\partial Z}. \tag{3.3}$$

Introducing the normalized coordinate z and the canonical momentum p_z as

$$z = \frac{Z}{R_0}, \qquad p_z = \ln\frac{R}{R_0},$$

one transforms the equations (3.1) into Hamiltonian form

$$\frac{dz}{d\varphi} = \frac{\partial H}{\partial p_z}, \qquad \frac{dp_z}{d\varphi} = -\frac{\partial H}{\partial z}, \tag{3.4}$$

where the Hamiltonian function $H = H(z, p_z, \varphi)$ is normalized φ- component of the vector potential, i.e.,

$$H \equiv H(z, p_z, \varphi) = \frac{R(p_z)A_\varphi(R(p_z), \varphi, zR_0)}{B_0 R_0^2}, \tag{3.5}$$

where $R = R_0 \exp(p_z)$.

3.2 Field lines in axisymmetric tokamak equilibrium

In the axisymmetric case the magnetic field does not depend on the toroidal angle φ: $A_\varphi = A_\varphi(R, Z)$, and thus $H = H(z, p_z)$. In this case the Hamiltonian system (3.4) is completely integrable. The field lines lie on the nested toroidal surfaces, determined by the surface function $H(z, p_z) = f(Z, R) = \text{const}$. The section of a toroidal surface with the plane $\varphi = \text{const}$ is shown in Figure 3.1. One can introduce the action–angle variables (I, ϑ):

$$I = \frac{1}{2\pi}\oint_C p_z dz, \qquad \vartheta = \frac{\partial}{\partial I}\int^z p_z(z', I)dz', \tag{3.6}$$

where the integration is taken along the closed contour C consisting of cross–section of the surface function $f(R, Z)$ =const with the poloidal plane $\varphi =$ const (see Figure 3.1). The action variable I coincides with the normalized toroidal flux ψ:

$$I = \frac{1}{2\pi}\oint_C p_z dz = \frac{1}{2\pi}\int_S dp_z dz$$
$$= \frac{1}{2\pi R_0^2 B_0}\int_S B_\varphi(R, Z)dRdZ = \psi, \tag{3.7}$$

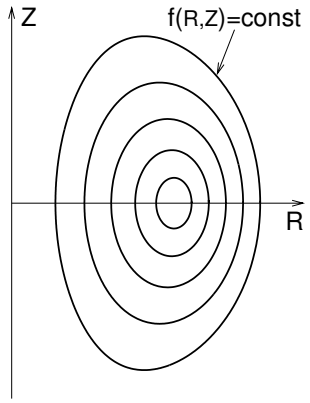

Fig. 3.1. Magnetic flux surfaces $H(z, p_z) = f(Z, R) = \text{const}$.

which has a meaning of the normalized flux of the toroidal field B_φ through the area S enclosed by the closed contour C on the poloidal plane $\varphi = \text{const}$. The angle variable ϑ is no more than the *intrinsic poloidal angle*.

In the action–angle variables (ψ, ϑ) the Hamiltonian $H = H(\psi)$ and the field lines are determined by Eq. (1.3). The inverse *safety factor* $q(\psi)$ is determined by $dH(\psi)/d\psi$. It can be also found from the equation of field lines (3.4). According to the definition of q it is equal to the number of toroidal turns per one poloidal turn, i.e., $q = \Delta\varphi/2\pi$, where $\Delta\varphi$ is the increment of the toroidal angle φ when field line make one full poloidal turn. Then from the first equation (3.4) it follows that

$$q(\psi) = \frac{\Delta\varphi}{2\pi} = \int\limits_C \frac{dz}{\partial H/\partial p_z}, \tag{3.8}$$

where the integral is taken along the closed contour C of $H = H_0(z, p_z) = \text{const}$.

The geometrical coordinates (R, Z) (or (r, θ)) of field lines are periodic functions of the angle variable ϑ: $R(\vartheta, \psi) = R(\vartheta + 2\pi, \psi)$, $Z(\vartheta, \psi) = Z(\vartheta + 2\pi, \psi)$, and they can be presented by Fourier series:

$$Z(\vartheta, \psi) = \sum_m Z_m(\psi) e^{im\vartheta}, \qquad R(\vartheta, \psi) = \sum_m R_m(\psi) e^{im\vartheta}, \tag{3.9}$$

or

$$r(\vartheta, \psi) = \sum_{m=0}^{\infty} \left(r_m^{(c)}(\psi) \cos m\vartheta + r_m^{(s)}(\psi) \sin m\vartheta \right),$$
$$\theta(\vartheta, \psi) = \vartheta + \sum_{m=0}^{\infty} \alpha_m(\psi) \sin m\vartheta. \tag{3.10}$$

The coefficients $R_m(\psi), Z_m(\psi)$ (or $r_m^{(c,s)}(\psi)$, $\alpha_m(\psi)$) depending on a toroidal flux ψ can be found by integrating of Hamiltonian field line equations (3.4). The field lines $R(\varphi), Z(\varphi)$ [or $r(\varphi), \theta(\varphi)$] in real geometrical space (R, Z) or (r, θ) are determined by Eqs. (3.9), (3.10), respectively, by taking the intrinsic poloidal angle, ϑ, as $\vartheta = \varphi/q(\psi) + \vartheta_0$.

3.2.1 Non–axisymmetric magnetic perturbations

In the presence of non-axisymmetric magnetic perturbations the toroidal component of the vector potential $A_\varphi^{(per)}(R, Z, \varphi)$ can be presented as a sum:

$$A_\varphi = A_\varphi^{(0)}(R, Z) + A_\varphi^{(per)}(R, Z, \varphi). \tag{3.11}$$

In typical situations the perturbed part of the component A_Z is small and it can be neglected in comparison with the unperturbed part $A_Z^{(0)}(R)$ which determines the toroidal magnetic field B_φ. Then the magnetic perturbation $\mathbf{B}^{(per)}(R, Z, \varphi)$ has only two nonzero components B_R and B_Z which, according to (3.3), are expressed via the perturbed part of the vector potential $A_\varphi^{(per)}(R, Z, \varphi)$:

$$\mathbf{B}^{(per)}(R, Z, \varphi) = \left(-\mathbf{e}_R \frac{1}{R}\frac{\partial}{\partial Z} + \mathbf{e}_Z \frac{1}{R}\frac{\partial}{\partial R}\right) R A_\varphi^{(per)}(R, Z, \varphi). \tag{3.12}$$

For the DED magnetic perturbations $A_\varphi^{(per)}(R, Z, \varphi)$ is given by Eqs. (2.63), (2.65).

Introducing the toroidal flux ψ and the intrinsic poloidal angle ϑ (3.6) (or the action – angle variables) for the equilibrium magnetic field, the Hamiltonian equations for perturbed field lines (1.2), (1.5) can be presented as

$$\frac{d\vartheta}{d\varphi} = \frac{1}{q(\psi)} + \epsilon\frac{\partial H_1}{\partial \psi}, \qquad \frac{d\psi}{d\varphi} = -\epsilon\frac{\partial H_1}{\partial \vartheta}, \tag{3.13}$$

with the perturbed Hamiltonian $\epsilon H_1 \equiv H_1(\psi, \vartheta, \varphi)$ given by

$$H_1(\psi, \vartheta, \varphi) = \frac{R(\psi, \vartheta)}{R_0^2 B_0} A_\varphi^{(per)}\left(R(\psi, \vartheta), Z(\psi, \vartheta), \varphi\right), \tag{3.14}$$

where $R(\psi, \vartheta) = R_0 + r(\psi, \vartheta)\cos\theta(\psi, \vartheta)$. For the perturbation magnetic field given by Eq. (2.63) it has the following Fourier expansion:

$$H_1(\psi, \vartheta, \varphi) = \epsilon \sum_m H_{mn}(\psi)\cos(m\vartheta + n\varphi + \chi_{m0}), \tag{3.15}$$

where the dimensionless perturbation parameter ϵ is given by Eq. (2.64), and according to (2.63) the Fourier components $H_{m,n}(\psi)$ are given by the integrals:

$$H_{mn}(\psi) = \mathrm{Re}\iint_0^{2\pi} \frac{R(\psi, \vartheta)}{(2\pi)^2 R_0^2 B_0 \epsilon} A_\varphi^{(per)}\left(R(\psi, \vartheta), Z(\psi, \vartheta), \varphi\right) e^{-im\vartheta - in\varphi} d\vartheta d\varphi$$

$$= \mathrm{Re} \iint_0^{2\pi} \frac{R(\psi,\vartheta)}{(2\pi)^2 R_0} a\left(r(\psi,\vartheta),\theta(\psi,\vartheta),\varphi\right) e^{-im\vartheta - in\varphi} d\vartheta d\varphi. \tag{3.16}$$

Note that $H_{mn}(\psi)$ does not depend on the perturbation parameter, ϵ, i.e., on the amplitude perturbation current I_d.

Asymptotical behavior of H_{mn} and their numerical determination shall be studied in Section 3.5.3.

3.2.2 Perturbation field in intrinsic coordinates

One can also expand the perturbed magnetic field, $\mathbf{B}^{(per)}$ the in a Fourier expansion with respect to the intrinsic poloidal angle, ϑ, and the toroidal angle, φ, similar to the expansion of the perturbation Hamiltonian H_1 given by Eq. (3.15), i.e.,

$$\mathbf{B}^{(per)}(\psi,\vartheta,\varphi) = \sum_m \mathbf{B}_{mn}(\psi)\sin(m\vartheta + n\varphi + \chi_{m0}). \tag{3.17}$$

Often one uses the Fourier components, $\mathbf{B}_{mn}(\psi)$, to estimate the width of magnetic islands formed in the presence of magnetic perturbations.

The relation between the Fourier components of the perturbation Hamiltonian, $H_{mn}(\psi)$, and the perturbation field, $\mathbf{B}_{mn}(\psi)$ can be found using Eqs. (3.12) and (3.14). Supposing that $|dH_{mn}/d\psi| \ll m|H_{mn}|$, one obtains

$$|\mathbf{B}_{mn}(\psi)| \approx \epsilon m H_{mn}(\psi) B_0 = m H_{mn}(\psi) B_c. \tag{3.18}$$

3.3 Mappings of field lines

In the mapping approach to integrate the Hamiltonian system (1.4) (1.5), and (3.13) one wishes to avoid small time–step integration replacing it by return mappings of variables (ϑ,ψ) to a certain poloidal section of torus $\varphi = \varphi_k$. Below we define a mapping of field lines in a toroidal system. To be more general we consider the case when a toroidal mode number n take values proportional to a certain number N ($N \geq 1$) which corresponds to the $N-$ fold symmetry of magnetic perturbation along the toroidal angle φ, i.e., $n = sN$, ($s = \pm 1, \pm 2, \dots$). *Let (ϑ_k, ψ_k) be the poloidal angle and toroidal flux* at the poloidal sections $\varphi = \varphi_k = 2\pi k/N$, ($k = 0, \pm 1, \pm 2, \dots$) as illustrated in Fig. 3.2a. We define the map

$$(\vartheta_{k+1}, \psi_{k+1}) = \hat{M}(\vartheta_k, \psi_k), \tag{3.19}$$

which relates the variables (ϑ,ψ) at the successive sections φ_k and φ_{k+1}. Then the map $(\hat{M})^N$ defines Poincaré return map. The flux-preserving property of the mapping (3.19) is expressed by

$$\left|\frac{\partial(\vartheta_{k+1},\psi_{k+1})}{\partial(\vartheta_k,\psi_k)}\right| = 1. \tag{3.20}$$

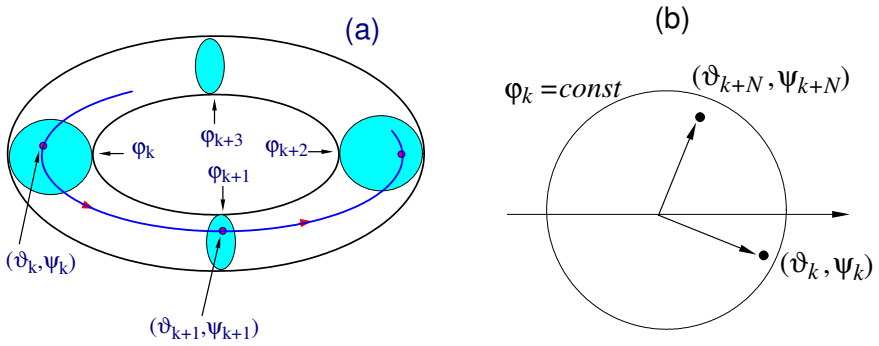

Fig. 3.2. Geometry of mapping in a toroidal system: a) Scheme of the mapping along the toroidal angle; b) Poincaré return map of field lines on the poloidal plane φ_k = const.

3.3.1 The Hamilton–Jacobi method to construct mappings

Symplectic mapping method for integrating Hamiltonian system (1.2), (1.4), (1.5) based on the Hamilton–Jacobi method and perturbation theory has been developed in Refs. by Abdullaev et.al. (1999); Abdullaev (1999, 2002, 2004). The general form of the mapping (3.19) for the Hamiltonian system (1.4), (1.5) is given by the following symmetric flux-preserving form (see Abdullaev (2002)):

$$\Psi_k = \psi_k - \epsilon\frac{\partial S^{(k)}}{\partial\vartheta_k}, \qquad \Theta_k = \vartheta_k + \epsilon\frac{\partial S^{(k)}}{\partial\Psi_k}, \tag{3.21}$$

$$\Psi_{k+1} = \Psi_k, \qquad \bar{\Theta}_k = \Theta_k + w(\Psi_k,\epsilon)(\varphi_{k+1}-\varphi_k), \tag{3.22}$$

$$\psi_{k+1} = \Psi_{k+1} + \epsilon\frac{\partial S^{(k+1)}}{\partial\vartheta_{k+1}}, \quad \vartheta_{k+1} = \bar{\Theta}_k - \epsilon\frac{\partial S^{(k+1)}}{\partial\Psi_{k+1}}, \tag{3.23}$$

where $w(\Psi,\epsilon) = \partial\mathcal{H}/\partial\Psi$ is the frequency of perturbed motion, and $S^{(k)} \equiv S(\vartheta_k,\Psi_k)$ is the value of the generating function $G(\vartheta,\Psi,\varphi,\varphi_0;\epsilon)$ taken at sections $\varphi = \varphi_k$, i.e., $S(\vartheta_k,\Psi_k) = G(\vartheta_k,\Psi_k,\varphi_k,\varphi_0;\epsilon)$. The generating function obeys the Hamilton-Jacobi equation,

$$H\left(\Psi + \epsilon\frac{\partial G}{\partial\vartheta},\vartheta,\varphi\right) + \epsilon\frac{\partial G}{\partial\varphi} = \mathcal{H}(\Psi,\epsilon), \tag{3.24}$$

in the finite interval $\varphi_k < \varphi < \varphi_{k+1}$ and satisfying the condition $G|_{\varphi=\varphi_0} = 0$ at the initial value φ_0 ($\varphi_k < \varphi_0 < \varphi_{k+1}$).

In the first order of ϵ the frequency $w(\Psi, \epsilon)$ is determined by the inverse safety factor $q(\Psi)$:

$$w(\Psi, \epsilon) = \frac{1}{q(\Psi)}, \tag{3.25}$$

and the generating function $G(\vartheta, \Psi, \varphi, \varphi_0)$ in the finite interval $\varphi_{k+1} < \varphi < \varphi_k$ is given by Abdullaev (2002):

$$G(\vartheta, \Psi, \varphi, \varphi_0) = -(\varphi - \varphi_0) \sum_{m,n} H_{mn}(\Psi)$$
$$\times \left[a(x_{mn}) \sin(m\vartheta - n\varphi + \chi_{mn}) + b(x_{mn}) \cos(m\vartheta - n\varphi + \chi_{mn}) \right], \tag{3.26}$$

where

$$a(x) = \frac{1 - \cos x}{x}, \qquad b(x) = \frac{\sin x}{x},$$
$$x_{mn} = \left(\frac{m}{q(\Psi)} - n \right) (\varphi - \varphi_0).$$

The free parameter φ_0 lies in the interval $\varphi_k \le \varphi_0 \le \varphi_{k+1}$.

The mapping (3.21) can be also considered as the alternative method of the symplectic integration of Hamiltonian systems (1.4), (1.5). As was shown in Abdullaev (2002) this map with large integration steps, $\Delta\varphi = \varphi_{k+1} - \varphi_k$, comparable with the characteristic periods of the system (e.g., a perturbation period) has the same accuracy as the conventional symplectic integrators (see, for example, a review Sanz-Serna (1992)) with integration steps two or three orders smaller. The mapping can be applied to Hamiltonian systems with moderately large perturbation $\epsilon \sim 1$ by taking the mapping step $\Delta\varphi = \varphi_{k+1} - \varphi_k$ sufficiently small.

The mapping (3.21) is called *symmetric* if the free parameter is taken exactly in the middle of the interval $[\varphi_k, \varphi_{k+1}]$, i.e., $\varphi_0 = (\varphi_k + \varphi_{k+1})/2$. In the cases when $\varphi_0 = \varphi_k$ (or $\varphi_0 = \varphi_{k+1}$) the mappings have nonsymmetric form (*nonsymmetric maps*). As was shown in Ref. Abdullaev (2002) the symmetric map is more accurate that than the nonsymmetric maps.

3.3.2 Mapping with a numerical interpolation of Hamiltonian

The mapping method requires the knowledge of the safety factor $q(\psi)$ and the perturbation Hamiltonian $H_1(\psi, \vartheta, \varphi)$ or its Fourier coefficients $H_{mn}(\psi)$. Analytical determination of these functions for realistic magnetic configurations is somehow difficult. In order to apply mapping procedure in these cases one can calculate these functions by the numerical integration of the equations of field lines (3.4) on a grid of magnetic flux ψ: $\psi_i = i\Delta\psi$, ($i = 1, \ldots, N_\psi$). The

functions $q(\psi)$, $H_{mn}(\psi)$ for the arbitrary values of ψ can be interpolated by the cubic splines using their pre-calculated values $q(\psi_i)$, $H_{mn}(\psi_i)$.

In order to display the orbits in real space coordinates $\mathbf{x}$ the relations of these coordinates with the variables (ψ, ϑ) can be found during the numerical integration of the equations of field lines in the absence of magnetic perturbations. For instance, the relation between toroidal coordinate (r, θ, φ), (r is a minor radius, θ is a geometrical poloidal angle, different from ϑ) and (ψ, ϑ) can be sought in the form of Fourier series

$$r = r_0 + \sum_m \left(r_m^{(s)}(\psi) \sin m\vartheta + r_m^{(c)}(\psi) \cos m\vartheta \right),$$

$$\theta = \vartheta + \sum_m \alpha_m(\psi) \sin m\vartheta.$$

The Fourier coefficients $r_m^{(s)}(\psi)$, $r_m^{(s)}(\psi)$, and $\alpha_m(\psi)$ can be also calculated numerically for the same grid coordinates of ψ, and their values for arbitrary ψ can be interpolated by the cubic splines.

The described procedure replaces the equations of field lines (3.4) by the Hamiltonian ones (1.2), (1.4), (1.5) which allows to integrate them using the symplectic mapping instead of integrating the equations of field lines (3.4) using the standard, usually, non-symplectic numerical integration schemes.

3.4 Models for the tokamak magnetic equilibrium

3.4.1 Equilibrium magnetic field with the Shafranov shift

As a model for the equilibrium magnetic field we will consider the tokamak plasma with nested, circular magnetic surfaces. The model takes into account the outward (Shafranov) shift of magnetic surfaces due to effects of the plasma pressure and electric current. Schematically it is shown in Fig. 3.3. Here $R_0(\rho)$ is the position of the center of the magnetic surface of radius ρ, and a is a radius of the the last magnetic surface. The shift of $R_0(\rho)$ with respect $R_0(a)$ is denoted $\Delta(\rho)$, i.e., $\Delta(\rho) = R_0(\rho) - R_0(a)$. This quantity is known as the *Shafranov shift*. The Shafranov shift $\Delta(\rho)$ of the magnetic surface of radius ρ is given by (see Ref. Nguyen (1995))

$$\Delta(\rho) = \left[R_0^2(a) + (\Lambda + 1) \left(a^2 - \rho^2 \right) \right]^{1/2} - R_0(a), \tag{3.27}$$

where $\Lambda = \beta_{pol} + l_i/2 - 1$. Here, β_{pol} is the ratio of the plasma pressure, $\langle p \rangle$ to the magnetic pressure, $B_\theta^2/8\pi$ of the poloidal field B_θ:

$$\beta_{pol} = \frac{8\pi \langle p \rangle}{B_\theta^2},$$

l_i is the internal inductance. We consider low β and large aspect-ratio tokamak plasma, and describe its equilibrium field with the following vector potential

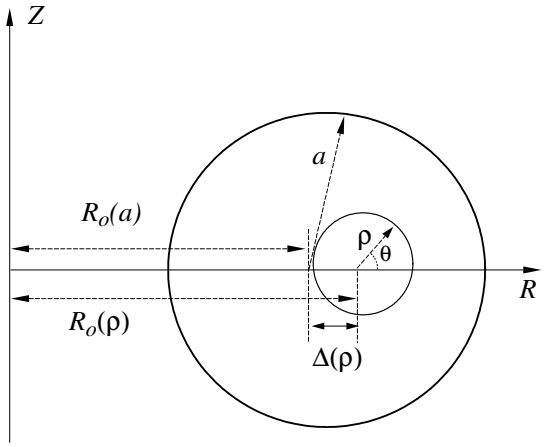

Fig. 3.3. Shifted magnetic flux surfaces in a toroidal plasma.

$$\begin{aligned} \mathbf{A} &= (0, A_\varphi(r,\theta), A_z(r,\theta))\,, \\ A_\varphi(r,\theta) &= \frac{B_0}{R}\int \frac{d\psi}{q\,(\rho(\psi))}, \\ A_z(r,\theta) &= -B_0 R_0 \ln(R/R_0). \end{aligned} \tag{3.28}$$

In (3.28) R is a major radius of torus, related with the coordinates (r,θ): $R = R_0 + r\cos\theta$, B_0 is a toroidal magnetic field at the center of torus R_0. The quantity $q(\rho)$ is a safety factor as a function of radius of magnetic surface ρ, which is related to the normalized toroidal magnetic flux. Using the definition of the toroidal flux (3.7) one can show that for the toroidal field, $B_t = B_0 R_0/R$, the normalized toroidal flux, ψ, is determined by

$$\psi = \frac{R_p(\rho)}{R_p(a)}\left[1 - \left(1 - \frac{\rho^2}{R_p^2(\rho)}\right)^{1/2}\right] \approx \frac{\rho^2}{2R_p^2}. \tag{3.29}$$

The relation between the radius ρ of magnetic surface and the cylindrical coordinates (R,Z) is $\rho = \sqrt{(R - R_p(a) - \Delta(\rho))^2 + Z^2}$. The toroidal, B_φ, and poloidal, B_θ, magnetic fields corresponding to Eq. (3.28) are

$$\begin{aligned} B_\varphi(r,\theta) &= \frac{B_0 R_0}{R}, \\ B_\theta(r,\theta) &= \frac{B_0}{qR}\frac{d\psi}{d\rho}\frac{1}{1+\Delta'(\rho)\cos\bar{\theta}} \approx \frac{B_0\rho}{qR}\frac{1}{1+\Delta'(\rho)\cos\bar{\theta}}, \end{aligned} \tag{3.30}$$

where $\bar{\theta} = \sin^{-1}(Z/\rho)$.

3.4.2 The safety factor profiles

Here we present the profiles of the safety factor, $q(\rho)$, for a several models of the plasma with a circular cross–section.

Cylindrical approximation

In a cylindrical plasma model the safety factor profile is fully determined by the toroidal current density profile of the plasma, $j(\rho)$. According to Ampère's law

$$B_\theta = \frac{\mu_o I(\rho)}{2\pi\rho} = \frac{\mu_o}{2\pi\rho}\int\limits_0^\rho j(\rho')d\rho', \tag{3.31}$$

where $I(\rho)$ is a current flowing inside the magnetic surface of radius ρ. Then according to definition

$$q_{cyl}(\rho) = \frac{\rho B_0}{R B_\theta} = \frac{2\pi\rho^2 B_0}{\mu_o R_0 I(\rho)}. \tag{3.32}$$

At the plasma edge, $\rho = a$, the value of the safety factor is determined by the total plasma current $I_p = I(a)$, i.e.,

$$q_a = q_{cyl}(a) = \frac{2\pi a^2 B_0}{\mu_o R_0 I_p}. \tag{3.33}$$

Consider a simple model for $q(\rho)$. For a large aspect–ratio circular plasma the toroidal current density is modeled as

$$j(\rho) = j_0\left(1-\rho^2/a^2\right)^\nu, \tag{3.34}$$

which gives

$$I(\rho) = I_p\left[1-\left(1-\rho^2/a^2\right)^{\nu+1}\right], \qquad I_p = \frac{\pi j_0 a^2 \mu_0}{\nu+1},$$
$$q_{cyl}(\rho) = q_a \frac{\rho^2/a^2}{1-(1-\rho^2/a^2)^{\nu+1}}. \tag{3.35}$$

For this model of the plasma the value of the safety factor at the magnetic axis, $q(0)$, is determined by q_a and the parameter ν: $q(0) = q_a/(\nu+1)$.

Toroidal corrections

The safety factor given by Eq. (3.32) is valid only for the cylindrical plasma column. For a toroidal plasma the $q-$profile differs from (3.32). It should approach to the cylindrical approximation in the limit of large aspect–ratio

$R/r \gg 1$. We find a corrections to the safety factor due to toroidicity for the simple model of the plasma. We consider the plasma equilibrium with the following poloidal and toroidal fields:

$$B_\theta = \frac{\mu_o I(\rho)}{2\pi\rho}\left(1 + \Lambda\frac{\rho}{R}\right),$$
$$B_\varphi = \frac{B_0 R_0}{R} = \frac{B_0 R_0}{R_p(\rho)\left(1 + \rho/R_p(\rho)\cos\bar{\theta}\right)}, \tag{3.36}$$

where Λ is defined above. As was shown in Ref. Abdullaev et.al. (1999) the safety factor can be presented by the following expansion in a series of powers of the inverse aspect ratio $\varepsilon = \rho/R_p(\rho)$:

$$q(\rho) = q_{cyl}(\rho)\frac{R_0^2}{R_p^2(\rho)}\left(1 + \frac{1}{2}a_2\varepsilon^2 + \frac{3}{8}a_4\varepsilon^4 + O(\varepsilon^8)\right), \tag{3.37}$$

where $q_{cyl}(\rho)$ is described by (3.32). The coefficients a_m are given by

$$a_k = (-1)^m \sum_{k=0}^{m}(m - k + 1)\Lambda^k. \tag{3.38}$$

Similar type of $q-$profile has been obtained in Refs. daSilva et.al. (2001a,b) by solving the Grad-Shafranov equation for the plasma equilibrium. In the lowest order it is shown that for the current density profile (3.34) the $q-$ profile has the form

$$q(\rho_t) = q_{cyl}(\rho_t)\left(1 - 4\frac{\rho_t^2}{R_p^2(0)}\right)^{-1/2}, \tag{3.39}$$

where $q_{cyl}(\rho_t)$ is a the safety factor in a cylindrical approximation (3.32).

The relation between the intrinsic poloidal angle ϑ and the geometrical one θ may be presented in the form of a series of powers of ε,

$$\vartheta(\theta, \rho) = \theta + \sum_{m=1}^{M}\alpha_m \sin m\theta + O(\varepsilon^{M+1}), \tag{3.40}$$

where the expansion coefficients α_m are series in powers of ε:

$$\alpha_m = \sum_{k=0}^{M}\alpha_m^{(k)}\varepsilon^{m+k} + O(\varepsilon^{M+1}).$$

The coefficients α_m for the case $M = 4$ are given by

$$\alpha_1 = a_1\varepsilon + \left(\frac{3a_3}{4} - \frac{a_1 a_2}{2}\right)\varepsilon^3 + O(\varepsilon^5),$$

$$\alpha_2 = \frac{\varepsilon^2}{4}\left[a_2 + \left(a_4 - \frac{a_2^2}{2}\right)\varepsilon^2\right] + O(\varepsilon^5),$$
$$\alpha_3 = \frac{1}{12}a_3\varepsilon^3 + O(\varepsilon^5), \qquad \alpha_4 = \frac{1}{32}a_4\varepsilon^4 + O(\varepsilon^5). \tag{3.41}$$

The coefficients a_m are polynomial functions of the plasma parameter Λ:

$$a_m = (-1)^m \sum_{k=0}^{m}(m-k+1)\Lambda^k.$$

The relation (3.40), expressing the intrinsic poloidal angle ϑ via the geometrical poloidal angle θ, can be inverted to find θ in terms of ϑ,

$$\theta(\vartheta, r) = \vartheta + \sum_{m=1}^{M} \alpha_m^* \sin m\vartheta + O(\varepsilon^{M+1}). \tag{3.42}$$

The expansion coefficients α_m^* can be expressed in terms of coefficients α_m. They are given in Table 3.1.

Table 3.1. The expansion coefficients in Eq. 3.42

$-\alpha_1^*$	$\alpha_1 + \alpha_1\alpha_2 - \frac{1}{4}\alpha_1^3 + O(\epsilon^5)$
$-\alpha_2^*$	$\alpha_2 - \frac{1}{2}\alpha_1^2 - \frac{3}{2}\alpha_1^2\alpha_2 + \frac{1}{4}\alpha_1^4 + \frac{3}{2}\alpha_1\alpha_3 + O(\epsilon^6)$
$-\alpha_3^*$	$\alpha_3 - \frac{3}{2}\alpha_1\alpha_2 + \frac{3}{8}\alpha_1^3 + O(\epsilon^5)$
$-\alpha_4^*$	$\alpha_4 - 2\alpha_1\alpha_3 + 2\alpha_1^2\alpha_2 + \alpha_2^2 - \frac{1}{4}\alpha_1^4. + O(\epsilon^6)$

The accuracy of the relations (3.40) and (3.42) is sufficiently high. At $M = 4$ they deviate from the exact formulas by less than 1%. However, the higher order derivatives, $d^k\vartheta/d\theta^k$ $(k > 2)$, calculated from these formulas are less accurate because of divergence of series.

A dependence θ on ϑ is shown in Fig. 3.4a at the magnetic surface with the safety factor $q(\rho)$=3, and the radial profile of the safety factor $q(\psi)$ is plotted in Fig. 3.4b. The plasma parameters are chosen: $B_\varphi = 1.9$ T, $I_p = 382$ kA, $\beta_{pol} = 0.5$, $l_i = 1.2$ and $R_a = 1.72$ m, $R_0 = 1.75$ m. The radial profile of the plasma current density, $j(\rho)$, is given by Eq. (3.34) with $\nu = q_a/q(0) - 1$, where $q(0) = 0.75$ and q_a determined through the plasma I_p according to Eq. (3.33).

3.5 Spectrum of Hamiltonian perturbations

The perturbation harmonics $H_{m,n}(\psi)$ of the DED magnetic perturbations (2.63), (2.65) are given by Eq. (3.16). Introducing the inverse aspect ratio $\varepsilon =$

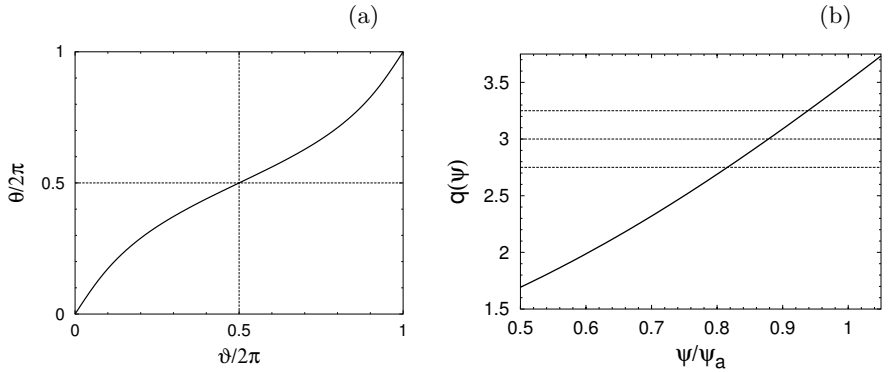

Fig. 3.4. a) Dependence of the intrinsic angle ϑ on the poloidal angle θ ; b) Radial profile of the safety factor $q(\psi)$ vs the normalized toroidal flux ψ/ψ_a, where $\psi_a \equiv \psi(a)$.

$r(\psi)/R_0$ and using the definition of the dimensionless perturbation parameter ϵ, (2.64), one can present R as $R = R_0(1 + \varepsilon(\psi)\cos\theta(\vartheta,\psi))$ and $A_{mn}(r) = \epsilon R_0 B_0 a_{mn}(\psi)$, Eq. (2.63), where a_{mn} are coefficients of order of 1. In the case of the DED perturbation is given by Eq. (2.65). Then using the expansion (2.63) one can transform the coefficients (3.16) into

$$H_{mn}(\psi) = \sum_{m'} S_{m,m'}(\psi) a_{m'n}(\psi), \tag{3.43}$$

where $S_{mm'}(\psi)$ is a transformation matrix defined by

$$S_{m,m'}(\psi) = -\mathrm{Re}\frac{1}{2\pi}\int_0^{2\pi} [1 + \varepsilon\cos\theta(\vartheta,\psi)]\, e^{im'\theta(\vartheta,\psi) - im\vartheta} d\vartheta. \tag{3.44}$$

These Fourier integrals depend on the relation between the poloidal angle θ and the intrinsic poloidal angle ϑ. For the large aspect ratio tokamaks, $\varepsilon \ll 1$, with circular magnetic surfaces $r = \mathrm{const}$, this relation can be approximated by Eq. (3.10): $\theta \approx \vartheta - \varepsilon\sin\vartheta$. Then the diagonal terms $S_{m,m}$ have an order 1, and the non-diagonal terms $S_{m,m\pm k}$, $(k = 1, 2, \cdots)$ have an order of ε^k. Therefore, the main contribution to H_{mn} comes from the harmonics $A_{m,n}$ of the magnetic field with the same poloidal mode m, while the contribution to this poloidal mode m from the sideband modes $A_{m\pm k,n}$ decreases as ε^k.

However, this commonly accepted feature of mode transformation matrix, $S_{m,m'}$, is valid only for small poloidal mode numbers m, m'. As was established by Abdullaev et.al. (1999) for large mode numbers m, m' the matrix $S_{m,m'}$ may grow with m' at the fixed m. It means that the main contributions to H_{mn} may come not from the poloidal mode m and neighboring modes $m' = m \pm 1$ of magnetic field perturbations, but from those modes m' located far from m. Below we study these new features of the mode transformation matrix $S_{mm'}$ using the method of asymptotic estimations of the integral (3.44). Details of calculations are given in Appendix E.

3.5.1 Asymptotics of the transformation matrix elements $S_{m,m'}$

First of all we recall a typical feature of the dependence $\theta = \theta(\vartheta) \equiv \theta(\vartheta, \psi)$. According to a definition we have $\theta(\vartheta = 0) = 0$ (the high field side) and $\theta(\vartheta = \pi) = \pi$ (the low field side) (see, e.g., Fig. 3.4a). These points are the critical points of the function $\theta = \theta(\vartheta)$. At these points the second derivatives $d^2\theta/d\vartheta^2$ vanish. As we will see below that the asymptotics of the integral (3.44) at large m, m' is mainly determined by the behavior of the function $\theta = \theta(\vartheta)$ near these points, namely by the first and third derivatives at the points $\vartheta = 0$ and $\vartheta = \pi$:

$$\gamma_1 = \left.\frac{d\theta}{d\vartheta}\right|_{\theta=0}, \qquad \gamma_3 = \left.\frac{d^3\theta}{d\vartheta^3}\right|_{\theta=0},$$
$$\beta_1 = \left.\frac{d\theta}{d\vartheta}\right|_{\theta=\pi}, \qquad \beta_3 = \left.\frac{d^3\theta}{d\vartheta^3}\right|_{\theta=\pi}. \tag{3.45}$$

One should note that $\gamma_1 > 1$, $\gamma_3 < 0$, $0 < \beta_1 < 1$, and $\beta_3 > 0$. The coefficients γ_1 and β_1 determine the tangents of the curves θ versus ϑ at the low field side and at the high field side, respectively (see Fig. 3.4a).

It is shown in Appendix E that for fixed values of m the main contribution to the integral (3.44) comes from two intervals of m'. For small values of m'

$$m' \le m/\gamma_1 + x_c(m'|\gamma_3|/2)^{1/3}, \qquad (x_c \approx 2)$$

the integral $S_{mm'}(\psi)$ may be expressed as a product

$$S_{mm'}(\psi) = f(0)A_{mm'}(\psi), \qquad f(0) = 1 + \varepsilon, \tag{3.46}$$

where $f(\vartheta) = 1 + \varepsilon\cos\theta(\vartheta)$ and $A_{mm'}(\psi)$ is the the Fourier integral having the following asymptotics at large m', m:

$$A_{mm'}(\psi) = \frac{1}{2\pi}\int_0^{2\pi} e^{i(m'\theta(\vartheta,\psi)-m\vartheta)}d\vartheta$$
$$\approx \left(\frac{2}{|\gamma_3|m'}\right)^{1/3}\mathrm{Ai}\left(-\frac{\gamma_1 m' - m}{(|\gamma_3|m'/2)^{1/3}}\right), \tag{3.47}$$

expressed via the Airy function $\mathrm{Ai}(z)$. The Airy function $\mathrm{Ai}(x)$ oscillates for $x < 0$ and exponentially decays for $x > 0$. It has a local maximum at $x_c \approx -1$.

Similarly, for the values of m',

$$m' > m/\beta_1 - x_c(m'\beta_3/2)^{1/3}, \qquad (x_c \approx 3)$$

the quantity $S_{mm'}(\psi)$ may be approximated by the product

$$S_{mm'}(\psi) = f(\pi)A_{mm'}(\psi), \qquad f(\pi) = 1 - \varepsilon, \tag{3.48}$$

with the following asymptotics

$$A_{mm'}(\psi) \approx (-1)^{m+m'} \left(\frac{2}{\beta_3 m'} \right)^{1/3} \mathrm{Ai}\left(\frac{\beta_1 m' - m}{(\beta_3 m'/2)^{1/3}} \right). \tag{3.49}$$

For the intermediate values of m': $m/\gamma_1 + x_c(m'|\gamma_3|/2)^{1/3} < m' < m/\beta_1 + x_c(m'\beta_3/2)^{1/3}$ unlike (3.47) and (3.49) the integral (3.44) is proportional to $1/\sqrt{m'}$. Contributions from these terms may be neglected due to the rapid oscillations of $A_{mm'}$ with m'.

A typical example of the dependence of the transformation matrix $S_{mm'}$ on m' at the fixed value $m = 12$ is shown in Figure 3.5: a) shows $S_{mm'}$ itself, and b) shows it after multiplication by $(-1)^{m'}$. The solid curves correspond to the exact numerical evaluation the integral (3.44), and the dashed curves describe their asymptotics by the Airy functions. As seen from Figure 3.5b the asymptotic formulas well describe the transformation matrix $S_{mm'}$ near the values $m' \approx m/\gamma_1$ and $m' \approx m/\beta_1$.

From Figures 3.5a, b also follows that the main contribution to $H_{m,n}$ with the fixed m comes from a few magnetic perturbation modes $a_{m',n}$ located near $m' \approx m/\gamma_1$ or $m' \approx m/\beta_1$. The contributions from other modes are negligible because of rapid oscillations of the transformation matrix $S_{m,m'}$.

3.5.2 Asymptotic behavior of $H_{m,n}$

Below we present asymptotical formulae for $H_{m,n}$ in two cases, when the perturbation field is localized on the lower field side (LFS) and on the high field side (HFS).

The LFS perturbation

In this case $a_{m',n}$ changes with m' smoothly. Then one can show that

$$H_{mn}(\psi) \approx \frac{f(0)}{\gamma_1} Ba \left(\frac{m - x_c(|\gamma_3|m/2)^{1/3}}{\gamma_1} \right), \tag{3.50}$$

where $B \approx \sqrt{2\pi/|x_c|}\mathrm{Ai}(x_c)$, and $x_c \approx -1$ is the local maximum of the Airy function, and $a(m) \equiv a_{m,n}$.

The HFS perturbation

In this case $a_{m',n}$ changes rapidly with m' as $a_{m',n} = (-1)^{m'}\tilde{a}(m')$, where $\tilde{a}(m')$ is a smooth function of m'. The asymptotic formula for $H_{m,n}$ is given by

$$H_{mn}(\psi) \approx (-1)^m \frac{f(\pi)}{\beta_1} B\, \tilde{a} \left(\frac{m + x_c(\beta_3 m/2)^{1/3}}{\beta_1} \right). \tag{3.51}$$

Asymptotic formulas (3.50) and (3.51) qualitatively describe the main features of conversations of magnetic perturbations in a toroidal plasmas. They can be

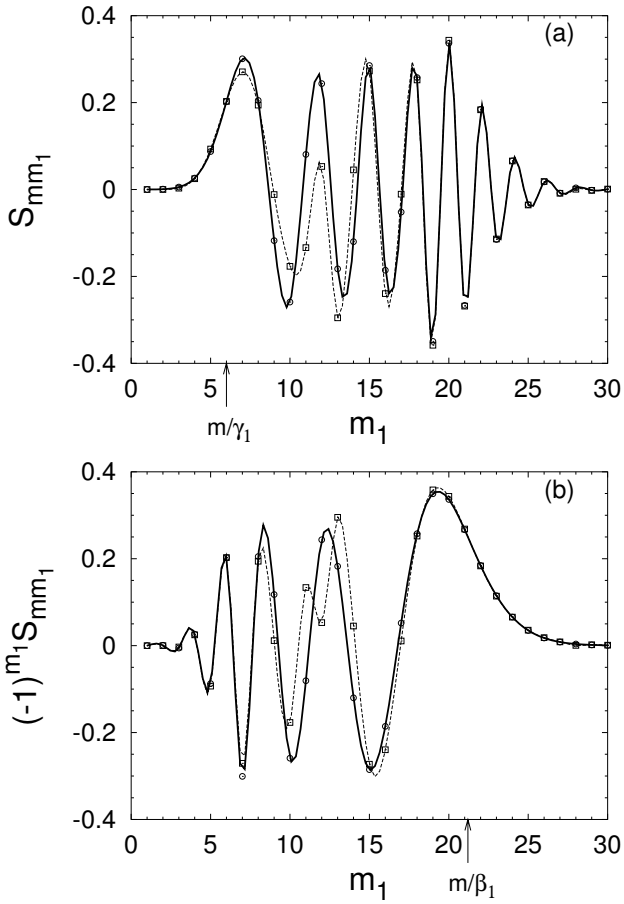

Fig. 3.5. Transformation integral (3.44) S_{mm_1} as a function of m_1 for the fixed $m = 12$: (a) S_{mm_1}; (b) $(-1)^{m_1}S_{mm_1}$. Solid curve describes the exact numerical integration, dashed curve corresponds to the asymptotics given by (3.47), (3.49). The plasma parameter are the same as in Figure 3.4.

also used for quantitative estimations of H_{mn}. To improve their accuracy the two parameters B and x_c in formulas (3.50) and (3.51) can be considered as fitting parameters and chosen to have a better agreement with the numerically calculated values of H_{mn}.

To illustrate the mode transformation consider the following example when the magnetic perturbation modes, a_{mn}, is given by

$$a_{mn}(\psi) = C_m \frac{\sin(m - m_0)\theta_c}{\pi m(m - m_0)}. \tag{3.52}$$

We consider two case type of coefficients C_m: (i) $C_m = (-1)^m$ and (ii)

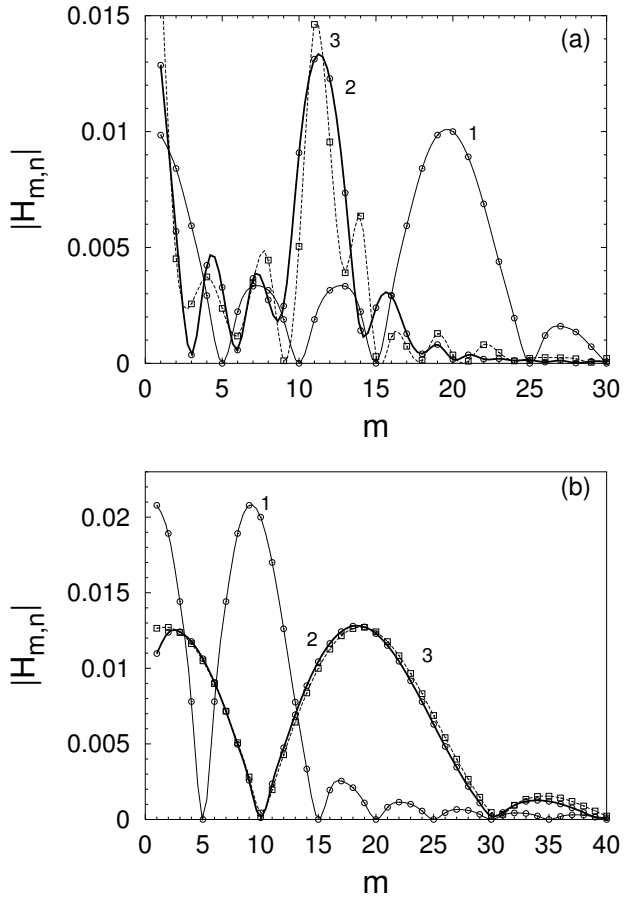

Fig. 3.6. Spectrum of magnetic a_{mn} (curve 1) and Hamiltonian perturbations $H_{m,n}$ obtained from (3.43) by numerical integration (3.44) (solid curve 2) and using the asymptotics (3.51) or (3.50) (dashed curve 3): a) describes the case $C_m = (-1)^m$, $m_0 = 20$, $\theta_c = \pi/5$, fitting parameters: $B = 1.3$, $x_c = -1.$; b) the case (ii) $C_m = 1$, $m_0 = 10$, $\theta_c = \pi/5$. Fitting parameters: $B = 1$, $x_c = 0$.

$C_m = 1$. The modes are localized near the central mode with a width $\Delta m = 2\pi/\theta_c$. Suppose that the equilibrium magnetic field is described by the plasma model considered in Section (3.4.1). The plasma parameters are the same as in Figures 3.4 and 3.5.

As seen from Figure 3.6a in the first case (i) the center of the mode distribution m_0 of magnetic mode perturbations, a_{mn}, (solid curve 1) is shifted to the lower mode $m_0^* \approx m_0\beta_1$ (solid curve 2 and dashed curve 3). The width of the distribution $\Delta m = 2\pi/\theta_c$ of magnetic perturbations became narrow: $\Delta m^* \approx \beta_1 2\pi/\theta_c$. In the second case (ii) the central mode number m_0 of

magnetic perturbations is shifted to higher mode $m_0^* \approx\approx m_0\gamma_1$ and the distribution became wider: $\Delta m^* \approx \gamma_1 2\pi/\theta_c$. The asymptotical formulae (3.50), (3.51) qualitatively correct describe the transformation of magnetic perturbations into Hamiltonian perturbations.

From the asymptotic formulae (3.50), (3.51) it follows that a particular mode m of Hamiltonian perturbations is determined by the mode number $m' \approx m/\gamma_1$ (or $m' \approx m/\beta_1$) of magnetic perturbations. They reflect the specific features of mode conversations between the spectra of Hamiltonian perturbation $H_{m,n}$ and of magnetic perturbations is toroidal plasmas.

3.5.3 DED magnetic perturbation

Since the perturbation field is localized in the finite interval of poloidal angles: $\pi - \theta_c < \theta < \pi + \theta_c$ at the HFS the spectrum $A_{m,n}$ of magnetic perturbation (2.63) contains the factor $g_m \propto (-1)^m$ (see Eq. (2.42)). As have been shown in Section 3.5.2 the spectra of Hamiltonian perturbations $H_{mn}(\psi)$ in this case originate from the spectra of magnetic perturbation $A_{m',n}(\psi)$ with m' located near m/β_1, and for large mode numbers m it is approximately described by

$$H_{mn}(\psi) \approx (-1)^m C \sqrt{1 - \frac{\rho}{R_0}} \left(\frac{\rho - \Delta(\rho)}{r_c}\right)^{m^*} \frac{\sin(m^* - m_c)\theta_c}{\pi\beta_1 m^*(m^* - m_c)}, \quad (3.53)$$

where

$$C = \sqrt{\frac{2\pi}{|x_c|}}\mathrm{Ai}(x_c), \qquad m^* = \frac{m + [m\beta_3/2\beta_1]^{1/3}}{\beta_1}.$$

The radial coordinate ρ is considered as a function of the toroidal flux ψ. For the plasma model with nested circular magnetic surfaces the relation $\rho = \rho(\psi)$ is given by Eq. (3.29). The poloidal spectrum H_{mn} (3.53) is located near the central mode $m_c^* \approx m_c\beta_1$ with the width $\Delta m \approx \pi\beta_1/\Delta\theta_c$. These quantities are mainly determined by the parameter β_1, which depends on the plasma parameter β_{pol} as well as the flux coordinate ψ. The spectra $H_{mn}(\psi)$ can be controlled by simple varying β_{pol}.

3.5.4 Numerical determination of H_{mn}

Although the asymptotic formula for (3.53) qualitatively correct describes the spectrum of Hamiltonian perturbation its accuracy is not enough to obtain the quantitatively correct the critical perturbations for the onset of global chaos of field lines. Since it is hard to obtain the exact analytical formulas for the perturbation spectrum $H_{mn}(\psi)$ we have numerically calculated them using the integral (3.16) and unperturbed field lines $R(\psi,\vartheta), Z(\psi,\vartheta)$ obtained from the numerical integration of the equations of field lines (3.4) over one poloidal turn in the (R, Z) -plane. The safety factor $q(\psi)$, $H_{mn}(\psi)$, and $R(\psi,\vartheta), Z(\psi,\vartheta)$ are found numerically as described in Section 3.3.2.

The safety factor

Figure 3.7 shows profiles of $q(\psi)$ for three different values of the plasma parameter β_{pol}: curve 1 corresponds to $\beta_{pol} = 0.2$, curve 2 − to $\beta_{pol} = 1$, and curve 3 − to $\beta_{pol} = 1.8$. As seen from Figure 3.7 the $q-$ profiles are significantly modified with a variation of β_{pol}. The locations, ψ_{mn}, of the resonant magnetic surface, $q(\psi_{mn}) = m/n$ are shifted toward inward the plasma with increasing the plasma β_{pol}. Particularly, the resonant $q = 3$ magnetic surface is shifted by $\Delta\psi \approx 0.05\psi_a$ when β_{pol} is changed from 1.8 to 1. Since $\psi/\psi_a \approx r^2/a^2$, one can obtain that $\Delta r \approx (a/2)\sqrt{\psi_a/\psi}(\Delta\psi/\psi_a)$.

For the plasma of radius $a = 46$ cm the radial shift of the resonant surface is $\Delta r \approx 1.2$ cm. It shows that the threshold of the formation of stochastic layer changes drastically with the plasma β_{pol}.

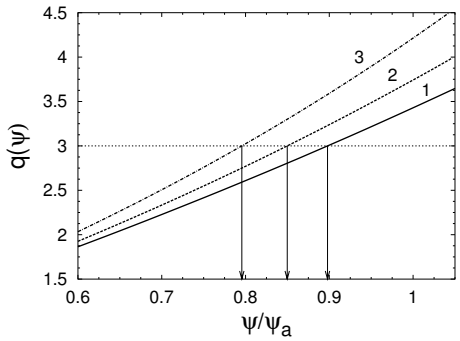

Fig. 3.7. Safety factor profile $q(\psi)$ for three different values of the plasma parameter: curve 1 - $\beta_{pol} = 0.2$, curve 2 − to $\beta_{pol} = 1$, curve 3 − to $\beta_{pol} = 1.8$. The crossing points of these curves with the horizontal line $q = 3$ determine the resonant magnetic flux ψ_{mn}: $q(\psi_{mn}) = 3$.

The perturbation spectra $H_{mn}(\psi)$

Below we shall give a several examples of the numerically found spectrum of $H_{mn}(\psi)$. They show characteristic features of $H_{mn}(\psi)$ at the three operational modes of the DED.

First we consider the characteristic dependence of $H_{mn}(\psi)$ on the plasma β_{pol}, shown in Fig. 3.8 for the 12:4 operational mode at the resonant magnetic surface ψ_{mn}, $m : n = 12 : 4$ for the same values of the plasma β_{pol} as in Fig. 3.7. As seen from Fig. 3.8 that $|H_{m,n}|$ strongly decreased with increasing β_{pol}. This is because of shifting magnetic surfaces towards the LFS with β_{pol} which reduces the influences of perturbation field localized on the HFS.

From Figure 3.8b also follows that only a group of few poloidal modes contributes to the destruction of resonant magnetic surfaces located near the

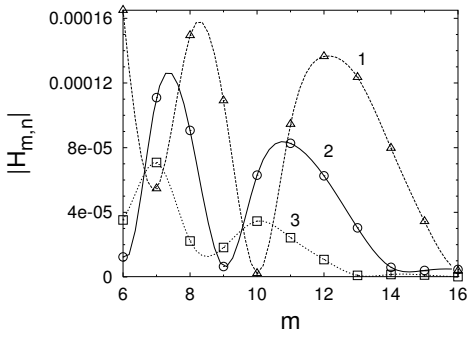

Fig. 3.8. Hamiltonian perturbation spectrum $|H_{m,n}|$ $(n = 4)$ for different values of β_{pol} at the resonant magnetic surface ψ_{mn} $(m : n = 12 : 4)$: curve 1 corresponds to $\beta_{pol} = 0.2$, curve 2 − to $\beta_{pol} = 1$, curve 3 − to $\beta_{pol} = 1.8$.

magnetic surface with $q = 3$. The central mode m_c^* of this group is shifted to small modes m with increasing β_{pol}.

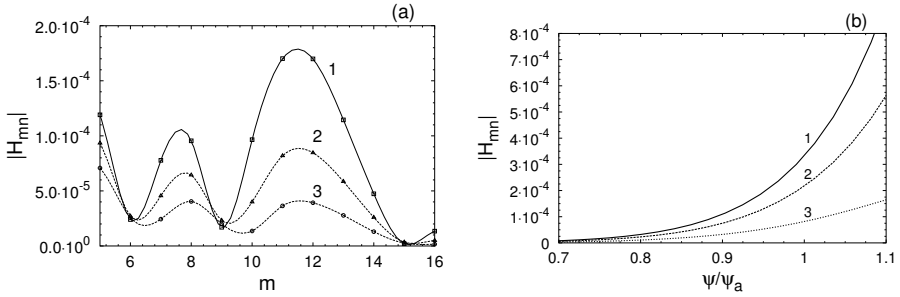

Fig. 3.9. a) Hamiltonian perturbation spectrum $|H_{m,n}|$ $(n = 4)$ at the resonant magnetic surface ψ_{mn}, $q(\psi_{mn}) = m/n$: curve 1 corresponds to $q = 3.25$, curve 2 − to $q = 3$, curve 3 − to $q = 2.75$. b) Dependence of $|H_{m,n}|$ on the toroidal flux ψ/ψ_a: : curve 1 − m=12 , curve 2 − m= 13, curve 3 − m=14. Plasma current I_p= 0.382 MA, toroidal field $B_\varphi = 1.9$ T, the plasma radius $a = 44.7$ cm, $R_0 = 175$ cm, $R_a = 172$ cm, $\beta_{pol} = 0.5$.

The typical spectra of $H_{m,n}(\psi)$ and their radial dependencies at the fixed β_{pol} are shown in Figs. 3.9 - 3.11 for the three operational modes, $m : n =$ 12:4, 6:2, and 3:1, respectively.

First consider the $m : n =$ **12:4 mode**. The plasma parameters (the plasma current I_p= 0.382 MA, toroidal field $B_\varphi = 1.9$ T, the plasma radius $a = 44.7$ cm, $R_0 = 175$ cm, $R_a = 172$ cm, $\beta_{pol} = 0.5$) correspond to the TEXTOR discharge # 93100. Fig. 3.9a shows the spectrum of $H_{mn}(\psi)$ at three resonant magnetic surfaces, ψ_{mn}, $q(\psi_{mn}) = m/n$, corresponding to $q = 4$ (curve 1), $q = 3.5$ (curve 2), and $q = 3$ (curve 3). The dependence of $H_{mn}(\psi)$

on the normalized toroidal flux ψ/ψ_a, where ψ_a is a toroidal flux of the last magnetic surface, is plotted in Fig. 3.9b for the poloidal mode numbers m =12 (curve 1), m =13 (curve 2), and m =14 (curve 3). The dependence of $H_{m,n}$ on ψ following from Eq. (3.53), i.e., $H_{m,n} \propto \psi^{m/2\beta_1}$, is confirmed by the curves in Figure 3.9b. As seen from Fig. 3.9a that only a few poloidal modes $m = 10, \ldots, 14$ are mainly responsible for the formation of the stochastic layer.

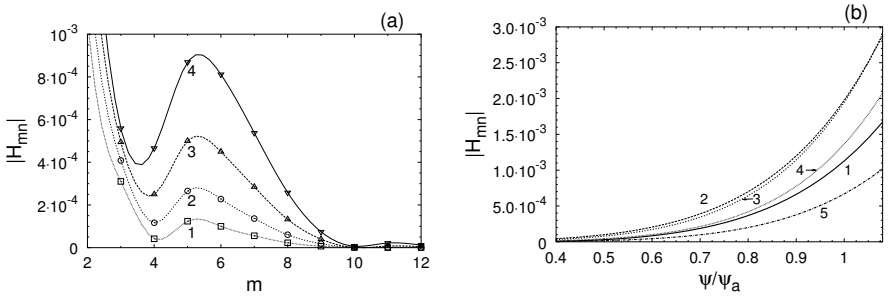

Fig. 3.10. a) Hamiltonian perturbation spectrum $|H_{m,n}|$ ($n = 2$) at the resonant magnetic surface ψ_{mn}, $q(\psi_{mn}) = m/n$: curve 1 corresponds to $q = 4$, curve 2 − to $q = 3.5$, curve 3 − to $q = 3$, curve 4 − to $q = 2.5$. b) Dependence of $|H_{m,n}|$ on the toroidal flux ψ/ψ_a: curve 1 − m=4 , curve 2 − m= 5, curve 3 − m=6, curve 4 − m= 7, curve 5 − m= 8. Plasma current I_p= 0.3 MA, toroidal field B_φ = 2.25 T, the plasma radius a = 46 cm, $R_0 = R_a$ 175 cm, $\beta_{pol} = 0.3$.

The spectrum of $H_{m,n}$ and their radial-profiles for the $m : n$**= 6:2 mode** are plotted in Fig. 3.10 for the plasma parameters: the plasma current I_p= 0.3 MA, the toroidal field B_φ = 2.25 T, the plasma radius a = 46 cm, $R_0 = R_a$ 175 cm, $\beta_{pol} = 0.3$.

The case of the $m : n$**= 3:1 mode** is shown in Fig. 3.11 for the plasma parameters corresponding to the TEXTOR discharge # 94809: the plasma current I_p= 0.3 MA, the toroidal field B_φ = 2.25 T, the plasma radius a = 46 cm, $R_0 = R_a$ 175 cm, $\beta_{pol} = 0.3$.

3.6 Bibliographic notes on mapping methods

The most convenient and natural approach to this problem is to use the Hamiltonian equations of field lines and to study them using symplectic methods of integration, particularly, symplectic mappings. They always preserve a magnetic flux, and run much faster. Several mapping models have been proposed to study the formation of ergodic zone at the plasma edge. The first mapping model has been proposed by Martin and Taylor (1984) for the rectangular model of tokamak. This model has been used in Regianni and Sakanaka (1994)

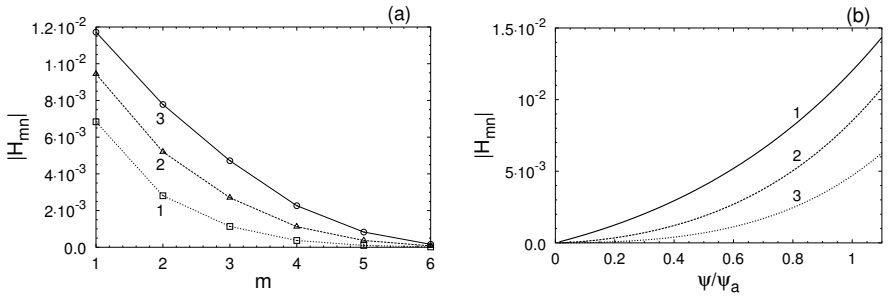

Fig. 3.11. a) Hamiltonian perturbation spectrum $|H_{m,n}|$ ($n = 1$) at the resonant magnetic surface ψ_{mn}, $q(\psi_{mn}) = m/n$: curve 1 corresponds to $q = 4$, curve 2 − to $q = 3$, curve 3 − to $q = 2$. b) Dependence of $|H_{m,n}|$ on the normalized toroidal flux ψ/ψ_a: curve 1 − m=2 , curve 2 − m= 3, curve 3 − m=4, curve 4 − m= 7, curve 5 − m= 8. Plasma current I_p= 0.3 MA, toroidal field $B_\varphi = 2.25$ T, the plasma radius $a = 46$ cm, $R_0 = R_a$ 175 cm, $\beta_{pol} = 0.3$.

to calculate the Lyapunov exponents and diffusion coefficients. The generalization of the Martin and Taylor mapping model to the toroidal plasma and different statistical properties of magnetic field lines have been studied by Viana and Caldas (1992); Caldas et.al. (1996); Viana and Vasconcelos (1997); Ullmann and Caldas (2000); Portela et.al. (2003).

More realistic and generic mapping models for magnetic field lines in the ergodic divertor, namely, the perturbed twist mappings have been proposed by Abdullaev et.al. (1998); Fischer and Cooper (1998); daSilva et.al. (2001a,b, 2002a); da Silva et.al. (2002b). The numerical study and Hamiltonian analyses of magnetic field lines have been also studied in Viana (2000). Rigorous mapping methods developed by Abdullaev et.al. (1999); Abdullaev (1999); Finken et.al. (1999); Abdullaev et.al. (2001); Abdullaev (2002, 2004) were applied to study a magnetic structure of the TEXTOR-DED.

Mapping methods have been also applied to study stochastic field lines in poloidal divertor tokamaks. Particularly, simple algebraic mapping models have been developed in a series of works by Punjabi et.al. (1992, 1994, 1996, 1997, 2003); Ali et.al. (2004) the structure of field lines near the separatrix and on divertor plates. The more rigorous mappings, namely, the separatrix mappings have been constructed by Yamagishi (1995); Abdullaev and Zaslavsky (1995, 1996); Abdullaev and Finken (1998); Abdullaev et.al. (2006).

Beside analytical mapping models numerical mapping methods have been also developed to study field lines and modeling heat and particle transport in tokamak plasmas. The numerical mapping technique has been proposed for integrating Hamiltonian systems, particularly, the equations of magnetic field lines and particles in realistic toroidal geometry. The main idea of the method known as *Interpolated Cell Mapping* has been proposed by Tongue (1987); Montvai and Düchs (1993); de Rover et.al. (1996), and later this numerical mapping and its modifications have been employed by Kasilov et.al.

(1997); Runov et.al. (2001); Feng et.al. (2002) for Monte–Carlo simulations of transport processes in tokamak plasmas with stochastic field lines. The fundamental shortcoming of the numerical mapping is that it is not flux-preserving.

Recently another numerical twist mapping of field lines called TRIP3D_MAP have been constructed by Roeder et.al. (2003); Evans et.al. (2005b) using a magnetic field line integration code, TRIP3D code (Evans et.al. (2002)) in poloidally diverted tokamaks.

4

Properties of the ergodic and laminar zones

4.1 Formation of the ergodic zone

Below we study the formation of the stochastic layer of field lines at the plasma edge in the presence of described above magnetic perturbations. The Hamiltonian equations of field lines (3.13) in this case are integrated using the mappings (3.21). The perturbation modes $H_{m,n}(\psi)$ and the safety factor $q(\psi)$ are found using the cubic spline interpolations of their precomputed values.

4.1.1 Qualitative estimations

The strong influence of the perturbation (3.15) on the field lines originates from terms $\epsilon H_{mn}(\psi)\cos(m\vartheta + n\varphi + \chi_{m0})$, which are resonant on the rational magnetic surfaces ψ_{mn}, $q(\psi_{mn}) = m/n$. These perturbations destroy these magnetic surfaces and create the chain of islands. The width of each magnetic islands is given by (see, Chirikov (1979); Lichtenberg and Lieberman (1992))

$$W_{mn} = 4\left|\frac{\epsilon H_{mn}(\psi_{mn})}{dq^{-1}/d\psi}\right|^{1/2}. \tag{4.1}$$

With increase the perturbation current the width of islands grows as $W_{mn} \propto I_d^{1/2}$. At a certain value of perturbation the neighboring islands overlapping, thus, giving a rise the chaotic motion of field lines. The stochastic layer or the *ergodic zone* at the plasma edge is formed due to the interactions of several magnetic islands ψ_{mn}, $q(\psi_{mn}) = m/n$, $(m_c^* - \Delta m/2 < m < m_c^* + \Delta m/2)$, located near the magnetic surface with $q = 3$.

The qualitative measure of the degree ergodization of field lines can be described by the Chirikov parameter, σ_{Chir},

$$\sigma_{Chir} = \frac{W_{mn} + W_{m+1,n}}{2|\psi_{m+1,n} - \psi_{m,n}|}, \tag{4.2}$$

which characterizes the degree of overlapping of magnetic islands. The Chirikov criteria, (see, Chirikov (1979); Lichtenberg and Lieberman (1992))

$$\sigma_{Chir} \geq 1, \tag{4.3}$$

determines the onset of chaotic motion.

A typical dependence of the Chirikov parameter, σ_{Chir}, (4.2) on the radius $\rho = (\rho_{m,n} + \rho_{m+1,n})/2$, where $\rho_{m,n}$ is a radius of the rational magnetic surface with $q(\rho_{mn}) = m/n$, is shown in Fig. 4.1. The area where $\sigma_{Chir} \geq 1$ approximately determines the ergodic zone of field lines.

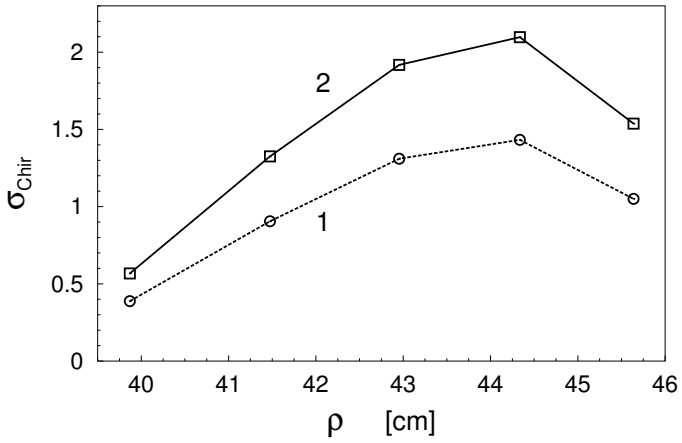

Fig. 4.1. Radial dependence of the Chirikov parameter σ_{Chir} (4.2): curve 1 corresponds to the perturbation current $I_d = 7$ kA; curve 2 – $I_d = 15$ kA. The plasma parameters correspond to TEXTOR shot # 93100: $\beta_{pol} = 0.5$, the plasma current $I_p = 382$ kA, the toroidal field $B_t = 1.9$ T, the major radius of the magnetic axis $R_a = 172$ cm.

The Chirikov criteria gives only a qualitative picture of the formation of the ergodic zone. For the quantitative study of this problem one needs the direct integration of field line equations. Below we study the problem using the mapping (3.21)- (3.23) of Hamiltonian equations of field lines (3.13).

4.1.2 The $m : n = 12 : 4$ operational mode

The typical example of the formation of the stochastic layer in this case is illustrated in Fig. 4.2 by plotting the Poincaré sections of field lines in the (ϑ, ρ) plane and in the toroidal coordinates (θ, r) (see Eq. 3.2) for the different levels of magnetic perturbation. A small rectangular area on the top of the plots in Figs. 4.2 d-f corresponds to the divertor plate. At the sufficiently small magnetic perturbation corresponding to $I_d = 1.5$ kA the resonant magnetic

surfaces $(m : n)$, $(m = 11, \ldots 14)$, are destroyed and the chains of isolated islands are formed as shown in Figs. 4.2 a,d. The increase of the divertor current I_d up to I_d =4.5 kA results in overlapping of three magnetic island with poloidal mode numbers $m = 12, \ldots 14$, and in the formation of the stochastic layer of field lines bounded in a finite area along the radial coordinate ψ. The magnetic field lines in the stochastic layer is practically isolated and only few of chaotic field lines can reach the divertor plates. Figs. 4.2 b,e shows this case. Further increase of the perturbation current creates the well–developed stochastic layer with field lines open to the divertor plates which is shown in Figs. 4.2 c,d for the divertor current $I_d = 7.0$ kA.

In general the formation of the ergodic zone depends on the many parameters of the plasma. It can be varied by changing the profile of the safety factor $q(\psi)$, the plasma parameter β_{pol}, the perturbation current I_d. These aspects of the problem are discussed below (see also Abdullaev et.al. (1999); Finken et.al. (1999); Abdullaev et.al. (2001, 2003)).

4.1.3 Variation of the ergodization level

There are several options to vary the ergodization of field lines at the plasma edge. The first of them is a variation of the divertor current I_d. Due to technical constraints on the maximal value of I_d this option is not sufficient to get sizeable ergodic zone, especially for the higher $\beta_{pol} \geq 1$ (see Finken et.al. (1999)).

The most convenient way to regulate the degree of ergodization and the width of the ergodic zone is a variation of radial positions of main resonant magnetic surfaces ψ_{mn}, $q(\psi_{mn}) = m/n$. Particularly, the ergodization can be increased by shifting the ψ_{mn} towards the HFS which can be implemented by

- increasing the plasma current I_p;
- decreasing the toroidal field B_t;
- lowering the plasma β_{pol};
- shifting the plasma to the HFS as a whole;

In the case shown in Fig. 4.2 the center of the last magnetic surface, R_a, is shifted from the center of torus, R_0, to the HFS on 3 cm.

4.1.4 The $m : n$=6:2 operational mode.

In this operational mode the stochastic layer at the plasma edge is created by overlapping the magnetic islands with the fixed toroidal mode $n = 2$ and the poloidal modes $5 \leq m \leq 9$. As was shown in Fig. 3.10 the corresponding perturbation amplitudes $H_{mn}(\psi)$ penetrate deeper into the plasma than in the case of the 12:4 mode, since $H_{mn}(\psi) \propto \psi^{m/2\beta_1}$. Therefore, the sufficiently large stochastic layer can be created at the smaller perturbation currents. The example of the stochastic layer for this operational mode is shown in Fig. 4.3. The DED-coil configuration is given by Eq. (2.17).

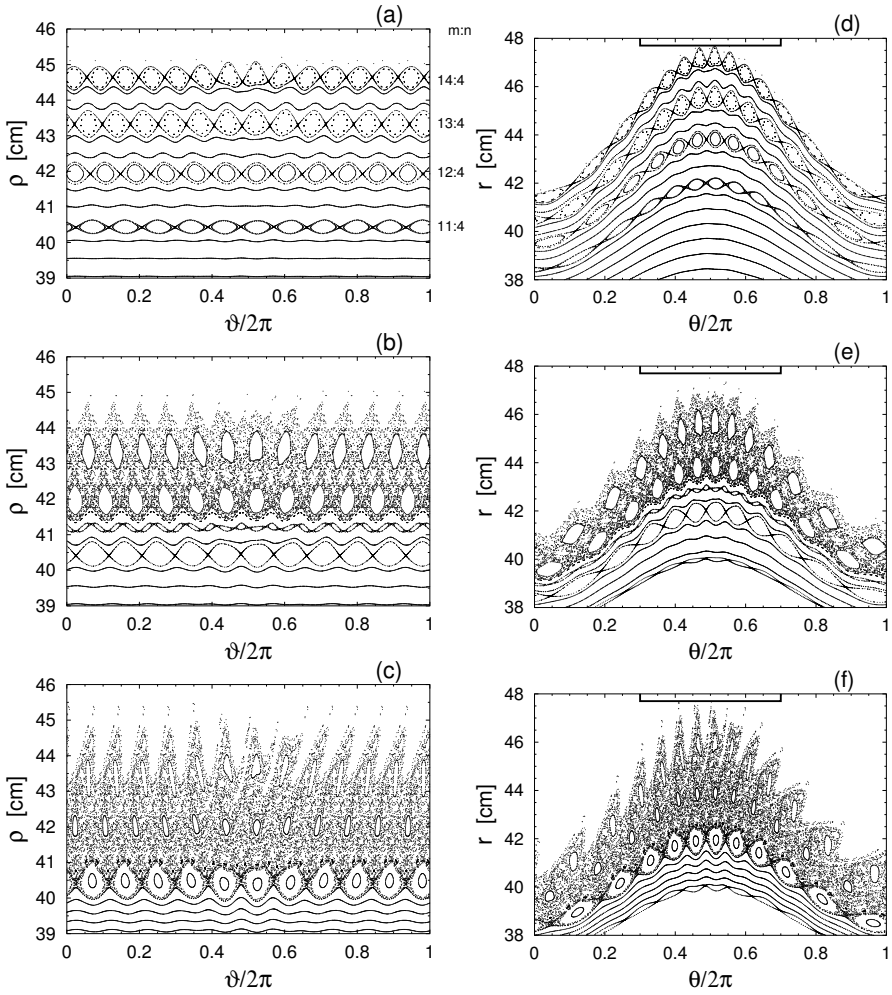

Fig. 4.2. Formation of stochastic layer of field lines with increasing the perturbation current I_d: (a) and (d) the perturbation current $I_d = 1$ kA; (b) and (e) $I_d = 4.5$ kA; (c) and (f) $I_d = 7$ kA. (a)-(c) show the Poincaré sections in the (ϑ, ρ) plane, (d) -(f) – in the geometrical space (θ, r). The plasma parameters correspond to TEXTOR shot # 93100: $\beta_{pol} = 0.5$, the plasma current $I_p = 382$ kA, the toroidal field $B_t = 1.9$ T, the major radius of the magnetic axis $R_a = 172$ cm.

At the lower perturbation current $I_d = 3$ kA the ergodic zone is less developed. It contains the remnants of magnetic islands $m = 6, 7, 8, 9$. The field lines practically does not leave the ergodic zone. With increase the perturbation current the ergodic zone is radially extended. The remnants of islands become smaller, and field lines leave the stochastic layer by hitting the diver-

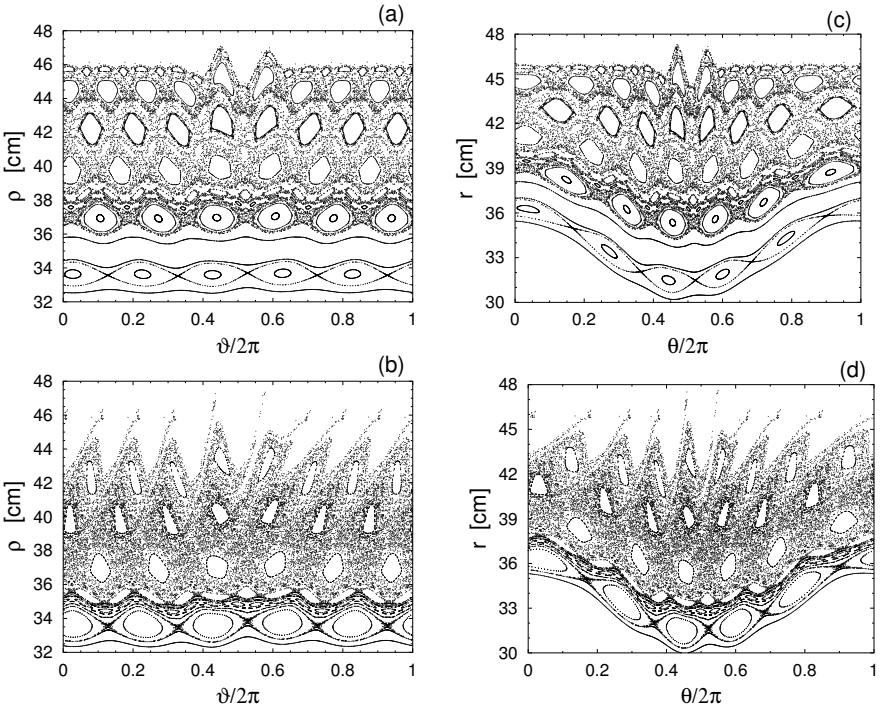

Fig. 4.3. Poincaré sections of field lines in the $m:n$=6:2 operational mode: (a), (c) – the perturbation current $I_d = 3$ kA; (b), (d) – $I_d = 6$ kA; The plasma parameters are $\beta_{pol} = 0.3$, the plasma current $I_p = 300$ kA, the toroidal field $B_t = 2.25$ T, the major radii of the magnetic axis and the torus center are $R_0 = R_a = 175$ cm, the minor radius $a = 46$ cm.

tor plates. Such a case is shown in Fig. 4.3b for the perturbation current $I_d =$ 6 kA.

4.1.5 The $m:n$=3:1 operational mode.

In this regime the perturbation field penetrates deep into the plasma (see Fig. 3.11b). The resonant magnetic perturbation with the toroidal mode $n =$ 1 can trigger a forced reconnection of field lines creating magnetic islands with the poloidal mode numbers $m = 2, 3$ at the resonant magnetic surfaces $q(\psi_{mn}) = m/n$. It will certainly modify the plasma equilibrium. Therefore, the study of ergodization of field lines in this case using the equilibrium plasma configuration and vacuum magnetic perturbation field, in principle, may be not quite correct. The correct treatment of the problem requires also taking into account the plasma response to the external magnetic perturbations. However, this is a complicated problem, and, to our knowledge, at the present time no such an approach to the ergodization of field lines in the plasma has been developed.

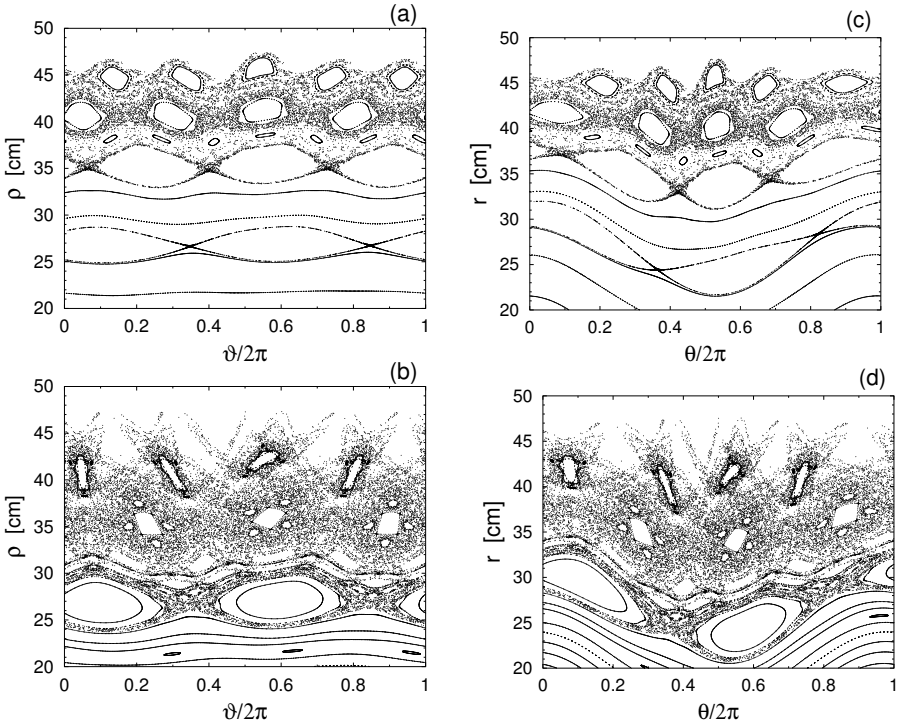

Fig. 4.4. Poincaré sections of field lines in the m : n=3:1 operational mode: (a), (c) − the perturbation current I_d = 1.5 kA; (b), (d) − I_d = 3.75 kA. The plasma parameters corresponds to discharge #94809: B_t = 2.25 T, I_p = 300 kA, β_{pol}=0.3, the major radii of the magnetic axis and the torus center are $R_0 = R_a$ = 175 cm, the minor radius a = 46 cm.

In order to obtain a qualitative picture of ergodization of field lines in the this operational mode we have used the following simplified model. As was observed in the experiments on the TEXTOR-DED when the perturbation current, I_d, exceeds a certain critical level it triggers the $m : n = 2 : 1$ MHD mode and modifies the density and temperature profiles near this island (see Finken et.al. (2004)). The modification of the plasma equilibrium in the case can be taken into account by changing the current density $j(r)$ of the plasma. We have chosen the current density profile $j(r)$ given by Eq. (D.1) which is a constant in the small neighborhood of the resonant surface of the $m : n = 2 : 1$ mode (see Appendix D).

Poincaré sections of the field lines in this case are shown in Fig. 4.4 at the two perturbation currents: (a) I_d = 1.5 kA; (b) I_d = 3.75 kA. The plasma parameters corresponds to the TEXTOR discharge #94809 with the toroidal field B_t = 2.25 T, the plasma current I_p = 300 kA, β_{pol}=0.3, the major radii of the magnetic axis and the torus center are $R_0 = R_a$ = 175 cm, the minor radius a = 46 cm. The coil configuration is given by Eq. 2.9.

As seen from Fig. 4.4 at the lower current, $I_d = 1.5$ kA, the stochastic layer is formed due to overlapping of islands $(m, n) = (3, 1)$ and $(m, n) = (4, 1)$. The $(m = 2, n = 1)$ island is isolated from the stochastic layer. With increasing the perturbation current the island $(m = 2, n = 1)$, as well as, the stochastic layer grow. At certain level of the perturbation current they overlap which leads to the disruptions of the plasma discharge. From the calculation follows that the critical perturbation current I_{crit} for the disruption approximately equal to 3.8 kA. For the standard plasma position, i.e., $R_0 = R_a = 175$ cm, the experimentally found disruption limit of I_{crit} is above 3.75 kA.

4.2 Ergodic divertor as a chaotic scattering system

Field lines at the plasma edge with initial coordinates located in the stochastic layer eventually leave the plasma region hitting the divertor plate (expect for those field lines being trapped inside the magnetic islands). In this sense the ergodic zone with *open field lines can be viewed as a chaotic scattering system* [1], whereby field lines enter into the plasma edge from the divertor plate and leave when hitting it again after a certain number of poloidal turns, N_p, as illustrated in Figure 4.5.

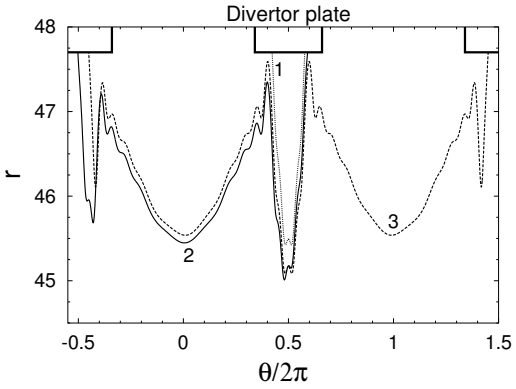

Fig. 4.5. Field lines connecting the divertor plate with itself after a several turns, N_p, along the poloidal angle: curve 1 describes $N_p = 0$, curve 2 corresponds to $N_p = 1$, and curve 3 – to $N_p = 2$.

In chaotic scattering systems, a trajectory may leave a system in one of several different ways. The space of initial coordinates corresponding to the various exit ways are separated by a boundary, which may be a fractal (Bleher et.al. (1990)). The set of initial conditions for which trajectories leave the

[1] A definition of chaotic scattering systems can be found in Eckhard (1988); Bleher et.al. (1989); Tel and Ott (1993) and references therein.

system in a particular way is called a *basin* of a particular mode. In the case of the ergodic divertor it is convenient to classify field lines by the number of poloidal turns N_p. Indeed, the perturbation field created by divertor coils are localized on the HFS, and field lines enter into the plasma and leave it on this side making almost full poloidal turns (see Figure 4.5). Therefore, the set of initial conditions for which field lines cross the section $\theta = 0 \pmod{2\pi}$ with the same number of times may be referred as the basin of a particular number of poloidal turns N_p. Field lines with $N_p = 0$ that do not cross the section $\theta = 0$ belong to a special set called a *private flux zone*. Spatial structures of boundaries of basins belonging to different N_p reveal fine details of the structure of field lines which cannot be seen in Poincaré sections. Below we study the structure of these basins by plotting the contours of N_p within the plasma edge and on the divertor plate.

4.2.1 Basin boundary structure at the plasma edge: Laminar plots

First we consider the structure of basin boundaries referring to the basin as the set of points (ϑ, ψ) at the given poloidal section $\varphi =$ constant which are crossed by field lines with a particular number of poloidal turns N_p. The procedure to obtain these plots is the following.

At the poloidal plane $\varphi = 0$ the field line with a given initial coordinate (ϑ, ψ) is traced by iterating the map (3.21) along the positive and negative directions of the toroidal angle φ until a field line reaches the divertor plate. Then we determine a fractional number of poloidal turns N_{pol} as the ratio of the total change of the poloidal angle $\Delta\theta$ to the full circle 2π, i.e., $N_{pol} = \Delta\theta/2\pi$. The values of N_{pol} computed in this way are close to integer numbers although they are not exactly integer. Let N_p be the integer number closest to N_{pol}. Areas in the (ϑ, ψ)- plane with different poloidal turns N_p are topologically different. The dependence of N_{pol} on the initial coordinates (ϑ, ψ) is displayed by a contour plot with contour lines separating the basins of different poloidal turns N_p. This plot is called as *laminar plot*.

The examples such a plots are presented in Figs. 4.6 for the 12:4 operational mode (Fig. 4.6a) and for the 6:2 mode (Fig. 4.6b). The laminar plot for the 3:1 operational mode is shown in Fig. 4.7a, b in the $(\theta, r)-$ and $(R, Z)-$ planes, respectively. Poincaré sections of field lines corresponding to these laminar plots were given in Figs. 4.2c, 4.3b and 4.4b.

The basin with one poloidal turn has a non-fractal boundary with the private flux zone. But it may have fractal boundaries with the basins corresponding to two and more poloidal turns. For $N_p \geq 2$ there are several topologically different basins related to the same N_p. As seen from Figure 4.6a the relatively large basins of a few poloidal turns $N_p \leq 3$ at the plasma edge are clearly separated by non-fractal boundaries. But they are alternating with the long dark elongated areas (or stripes) containing the basins for a few poloidal turns up to very large N_p. In Eich et.al. (2000) these stripes

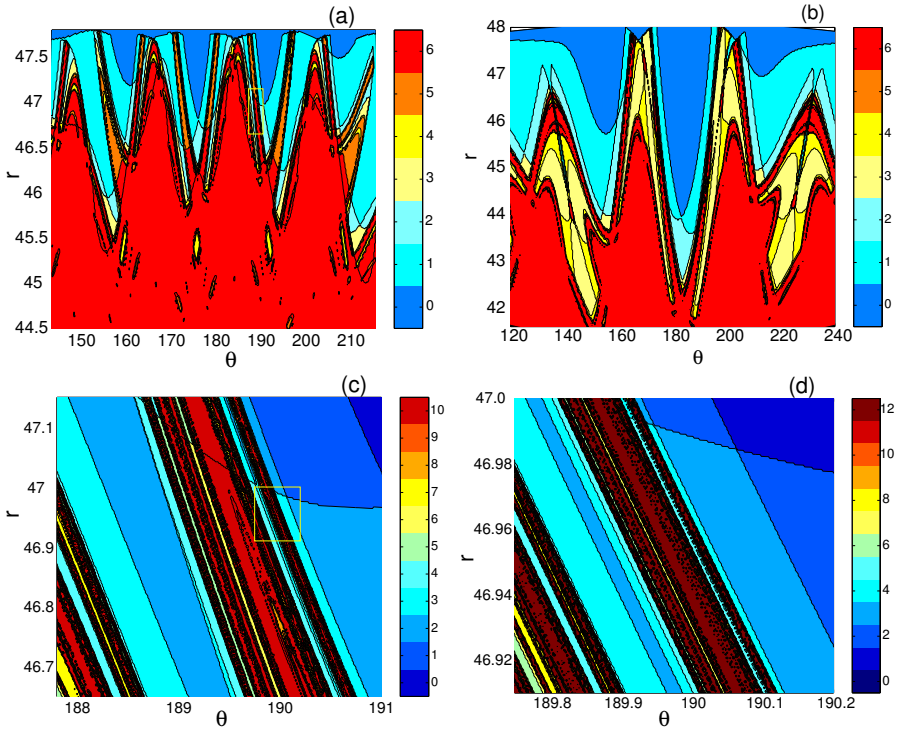

Fig. 4.6. Contour plots of N_p in the (θ, r) – plane on the HFS of torus: a) the 12:4 mode operation for the plasma parameters in Fig. 4.2c; b) the 6:2 mode operation for the plasma parameters in Fig. 4.3b; c) Expanded view of the rectangular area in (a); d) Expanded view of the rectangular area in (c).

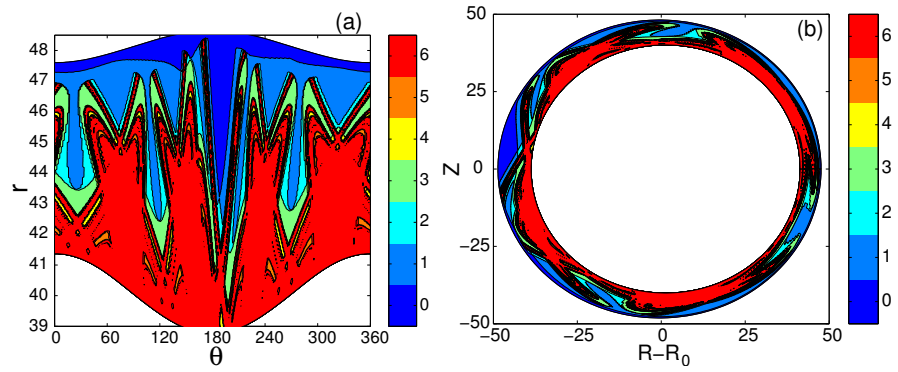

Fig. 4.7. Contour plots of N_p for the 3:1 mode operation: a) in the (θ, r) – plane; b) in the (R, Z) – plane. The plasma parameters corresponds to the discharge #94809 with the same parameters as in Fig. 4.4b.

were called "*fingers*". At the HFS some of these stripes are radially extended toward the divertor plate.

The structure of stripes has a complicated fractal nature. In order to study the fine structure of stripes we have magnified the area of the stripe with the fine resolution of basins of higher poloidal turns. In Figs. 4.6c, d show consecutive blow up of the rectangular areas in Figs. 4.6a and 4.6c, respectively. It shows that the basins at the stripe are highly elongated and the boundaries between them have fractal structure, i.e., the stripes consists of layered basins of different poloidal turns with a self−similar behavior at different spatial scales. As seen from Figure 4.6b the basins of field lines with a few poloidal turns N_p are "sandwiched" between basins for field lines with large numbers of poloidal turns $N_p \gg 1$.

4.2.2 Magnetic footprints

In order to study the basin boundary structure on the divertor plate we will use the following procedure. We follow a field line which enters into the plasma starting from the divertor plate with a given initial coordinate (φ, θ) and returns back to the plate after a certain number of poloidal turns N_p. The set of initial conditions (φ, θ) with a particular number N_p determines a basin. The whole picture of basin boundaries with $N_p \geq 1$ on the plasma wall determines a structure known as *magnetic footprints*. Similar to the stripe at the plasma edge the magnetic footprints have a fractal structure as well.

The examples of magnetic footprints are displayed in Figs. 4.8: a) for the 12:4 operational mode; b) for the 6:2 operational mode; b) for the 3:1 operational mode. The corresponding Poincaré sections and laminar plots were given in Figs. 4.2c, 4.3b and 4.4b, and Figs. 4.6 and 4.7, respectively.

One can see from Figs. 4.8a,b that for the 12:4 operational mode the the field lines can enter into the plasma (or hit the divertor plate from the plasma side) only along the four pairs of narrow helical stripes, for the 6:2 operational mode − along two pair helical stripe, and for the 3:1 operational mode − along one pair helical stripe. (Dark blue areas in Figures correspond to the field lines in a private flux zone). The distance between stripes of each pairs depends on the plasma current I_p (see Ref. Abdullaev et.al. (2001)). Each helical stripe has a fractal structure and it consists of layered basins of different poloidal turns (see Fig. 4.8a, b). The width of layers is changing along the toroidal direction φ. The area of the basin with one poloidal turn $N_p = 1$ is the largest. For the higher $N_p > 1$ corresponding areas of basins are drastically decreased in size. The boundaries between these basins are fractal.

The fine structure of helical stripes can be revealed by studying the dependence of N_p on the poloidal angle θ for fixed toroidal angle φ. Such a dependence of N_p on θ is described by Cantor-like, fractal curves. It is presented in Fig. 4.9 for the 12:4 mode at the fixed toroidal angle $\varphi = 180°$. The curve in Fig. 4.9a describes the poloidal section of the all four helical stripes shown in Figure 4.8a, while the expanded view of the area along the

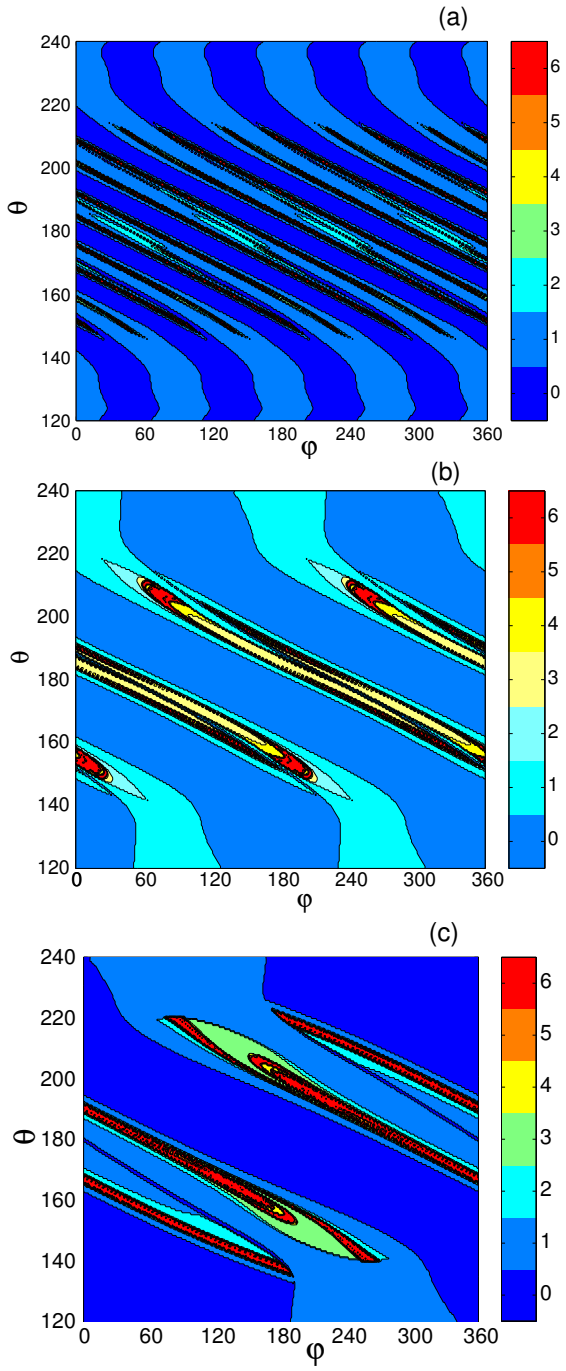

Fig. 4.8. Basin boundary structure (magnetic footprints) on the (φ, θ) - plane at the divertor plane: a) for the 12:4 mode; the plasma parameters are the same as in Fig. 4.2; b) for the 6:2 mode for the same plasma as in Fig. 4.3. (c) for the 3:1 mode during the discharge #94809 with the same parameters as in Fig. 4.4b.

one helical stripe is shown in Fig. 4.9b. They clearly show areas of field lines connecting plate to plate in one, two, three and more poloidal turns N_{pol}. These areas are described by almost horizontal steps in the fractal curve. The width of layers becomes smaller with increasing N_{pol}.

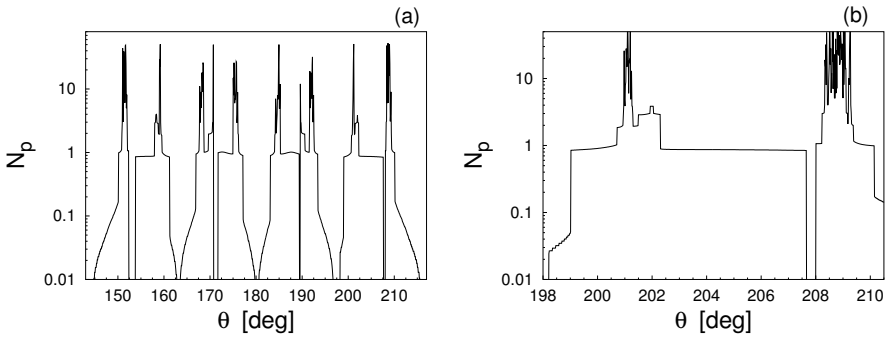

Fig. 4.9. (a) Fractal dependence of N_{pol} on θ at fixed toroidal angle $\varphi = 180°$ corresponding the magnetic footprint in Fig. 4.8a; (b) a view of the one helical stripe. The operational mode is 12:4.

The structure of the helical stripes plays an important role for heat and particle deposition on the divertor plates. Indeed, the basins with $N_p \gg 1$ correspond to the field lines coming from deep within ergodic zone. These field lines may bring high energetic particles to the wall because the particles predominantly move along field lines. Therefore one can expect that the spatial distribution of power deposition within the helical stripes will depend on the spatial structure of basins with $N_p > 1$. The cross–field diffusion of particles broadens the spatial distribution of power deposition around the maxima located at the basins corresponding to large number of poloidal turns. This conclusion is confirmed with the Monte–Carlo simulations of heat and energy transport in the ergodic zone (Runov et.al. (2001)).

4.3 Diffusion of field lines

The chaotic field lines in the ergodic layer contribute to the radial energy and particle transport at the plasma edge in addition to the perpendicular energy transport caused by turbulent processes in the plasma. To illustrate this consider for simplicity a collisionless plasma. Since electrons predominantly follow magnetic field lines the radial transport of electrons is determined by the radial deviation of field lines from the magnetic surfaces. Indeed, the radial diffusion coefficient of electrons is defined as $D_e = \langle(\Delta r)^2\rangle/2\Delta t$ where Δr is a random radial advance of particle during time period Δt, and $\langle(\cdots)^2\rangle$

stands for averaging over magnetic surface. Suppose that v_e is the thermal velocity of electrons. They make a full toroidal turn in time $\Delta t = \Delta l/v_e$ where $\Delta l = 2\pi R_0$ is the length of field line. Therefore

$$D_e = \frac{\langle(\Delta r)^2\rangle}{2\Delta t} = \frac{\Delta l}{\Delta t}\frac{\langle(\Delta r)^2\rangle}{2\Delta l} = D_{FL}v_e, \tag{4.4}$$

where

$$D_{FL} = \frac{\langle(\Delta r)^2\rangle}{2\Delta l}, \tag{4.5}$$

defines the diffusion coefficient of field lines. It means that in the collisionless plasma the diffusion of charged particles is mainly determined by the radial diffusion of field lines [2]. Below we discuss the problem of determination of field line diffusion coefficients.

4.3.1 Global and local diffusion coefficients

Let $\sigma(l)$ is the second order displacement moment,

$$\sigma^2(l) = \langle(\rho - \langle\rho(l)\rangle)^2\rangle = \frac{1}{N}\sum_{i=1}^{N}(\rho_i(l) - \langle\rho\rangle)^2, \tag{4.6}$$

where $\langle(\dots)\rangle$ means over a set of initial conditions at $l = 0$ taken on a certain magnetic surface.

First consider the definition of diffusion coefficients in an unlimited domain stochastic layer. In this case the asymptotics of $\sigma(l)$ at the large distance l has the following general behavior,

$$\sigma^2(l) = 2D_{FL}l^{\gamma}, \qquad l \to \infty, \tag{4.7}$$

where D_{FL} is a constant coefficient. For a normal Gaussian process the exponent $\gamma = 1$, and the coefficient D_{FL} is defined as a field line diffusion coefficient, $D_{FL} = \sigma(l)/2l$, $l \to \infty$. Such a diffusion coefficient can be called as *global* since it characterizes a global diffusive behavior of a system.

However, in the stochastic system with a finite domain, as the ergodic zone of field lines, the asymptotics (4.7) is not valid at long distances l, since in this case $\sigma(l) \to$ constant at $l \to \infty$, i.e., one cannot introduce the global diffusion coefficient D_{FL} defined as a ratio $D_{FL} = \sigma(l)/2l$, $l \to \infty$.

In this case one can also introduce the running diffusion coefficient of field lines defined as

$$D(l) = \frac{\sigma^2(l)}{2l}. \tag{4.8}$$

[2] Actually the radial transport of charged particles in the plasma is more complicated. It is determined not only due to collisions of particles but also the different kind of electromagnetic instabilities developing in the plasma (see Wesson (2004))

In an unlimited domain $D(l)$ tends to a finite value in the limit $l \to \infty$. However, in the ergodic zone the running diffusion coefficient $D(l)$ goes to zero when $l \to \infty$. At finite value of l it characterizes the radial diffusion rate of field lines.

In order to describe a transport in the stochastic layer one can also introduce a *local diffusion coefficient* $D_{FL}(r)$. It gives a quantitative measure of field line diffusion near the given magnetic surface of radius ρ. Below we give analytical and numerical determinations of diffusion coefficients.

4.3.2 Quasilinear diffusion coefficients

For the highly developed ergodic zone the diffusion coefficient D_{FL} can be obtained from the Hamiltonian equations of field lines with the Hamiltonian (1.4), (1.5). According to the quasilinear approximation (see, e.g., Lichtenberg and Lieberman (1992)) the diffusion coefficient D in the toroidal magnetic flux ψ for the Hamiltonian system (1.4), (1.5) given by

$$D_M = \pi\epsilon^2 \sum_{m,n} m^2 \left|H_{mn}(\psi)\right|^2 \delta\left(\frac{m}{q(\psi)} - n\right).$$

The relation between the diffusion coefficient D_{FL} and D_M in the magnetic flux, ψ, and the radial r coordinates can be found using the relation $\psi = r^2/2R^2$:

$$D_{FL}^{(Q)} = \frac{R_0^3}{r^2} D_M = \pi\epsilon^2 \frac{R_0^3}{r^2} \sum_{m,n} m^2 \left|H_{mn}(\psi)\right|^2 \delta\left(\frac{m}{q(\psi)} - n\right). \tag{4.9}$$

It coincides with the traditionally used quasilinear formula for D_{FL} (see Ghendrih et.al. (1996)) if the term $\epsilon m H_{mn}$ is replaced by rB_{mn}/R_0B_0 where B_{mn} is the Fourier expansion coefficient of the perturbed field B_r, i.e.,

$$D_{FL}^{(Q)} = \pi R_0 \sum_{m,n} \left(\frac{B_{mn}(r)}{B_0}\right)^2 \delta\left(\frac{m}{q(\psi)} - n\right). \tag{4.10}$$

4.3.3 Numerical calculation of field line diffusion coefficients

To determine a local diffusion coefficient, $D_{FL}(r)$, numerically we calculate the second order radial displacement moments according to Eq. (4.6) performing the averaging over a set of initial field lines with initial angle θ being uniformly distributed on the magnetic surface $r = r_0(\theta)$.

As was mentioned above in the ergodic zone one cannot introduce a global diffusion coefficient $D = \sigma_r(l)/2l$, $(l \to \infty)$ as in the case of unlimited stochastic domain. However, one can introduce a local diffusion coefficient $D_{FL}(r)$ as $\sigma_r(l)/2l$ which is valid for the initial linear growth regime of $\sigma_r(l)$ with l Abdullaev et.al. (1999).

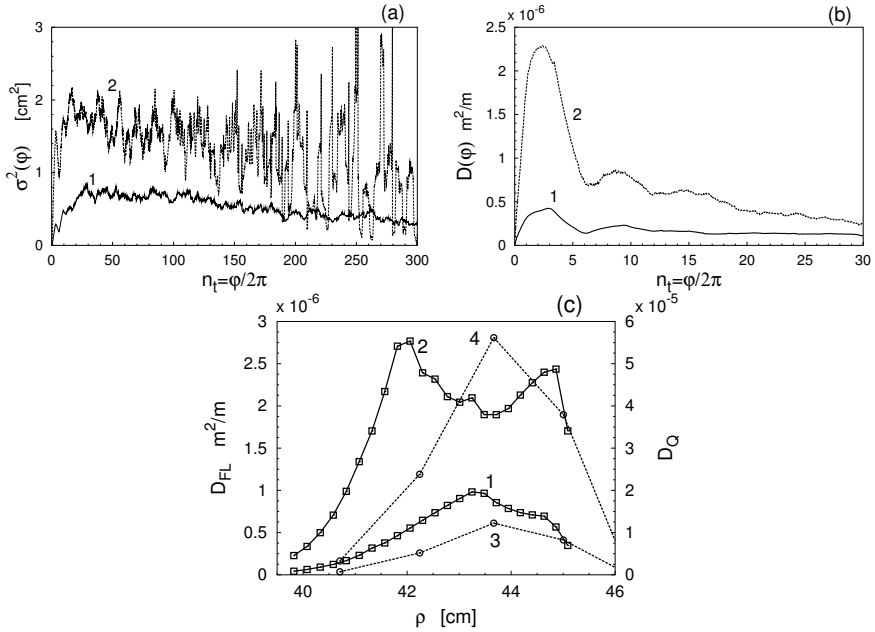

Fig. 4.10. a) Mean square radial displacement $\sigma^2(l)$ vs the toroidal angle φ for the different perturbation currents: curve 1 describes the case $I_d = 7$ kA; curve 2 corresponds to $I_d = 15$ kA. b) Running diffusion coefficient $D(\varphi)$: curve $1 - I_d = 7$ kA; curve $2 - I_d = 15$ kA. c) Radial profiles of local field line diffusion coefficient D_{FL} and the quasilinear diffusion coefficient D_Q (4.9) for the 12:4 mode at two different perturbation currents: curves 1 and 3 corresponds to $I_d = 7$ kA, curves 2 and 4 corresponds to $I_d = 15$ kA. The equilibrium plasma parameters are the same as in Fig. 4.2.

The 12:4 operational mode

Dependence $\sigma^2_\rho(l)$ along the toroidal angle $\varphi = l/2\pi R_0$ is plotted in Fig. 4.10a for the two different perturbation currents: curve 1 describes the case $I_d = 7$ kA; curve $2 - I_d$ =15 kA. The plasma parameters are the same as in Figs. 4.2. The averaging in Eq. (4.6) is performed over initial field lines on the magnetic surface of radius $\rho = 40.84$ cm. In the first case field lines are mostly confined in the ergodic zone and they don't reach the divertor plate, while in the second case the field lines are open and they reach the divertor plate after a certain number of poloidal turns. It has the following features: $\sigma_{r_0}(l)$ grows with l up to a certain distance, when field lines reach the boundaries of the ergodic zone, and then it tends to a constant value as shown by curve 1 in Fig. 4.10a or it decreases when field lines leave the ergodic zone hitting the divertor plates (curve 2 Fig. 4.10a). The corresponding running diffusion coefficients $D(l)$ defined by Eq. (4.8) are plotted in Fig. 4.10b.

The profiles of the local diffusion coefficient $D_{FL}(r)$ as a function of magnetic surface radius ρ are shown in Figure 4.10c for the perturbation currents: curve 1 – $I_d = 7$ kA, curve 2 – $I_d = 15$ kA. The corresponding quasilinear diffusion coefficients D_Q (4.9) are also plotted in this figure: curve 3 – $I_d = 7$ kA, curve 4 – $I_d = 15$ kA. One can see that D_{FL} grows with ρ monotonically up to the certain radius ρ_c then it decays in the zone $\rho > \rho_c$ where the field lines hit the divertor plates in very short lengths. The radius ρ_c characterizes the inner boundary of the zone of almost regular (non-chaotic) field lines with very short wall to wall connection lengths, i.e. the *laminar zone* The width of the laminar zone grows with the perturbation current I_d.

Usually the quasilinear diffusion coefficients overestimates the diffusion transport rate in the DED ergodic zone. The quasilinear theory is not valid in this case since the ergodic zone is formed by overlapping only a few neighboring magnetic islands.

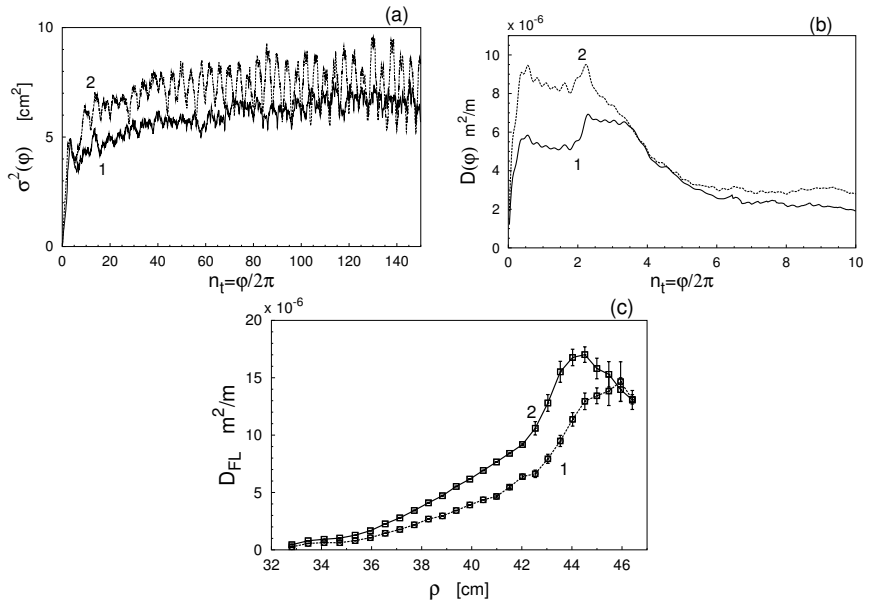

Fig. 4.11. The same as in Fig. 4.10, but for the 6:2 operational mode for the different perturbation currents:: curve 1 - $I_d = 6$ kA, curve 2 - $I_d = 7.5$ kA; In (a) and (b) ρ =41.5 cm. The equilibrium plasma parameters are the same as in Fig. 4.3.

The 6:2 operational mode

The mean square displacement moment σ^2, the running diffusion coefficients D and the local diffusion coefficients D_{FL} for this case are shown in Fig. 4.11 a-c, respectively, for the plasma parameters taken above in Figs. 4.3. As seen

from Fig. 4.11 in this operational mode the diffusion coefficients of field lines is one order larger than in the case of operational mode 12:4 at the same perturbation current I_d. This is mainly due to large radial excursions of field lines in the presence of resonant magnetic perturbations $m : n = m : 2$, with the poloidal modes $m = 5, 6, 7, 8$.

The 3:1 operational mode

The mean square displacement moment σ^2, the running diffusion coefficients D and the local diffusion coefficients D_{FL} are presented in Fig. 4.12 a-c, respectively, for the plasma discharge #94809. The corresponding Poincaré section, the laminar plot of field lines were given in Fig. 4.4 and Fig. 4.7. As expected, the diffusion coefficients, D_{FL}, in this case are larger than in the cases of 12:4 and 6:2 operational modes. Particularly, at the same perturbation current the typical values of D_{FL} of the 3:1 mode exceeds the corresponding ones in the 6:2 mode by factor 10.

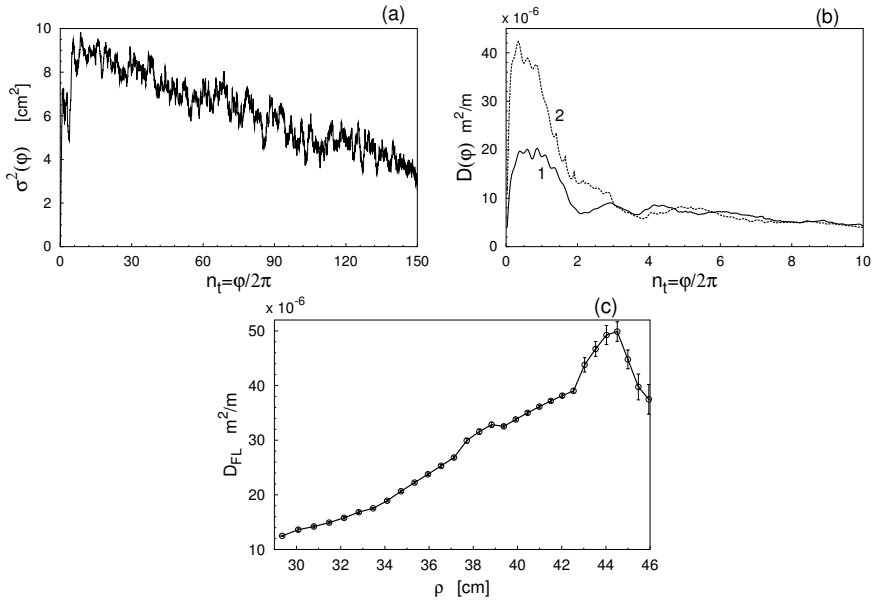

Fig. 4.12. The same as in Fig. 4.10, but for the 3:1 operational mode. The perturbation current $I_d = 3.75$ kA. In (a) $\rho = 42$ cm, and (b) curve 1 corresponds to $\rho = 34.1$ cm, curve 2 – ρ =42 cm. The equilibrium plasma parameters are the same as in Fig. 4.4.

One should note that the local and quasilinear diffusion coefficients do not completely describe the transport processes in the ergodic zone. They are valid only for the highly developed ergodic zone. The typical ergodic zone

at the plasma edge is not well-developed, and it consists of areas with the remnants of magnetic islands as well as areas with almost regular field lines with short connection lengths (the laminar zone). The transport processes in such an ergodic zone cannot be simply described by the quasilinear theory.

4.4 Lyapunov exponents and Kolmogorov lengths

One of important characteristics of chaotic systems is the *Lyapunov exponent*. It gives the quantitative measure of exponential divergence of nearby orbits (or field lines in the ergodic zone). The Lyapunov exponent is related with another statistical characteristic of chaotic dynamical system, namely, with the *Kolmogorov time* (or the *Kolmogorov length* of chaotic field lines) which characterizes the loss of information on initial state of system in time.

In this section we estimate the Lyapunov exponent and the Kolmogorov length of field lines in the ergodic zone. Since field lines in the ergodic zone are open and have finite connection lengths we will introduce finite–time Lyapunov exponent (or local Lyapunov exponent) and the local Kolmogorov length.

4.4.1 Definition of Lyapunov exponent

Below we give a definition of the Lyapunov exponent and the method of its calculation for symplectic mappings (3.19). Let

$$d\mathbf{I}_k = \begin{pmatrix} d\psi_k \\ d\vartheta_k \end{pmatrix} \tag{4.11}$$

be an infinitesimal vector separating neighboring orbits at the k-th step. The evolution of the vector $d\mathbf{I}_k$ for one map iteration is described by the following equation

$$d\mathbf{I}_{k+1} = \mathbf{J}_k d\mathbf{I}_k, \tag{4.12}$$

where $\mathbf{J}_k$ is the Jacobian matrix of the mapping (3.19):

$$\mathbf{J}_k = \begin{pmatrix} \frac{\partial \psi_{k+1}}{\partial \psi_k} & \frac{\partial \psi_{k+1}}{\partial \vartheta_k} \\ \\ \frac{\partial \vartheta_{k+1}}{\partial \psi_k} & \frac{\partial \vartheta_{k+1}}{\partial \vartheta_k} \end{pmatrix}. \tag{4.13}$$

We recall the property $\det \mathbf{J}_k = 1$. The calculation of the Jacobi matrix of the mapping (3.21)– (3.23) is given in Appendix F.

Consider the evolution of the distance $ds_k = \sqrt{d\psi_k^2 + d\vartheta_k^2}$ between orbits in the (ϑ, ψ) plane. According to (4.12) its square, ds_k^2, can be written as

$$ds_k^2 = d\mathbf{I}_k^T d\mathbf{I}_k = d\mathbf{I}_{k-1}^T \mathbf{J}_k^T \mathbf{J}_k d\mathbf{I}_{k-1}$$

$$= d\mathbf{I}_0^T \mathbf{J}_1^T \cdots \mathbf{J}_k^T \mathbf{J}_k \cdots \mathbf{J}_1 d\mathbf{I}_0. \tag{4.14}$$

Let $\lambda_1^{(k)}, \lambda_2^{(k)}$ be the eigenvalues of the matrix $\mathbf{J}_k$ which satisfy the eigenvalue problem,

$$\mathbf{J}_k \mathbf{A} = \lambda \mathbf{A},$$

where $\mathbf{A}$ is the corresponding eigenvector. The eigenvalues are found as solutions of the equation

$$\det \begin{pmatrix} \frac{\partial \psi_{k+1}}{\partial \psi_k} - \lambda & \frac{\partial \psi_{k+1}}{\partial \vartheta_k} \\ \frac{\partial \vartheta_{k+1}}{\partial \psi_k} & \frac{\partial \vartheta_{k+1}}{\partial \vartheta_k} - \lambda \end{pmatrix} = 0,$$

from which it follows that

$$\lambda_{1,2}^{(k)} = D \pm \sqrt{D-1}, \tag{4.15}$$

where

$$D = \frac{1}{2} \left(\frac{\partial \psi_{k+1}}{\partial \psi_k} + \frac{\partial \vartheta_{k+1}}{\partial \vartheta_k} \right).$$

In Eq. (4.15) we have taken into account that according to the volume–preserving condition (3.20) the determinant of the Jacobi matrix $\mathbf{J}_k$ is unity.

In general, the eigenvalues $\lambda_1^{(k)}, \lambda_2^{(k)}$ are functions of local coordinates (ϑ_k, ψ_k). In the case $D > 1$ the eigenvalues $\lambda_{1k}, \lambda_{2k}$ are real, and satisfy the condition

$$\lambda_1^{(k)} > 1, \qquad \lambda_2^{(k)} < 1, \qquad \lambda_1^{(k)} \lambda_2^{(k)} = 1.$$

In this case the orbits is locally unstable. If $D < 1$ the eigenvalues λ_{1k} and λ_{2k} are complex numbers, with the unity modules, $|\lambda_{1k}| = |\lambda_{2k}| = 1$. The orbits in this case are locally stable.

The *global Lyapunov exponent*, σ, is defined as

$$\sigma = \lim_{N \to \infty} \frac{1}{N} \ln \frac{ds_N}{ds_0}, \tag{4.16}$$

or $ds_n = \exp(N\sigma) ds_0$, i.e., it characterizes the degree exponential divergency of orbit per one map iteration. According to (4.14), it is determined by the largest eigenvalue, $\lambda^{(k)} = \max(\lambda_1^{(k)}, \lambda_2^{(k)})$, of the Jacobian matrix $\mathbf{J}_k$:

$$\sigma = \lim_{N \to \infty} \frac{1}{N} \ln \prod_{k=1}^{N} \lambda^{(k)}. \tag{4.17}$$

When the eigenvalue $\lambda^{(k)}$ does not depend on the local coordinates (ϑ_k, ψ_k), i.e., $\lambda^{(k)} = \lambda_1$, then $\sigma = \ln \lambda_1$. The Lyapunov exponent, σ, is positive for the unstable orbits, and it vanishes, $\sigma = 0$, for the stable orbit. For a chaotic system in a finite domain the Lyapunov exponent has a fixed value independent on initial positions of the system.

4.4.2 Finite–time Lyapunov exponent

In the ergodic zone the field lines have a finite connection lengths. Therefore, we cannot determine the global Lyapunov exponent, σ, defined by Eq. (4.17). In this case one can use the so-called *finite–time Lyapunov exponent*, σ_N. It is defined for a finite steps, N, of the map, (see, e.g., Ott (1993)), i.e.,

$$\sigma_N = \frac{1}{N} \ln \frac{ds_N}{ds_0} = \frac{1}{N} \ln \prod_{k=1}^{N} \lambda^{(k)}. \tag{4.18}$$

It characterizes the local divergency of orbits in a chaotic system and depends on the initial coordinates (ϑ_0, ψ_0). We call it as a *local Lyapunov exponent*. The quantity,

$$L_N = \frac{l}{\sigma_N}, \tag{4.19}$$

where l is the length of field line per one map step, gives a quantitative measure of the local e-folding length of exponential separation of neighboring orbits.

The quantity L_N similar to σ_N sensitively depends on the initial condition. Particularly, its dependence on the initial poloidal angle ϑ has a fractal nature. A typical dependence of L_N on ϑ is plotted in Fig. 4.13 for the 12:4 operational mode. Initial field lines are taken on the magnetic surface of radius $\rho = 42.8$ cm, and they are run until crossing the divertor plate, i.e., the number N in Eq. (4.19) is taken equal to the possible maximal number of map iteration. As seen from Fig. 4.13a, b the dependence L_N on the initial poloidal angle has indeed a fractal nature.

4.4.3 The Kolmogorov length

As we have seen the length L_N for open chaotic field lines depends on initial conditions. Below we introduce the characteristic e-folding length of exponential divergence of neighboring field lines of given magnetic surface of radius ρ (or toroidal flux ψ) by averaging over initial poloidal angles, i.e., we define the length, $L_K(\rho, N)$, as the inverse of the finite-time Lyapunov exponent, $\bar{\sigma}(\rho)$, averaged over the magnetic surface of radius ρ (or toroidal flux ψ):

$$L_K(\rho, N) = \frac{l}{\bar{\sigma}_N}, \tag{4.20}$$

$$\bar{\sigma}_N = \frac{1}{M} \sum_{i=1}^{M} \sigma_N(i),$$

where $\sigma_N(i)$ is the local Lyapunov exponent (4.18) with the initial coordinate $(\vartheta_i = 2\pi i/M, \psi(\rho))$, and M is a number of field lines. Following to Ghendrih et.al. (1992, 1996) we call the quantity $L_K(\rho, N)$, as the *Kolmogorov length*

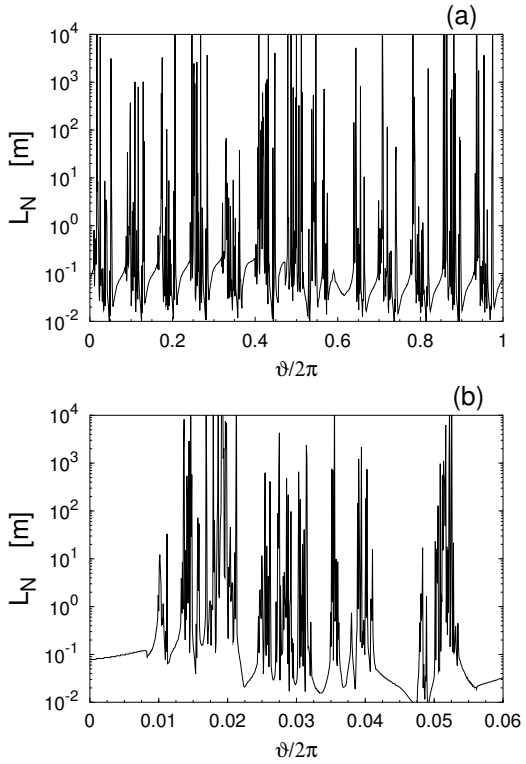

Fig. 4.13. Local e-folding length L_N vs the initial poloidal angle ϑ. Initial field lines taken on the magnetic surface of radius $\rho = 42.8$ cm are run until they reach the divertor plate. The perturbation current $I_d = 15$ kA. a) shows the whole interval of ϑ. b) shows the expanded view in the interval $0 \leq \vartheta/2\pi \leq 0.06$. The equilibrium plasma parameters are the same as in Fig. 4.2.

which is a *statistical measure* of the e-folding length of exponential divergence of neighboring field lines. According to the definition (4.20) is a function of radius, ρ, (flux ψ) of magnetic surface and the length of field lines measured in the map steps N.

The quasiclassical formula for the Kolmogorov length $L_K(\rho)$ has been proposed by Ghendrih et.al. (1992, 1996),

$$L_{KQ}(\rho) = \pi q R_0 \left(\frac{\pi \sigma_{Chir}}{2}\right)^{-4/3}, \tag{4.21}$$

where σ_{Chir} is the Chirikov parameter defined by Eq. (4.2).

4.4.4 Numerical results

Below we present the Kolmogorov's lengths numerically calculated for the three operational regime: 12:4, 6:2 and 3:1 modes. They correspond to the

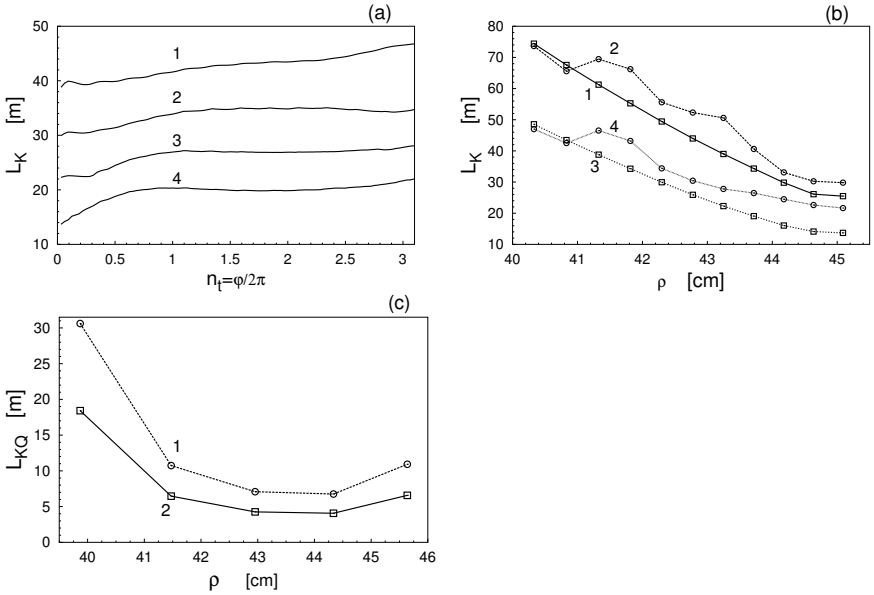

Fig. 4.14. Local Kolmogorov length $L_K(l)$ for the 12:4 mode. a) $L_K(l)$ vs the toroidal angle φ with a several initial radii: curve 1 corresponds to $\rho = 41.3$ cm; curve 2 – $\rho = 42.3$ cm; curve 3 – ρ =43.3 cm; curve 4 – $\rho = 45.1$ cm. The perturbation current $I_d = 15$ kA; b) Radial profiles of the Kolmogorov length $L_K(l)$ at different toroidal angles and perturbation currents: curves 1 and 3 correspond to $\varphi = 0$, curves 2 and 4 correspond to $\varphi = 6\pi$. Curves 1 and 2 correspond to $I_d = 7$ kA, curves 3 and 4 correspond to $I_d = 15$ kA. c) Quasiclassical formula for the Kolmogorov length L_{KQ}: curves 1 corresponds to $I_d = 7$ kA, curve 2 – to $I_d = 15$ kA. The equilibrium plasma parameters are the same as in Fig. 4.2.

plasma discharges whose Poincaré sections were shown in Figs. 4.2, 4.3, and 4.4, respectively.

The case of the 12:4 operational mode is shown in Fig. 4.14. The evolution of the local Kolmogorov length $L_K(l)$ along the toroidal angle φ is plotted in Fig. 4.14a at the four magnetic surface with radii $\rho = 41.3$ cm (curve 1), $\rho = 42.3$ cm (curve 2), ρ =43.3 cm (curve 3), and $\rho = 45.1$ cm (curve 4). The dependencies of $L_K(l)$ on the radii, ρ, of magnetic surfaces is shown in Fig. 4.14b for the two perturbation currents: $I_d = 7$ kA (curves 1 and 2) and $I_d = 15$ kA (curves 3 and 4). Curves 1 and 3 correspond to $L_K(l)$ at the beginning of evolution, i.e., $l \propto \varphi = 0$, while curves 2 and 4 correspond to $L_K(l)$ after three toroidal turns, i.e., $\varphi = 6\pi$. Finally, the corresponding quasilinear Kolmogorov length, L_{KQ}, given by Eq. (4.21) is plotted in Fig. 4.14c for the following perturbation currents: curve 1 corresponds to $I_d = 7$ kA and curve 2 corresponds to $I_d = 15$ kA. Similar plots for the operational modes 6:2 and 3:1 are shown in Fig. 4.15 and Fig. 4.16, respectively.

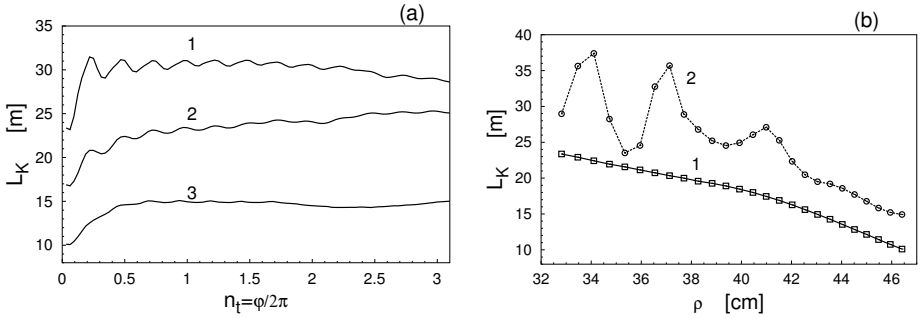

Fig. 4.15. The same as in Fig. 4.14 but for the 6:2 mode. a) curve 1 corresponds to $\rho = 32.8$ cm; curve 2 − $\rho = 41.5$ cm; curve 3 − $\rho = 46.4$ cm; b) Radial profiles of Kolmogorov length $L_K(l)$ at different toroidal angles: curve 1 corresponds to $\varphi = 0$, curve 2 corresponds to $\varphi = 6\pi$. The perturbation current $I_d = 7.5$ kA. The equilibrium plasma parameters are the same as in Fig. 4.3.

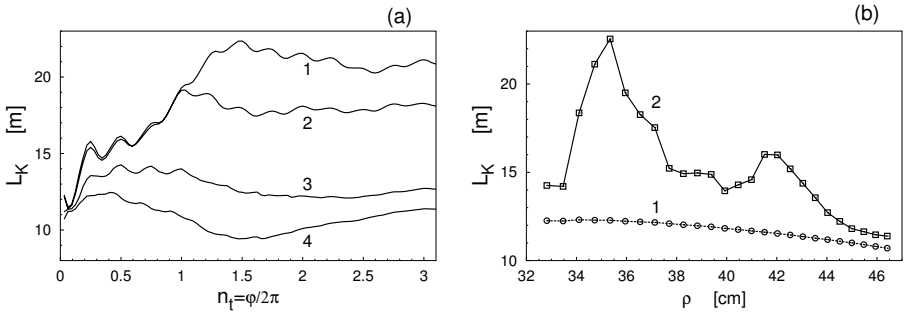

Fig. 4.16. The same as in Fig. 4.14 but for the 3:1 mode. a) curve 1 corresponds to $\rho = 34.7$ cm; curve 2 − ρ =36.5 cm; curve 3 − $\rho = 44.0$ cm; curve 4 − $\rho =$ 46.4 cm. The perturbation current $I_d = 3.75$ kA; b) Radial profiles of Kolmogorov length $L_K(l)$ at different toroidal angles perturbation currents: curve 1 corresponds to $\varphi = 0$, curve 2 corresponds to $\varphi = 6\pi$. The perturbation current $I_d = 3.75$ kA. The equilibrium plasma parameters are the same as in Fig. 4.4.

As seen from Figs. 4.14, 4.15, 4.16 the local Kolmogorov length, $L_K(l)$, depends on the radial positions of magnetic surfaces. The value of $L_K(0)$ monotonically decreases with increasing the radius (see, curves 1 and 3 in Figs. 4.14b, 4.15b, and curve 1 in Fig. 4.16b) where the perturbation field grows outwardly. Particularly, $L_K(0)$ does not depend on the structure of the stochastic layer. The influence of the latter starts to reveal on the radial profiles of the local Kolmogorov length, $L_K(l)$, with long field lines (see, curves 2 and 4). They have local maxima near the radial positions of the remnants of magnetic islands which are seen from the corresponding Poincaré sections in Figs. 4.2c, 4.3b, and 4.4b. This is because of the regular field lines in magnetic islands which effectively increase the statistical measure of e-folding length of

exponential divergence of neighboring field lines, i.e., the Kolmogorov length, $L_K(l)$.

One should note that the quasilinear Kolmogorov lengths, L_{KQ}, calculated using Eq. (4.21) (see, Fig. 4.14c) are larger than the numerically obtained Kolmogorov lengths, L_K, by a factor $2 \div 4$. Probably, it is due the fact the quasilinear theory is valid only for the highly developed stochastic layer in an unlimited domain, unlike the stochastic zone for field lines in the TEXTOR-DED. Nonetheless, the quasilinear formula (4.21) gives a right dependence of L_K on the perturbation current. Indeed, from Eq. (4.21) follows that $L_{KQ} \propto I_d^{-2/3}$, which is in a good agreement with numerical calculations. Particularly, from data plotted in Fig. 4.14b the ratio $\delta = L_K(I_d = 7kA)/L_K(I_d = 15kA)$ takes values in the interval [0.54, 0.65] which are close to the value 0.6 of the ratio $L_{KQ}(I_d = 7kA)/L_{KQ}(I_d = 15kA)$ predicted by the quasilinear formula. Similarly, for the 6:2 mode one finds that the ratio δ takes the values in the interval [0.47, 0.62] which close to the quasilinear value of δ=0.53.

4.5 Experimental observation of the magnetic structure

The model described in this work has been extensively tested against the experiments. Since the DED system produces a relatively simple perturbation field, it was possible to perform a direct comparisons between the plasma structures and modeled magnetic field topologies. The main limitation of the model comes from the linear addition of the applied perturbation and the magnetic equilibrium (so-called "vacuum" approximation). However, the overall agreement of the predicted structures and the measured data is very good. The general properties of the plasma edge resulting from the DED were predicted in detail demonstrating that the changes in transport can be understood with the knowledge of the calculated field line structures.

Fig.4.17a shows a false-color image of the CIII light emission, recorded by means of CCD camera equipped with an interference filter at $\lambda = 465$ nm, (#95592). The camera has a toroidal view, tangential to the inner wall (or divertor target plate) and observes the light pattern of CIII which is located near to the surface, around the equatorial midplane. Each frame is recorded for 8 ms. The figure clearly shows the effect of the near field of the DED resulting in a deformation of the flux zones to the wall. Superimposed to the figure is a Poincaré plot visualizing the structure of the perturbed volume. For the Poincaré plot magnetic field lines are analyzed for up to 15 poloidal turns. One observes that the distribution of the CIII spectral line intensity not only follows the symmetry of the perturbation field, but it strongly depends on the magnetic structures predicted by the model. Assuming the electron temperature $T_e \approx 70$ eV and electron density $n_e \approx 7 \cdot 10^{18}$ m^{-3} in the laminar zone gives mean free path of order of 10 meters, which is of the same order as the Kolmogorov length, L_K. The particles following the field lines hit the wall before the field lines can reveal a chaotic behavior. Therefore, the heat

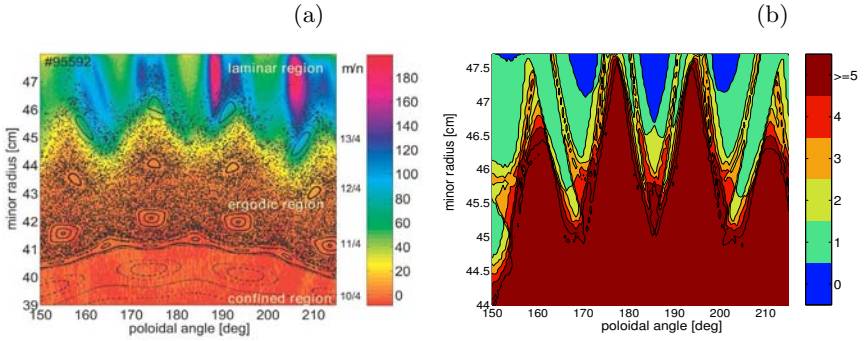

Fig. 4.17. a) The two-dimensional distribution of the CIII emission in the front of the DED coils for the discharge #95592 overlayed with the Poincaré section visualizing the calculated structure of the magnetic field. The colorbar indicates the intensity of the CIII line at 465 nm in the arbitrary units. The m/n numbers on the right hand side of the figure indicate the island chains. b) Corresponding laminar plot representing the contour plot of the field lines connection length calculated for the same conditions as in (4.17a) (Jakubowski et.al. (2005b)).

and particle deposition patterns are mainly driven by the laminar structures in the outermost plasma layer.

The regular patterns of heat deposition, which are formed by the laminar zone, have been identified since very first experiments with the DED (Jakubowski et.al. (2005a)). Two examples of the infrared images recorded by the infrared camera are shown in Figs. 4.18a-b. The images present the temperature distribution over the divertor target plates at (a) low and (b) high level of ergodization. The false color scale represents the temperature in centigrade degree. The plates are visible as a rectangles; each of them is attached to the vessel by two screws. Unfortunately, the structure of the heat flux deposition is affected by non-ideal alignment of the target plates. Protruding for 1-2 mm edges of the tiles, at190°, cause that some areas are shadowed from the heat flux and some of them are over-exposed. Since the angles of incidence of the field lines intersecting the DED wall are very shallow ($\sim 1°$), the heat distribution is strongly influenced.

The immanent features of the DED heat flux density pattern are the stripe-like structures parallel to the DED coils. One can see four pairs of strike zones formed by the incoming heat fluxes, where the half width of one of stripes is of order of 3 cm. At higher level of the ergodization each pair of the "power-stripes" contains a colder region in between (see Fig. 4.18b). At the lower degree of ergodization these pairs merge together (see Fig. 4.18a). The temperature distribution qualitatively resembles the footprint structure of the field lines on the divertor wall, which is presented in Figs. 4.18c-d.

To perform a direct comparison of the heat deposition pattern with the structure of magnetic footprints a heat flux profile along the poloidal angle

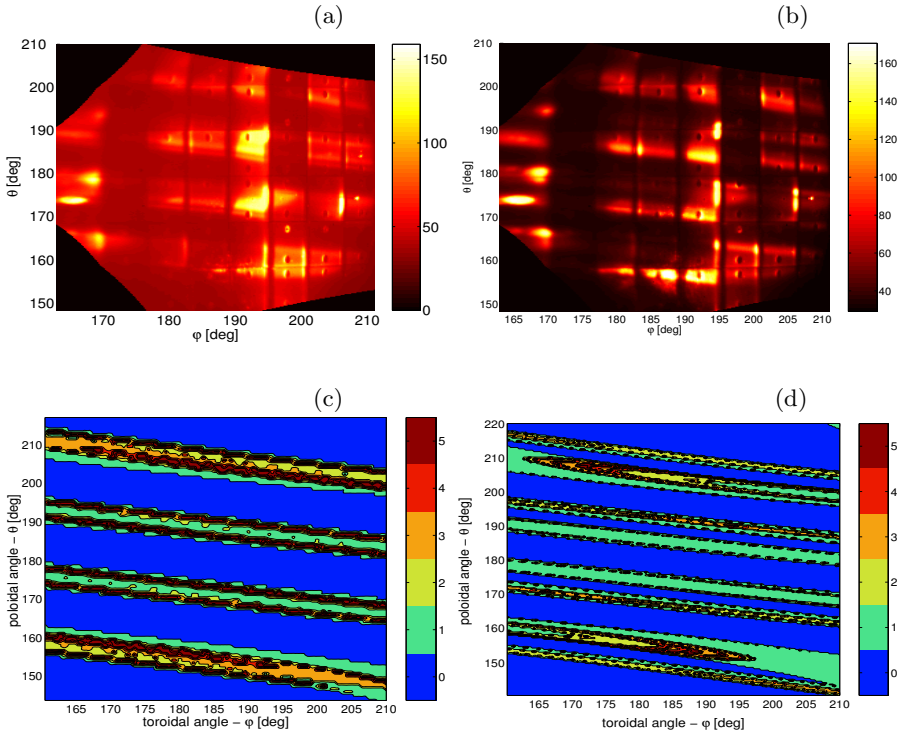

Fig. 4.18. a-b) Temperature distribution over the divertor target plates in the pressure measured by the infrared camera for (a) low and (b) high ergodization level in the 12/4 configuration; c-d) The magnetic footprints calculated for the temperature distribution shown above: case c) corresponds to Fig. 4.18a and case b) to Fig. 4.18b.

was evaluated (Jakubowski et.al. (2004)). In Fig. 4.19 the power flux profile calculated from the temperature evolution along the tiles at the toroidal angle $\varphi = 187°$ is shown. To avoid incidental changes of the profile an average over the whole time of the DED action was taken. For the same toroidal position the connection length profile along the DED tiles has been calculated. The abscissa represents the poloidal angle. The blue curve visualize the connection lengths of the magnetic field lines (values are on the left ordinate); the green line presents the heat fluxes towards the divertor target plates calculated from the temperature distribution (the right ordinate is the corresponding one). The power flux profile is in fair agreement with modeled connection length profile. Indeed the middle power flux stripes are composed of the two hotter "channels", where the heat is transported from the ergodic region to the divertor wall. The asymmetries in the power profiles are mainly caused by the geometrical imperfections of the wall components. The connection length profiles of the outer stripes are composed only from the field lines with $L_c > L_K$. Therefore the heat flux density distribution is more uniform. The heat

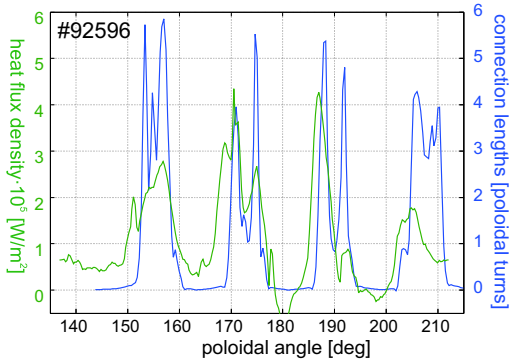

Fig. 4.19. Comparison of the magnetic structures predicted by the model and measured heat fluxes: the green curve presents the power flux profile evaluated with the THEODOR from the measured temperature distribution (the left ordinate); the blue curve (the left ordinate) represents the connection lengths of the field lines starting along the line, for which the power flux was evaluated.

flux density profiles are broader than the footprints, which is consistent with the assumption of a cross-field diffusion of the particles from the relatively thin fingers to the laminar zone. In the case presented here, the ergodic layer dominates the plasma edge. Most of the heat is brought from the plasma core to the wall by the field lines with relatively long connection lengths (more then 4 poloidal turns).

Results of extensive experiments in the TEXTOR-DED on the influence of magnetic perturbations created the DED on the plasma transport, divertor properties, plasma rotation are discussed by Finken et.al. (2004); Unterberg et.al. (2004); Lehnen et.al. (2005); Finken et.al. (2006); Wolf et.al. (2005).

5

Magnetic field structure obtained by means of the Gourdon code

In this chapter we briefly describe another method to study the ergodization of magnetic field lines in the TEXTOR-DED based on the numerical Gourdon code. This code developed by Gourdon (1970) uses the assumption that the equilibrium magnetic field and the radial perturbing field can be superimposed independently, the thus obtained total magnetic field vector can be used to track the field lines. The influence of the perturbation currents on the plasma equilibrium is neglected and ideal penetration of the perturbation field into the plasma is assumed. It integrates the equations (3.1) for field lines using the Adam integration scheme (see, e.g., Abramowitz and Stegun (1965), page 896).

The code requires the equilibrium magnetic field and the perturbation magnetic field field created by external coils. The first one is a solution of the Grad–Shafranov equation. The numerical solutions of the latter is given the DIVA equilibrium code by Zehrfeld (1999). The perturbation magnetic field is computed by means of Biot - Savart's formula. This field is stored on a spatial mesh set up in the (R, z, φ) domain which the field lines are expected not to leave. The field needed during field line tracing is computed by interpolating within the mesh.

The application of the Gourdon code to study the ergodization of field lines in the TEXTOR-DED has been given by Kaleck et.al. (1997); Finken et.al. (1998); Eich et.al. (1998, 2000); Kaleck (1999). Below we shortly describe the equilibrium calculations, the spectra of magnetic perturbations and some examples of Poincaré sections obtained by the Gourdon code.

5.1 Equilibrium calculation

The equilibrium calculation [see e.g. Nicolai (1989) for details] iterates between the $2D$ - Grad - Shafranov equation (GSE) and the flux surface averaged Grad - Shafranov equation. The GSE is given by

$$\Delta^* \psi = -\mu_0 R\, j_\varphi,$$

with the toroidal Laplace operator

$$\Delta^* = R^2 \boldsymbol{\nabla} \frac{1}{R^2} \boldsymbol{\nabla} = \frac{\partial^2}{\partial R^2} + \frac{\partial^2}{\partial z^2} - \frac{1}{R} \frac{\partial}{\partial R},$$

and the toroidal current density given by

$$\mu_0 R j_\varphi = -\mu_0 R^2 \frac{dp}{d\psi} - f \frac{df}{d\psi},$$

where $p = p(\psi)$ is the pressure profile and $f = f(\psi)$, the f function which is closely related to the to the $q-$ profile (see equation 5.2). The transport equations (or the experimental data) provide the pressure profile $p(\psi)$ and the $q-$ profile $q(\psi)$ which enter the ODE. This equation is obtained by averaging the Grad - Shafranov equation over the flux surfaces:

$$\left(K + \frac{Q^2}{A}\right) \bar{\psi}'' + \left[K' + \frac{\mu_0 p'}{\bar{\psi}'} + \frac{Q}{A}\left(Q' - \frac{A'Q}{A}\right)\right] \bar{\psi}' = 0 \qquad (5.1)$$

The following definitions were used:

$$\begin{aligned} Q &= (2\pi)^2 q, & K &= \left\langle \frac{|\boldsymbol{\nabla}\psi|^2}{R^2} \right\rangle, \\ A &= \left\langle \frac{1}{R^2} \right\rangle, & f(\psi) &= \frac{Q(\psi)}{A} \frac{d\psi}{dV}. \end{aligned} \qquad (5.2)$$

Here $\left\langle \right\rangle$ denotes the flux surface average, $\bar{\psi}$ the flux profile depending on the enclosed volume V and the prime denotes the derivative with respect to V. In the case of a force-free equilibrium the $f-$ function mainly determines the toroidal current density.

The equilibrium calculation iterates either between the ODE determining the flux profile $\bar{\psi}(V)$ and the PDE yielding the $2d-$ flux function $\psi(R, y)$ [as in Nicolai (1989)] or solves the PDE for a prescribed pressure profile $p(\bar{\psi})$ and $f-$ function $f(\bar{\psi})$ [as in Zehrfeld (1999)]. The outermost flux surface with the volume V_{max} is defined by the limiter or separatrix. The volume of this surface allows to computer the effective plasma radius given by

$$\rho_{max} = \sqrt{\frac{V_{max}}{2\pi^2 R_0}}, \qquad (5.3)$$

where R_0 is the radius of the magnetic axis. The effective radius ρ of an arbitrary flux surface with volume V is defined analogously (with V_{max} replaced by V).

The equilibrium contributions to the radial and vertical fields are

$$B_{R_{equ}} = -\frac{1}{R}\frac{\partial \psi}{\partial z}, \qquad B_{z_{equ}} = \frac{1}{R}\frac{\partial \psi}{\partial R}. \tag{5.4}$$

Thus the poloidal field is given by

$$B_p = \frac{|\nabla \psi|}{R}. \tag{5.5}$$

The toroidal field is related to the $f-$ function by

$$B_t = \frac{f(\bar{\psi})}{R}. \tag{5.6}$$

Finally we define the 'intrinsic' poloidal coordinate ϑ which is needed for the Fourier analysis, ϑ, is defined by

$$\frac{d\vartheta}{d\varphi} = \frac{1}{q}, \tag{5.7}$$

so that in (ϑ, φ) - coordinates the field - lines are straight. From the field line equation we get

$$\frac{d\theta}{d\varphi} = \frac{RB_p}{rB_t}. \tag{5.8}$$

Thus we obtain for the dependence of ϑ on θ the differential equation

$$\frac{d\vartheta}{d\theta} = \frac{1}{q}\frac{rB_t}{RB_p}, \tag{5.9}$$

which can be integrated numerically for a given equilibrium.

5.1.1 Fixed boundary value problem

The boundary values at a rectangular domain are prescribed such that the plasma boundary meets 8 prescribed positions [Nicolai (1989)] to describe $D-$ shaped (and thus also circular) tokamak plasmas. The boundary can be defined by two composed ellipses with the major half b in common and two different minor half-axis $a_1 < a_2$ this allows to define the elongation

$$\epsilon = \frac{b}{a}$$

with $a = a_1 + a_2$ and the excentricity,

$$e = \frac{a_2 - a_1}{a_2 + a_1},$$

in a simple way.

An analytic expression [Nicolai (1989)] is used to compute the boundary values. The parameters of this expressions are adjusted to obtain the aforementioned 8 positions.

5.1.2 Semifree boundary value problem

The current in the vertical field coils and in the shaping coils are adjusted such that the plasma boundary meets the outer limiter and upper limiter positions, respectively. The position of the inner rail - limiter is met by adjusting the plasma volume. We note that the 'inverse' equilibrium problem (with prescribed shape - parameters and the unknown coil currents) is in general 'ill - posed'.

5.1.3 Special equilibria

In the case of an equilibrium with a low poloidal $\beta_{pol} = 0.1$ (Fig. 5.1 a) (ϵ=1, $e = 0$ and ρ_{max}=50 cm), we see that the Shafranov - shift is small (Δ_{sh}=2.9 cm) and the flux surfaces are almost concentric circular tori.

For a large poloidal $\beta_{pol} \approx 1$ we have a big Shafranov - shift Δ_{sh}=8.7 cm and we get nested circular flux surfaces (Fig. 5.1 b) with a strong inside - outside asymmetry. In both cases the fixed boundary value problem was solved.

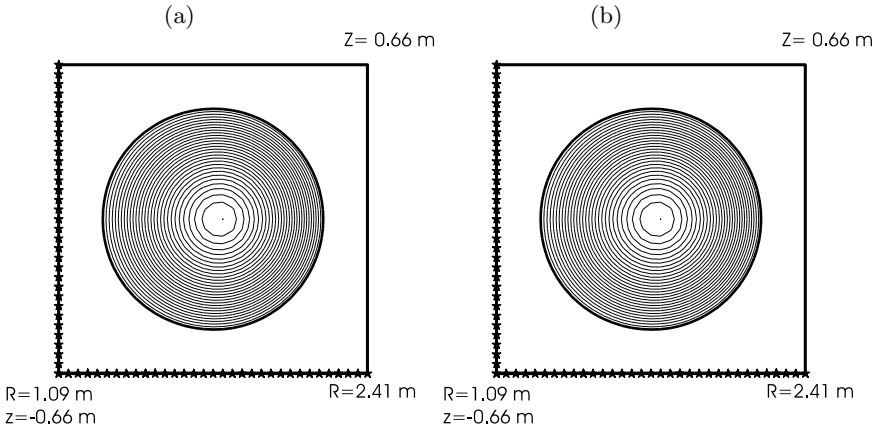

Fig. 5.1. a) Low β equilibrium (β_{pol}=0.1, I_p=450 kA, B_t=2.25 T) The flux surfaces are concentric circular tori. The Shafranov shift is small (Δ_{sh} = 2.9 cm) so that the centers of the flux surfaces almost coincide at R_0=175 cm. b) High β equilibrium ($\beta_{pol} \approx 1$, I_p=450 kA, B_t=2.25 T) The flux surfaces are circular tori as before, the Shafranov shift, however, is large (d_{sh}=8.7cm). Therefore there is a strong inside - outside asymmetry.

Since we have chosen a parabolic current distribution the $q-$ profile (see Fig. 5.2) starts with $q(\rho = 0) = 1.8$ and has the boundary value $q(\rho = 50$ cm$) = 4$ which is mainly determined by the plasma current and the toroidal magnetic field (I_p=450 kA, B_t=2.25 T). The transformer iron is simulated by a surface current density [Nicolai (1989)].

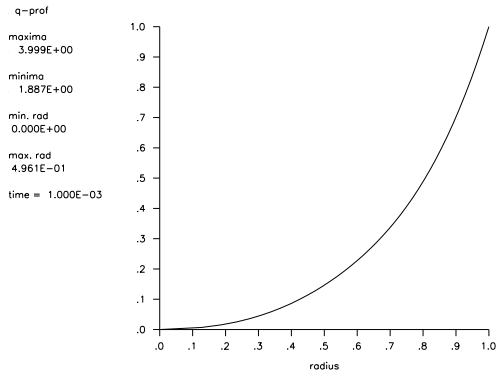

Fig. 5.2. Safety factor profile $q(\rho)$. Since a parabolic current distribution was chosen $q(\rho = 0) = 1.8$ is rather large. The boundary value $q(\rho = 50cm) = 4$ is mainly determined by the plasma current and the toroidal field (I_p=450 kA, B_t=2.25T).

5.2 Fourier analysis of the perturbing magnetic field

The Fourier sine - coefficients of the radial field B_r are given by

$$B_{mn}^{(s)} = \frac{1}{2\pi^2} \int_0^{2\pi} d\vartheta \int_0^{2\pi} d\varphi B_r(\theta, \varphi) \sin(m\vartheta - n\varphi). \tag{5.10}$$

An analogous formula holds for the cosine - coefficients $B_{mn}^{(c)}$. In the following the geometrical sum

$$B_{mn} = \sqrt{\left(B_{mn}^{(s)}\right)^2 + \left(B_{mn}^{(c)}\right)^2}, \tag{5.11}$$

of both is envisioned because this sum is decisive for the island width and is independent from the phase $\phi_{m,n} = \arctan\left(B_{mn}^{(c)}/B_{mn}^{(s)}\right)$. 100 grid points were chosen in the toroidal and in the poloidal directions, respectively.

Since B_r scales linearly with the currents in the helical coils I_d, the current I_d can be prescribed arbitrarily. The shape of the spectrum is not influenced by I_d. We note, that the spectra are computed for one specific flux surface, e.g. the $q = 3$ surface, with prescribed (effective) radius. Therefore the Poincaré plot with non overlapping islands, the mean width of which is proportional to $\sqrt{B_r}$, provides a more appropriate Fourier analysis since the field strength is computed at the specific flux surface.

5.3 Perturbation coils for the DED

The perturbation coils at TEXTOR are foreseen to have the dominant Fourier components in resonance with the $q = 3$ surface, i. e. the pitch of the conductors corresponds to the (mean) field line pitch at the $q = 3$ surface.

The winding is covered by carbon tiles the extension of which is indicated by the rectangle on top of each Poincaré plot. We note that the ALT II (pump-limiter) is sketched in the upper left corner of the same plot.

Due to the steps in upper and lower half of the winding these halves of the winding are magnetically not completely neutral, i.e. there are conductor sections with the current in the toroidal direction without the corresponding sections with the current in the opposite direction. It means that for the 12/4 - configuration the current,

$$4\left(\frac{1}{4}-\frac{1}{8}\right)I_d=\frac{1}{2}I_d,$$

is not compensated in the upper half. The impact of this current on the island configuration is given in the next section.

5.3.1 Magnetic fields generated by the DED

Using the torus coordinates, the radial and poloidal field component B_r and B_θ both depending on θ and φ can be computed. Fig. 5.3 a shows that the oscillations of B_r are roughly proportional to $\sin(12\theta-4\varphi)$. The poloidal field shows a similar behavior. Quite in contrast to the rapid oscillation of the

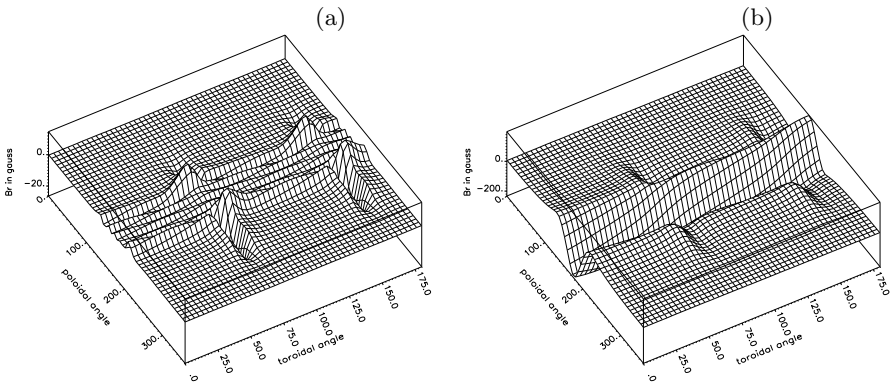

Fig. 5.3. (a) Radial field of the 12 : 4 configuration. The oscillation in θ and φ direction are roughly proportional to $\sin(12\theta-4\varphi)$. Outside the range of the DED the field vanishes. Therefore the spectrum (Fig. 5.4a) becomes broad in the poloidal mode number m. (b) Radial field of the 3 : 1 configuration. In contrast to the rapid oscillation of the radial field in the case of the 12 : 4 configuration the radial field of the 3 : 1 configuration (with the spectrum in Fig. 5.4 b) oscillates like $\sin(3\theta-\varphi)$, i. e. comparatively slowly.

radial field in the case of the 12 : 4 configuration the radial field of the 3 : 1 configuration (with the spectrum in Fig. 5.4 b) oscillates like $\sin(3\theta-\varphi)$, i. e. comparatively slowly (Fig. 5.3 b).

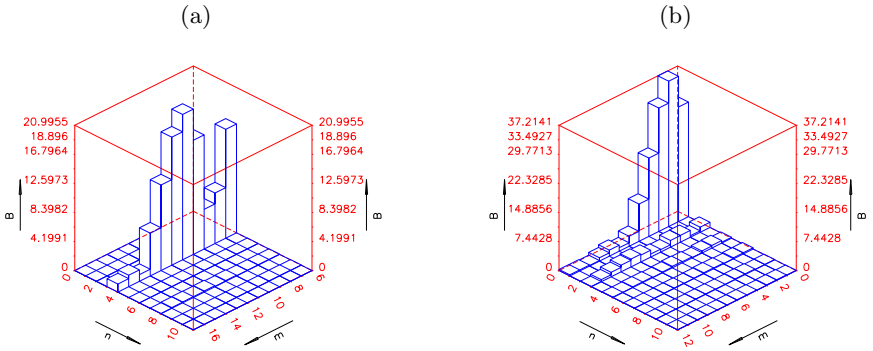

Fig. 5.4. a) Spectrum of the aforementioned configuration (12 : 4) at the $q = 3$ surface (I_d=7.5 kA). Only the ($m = 12, n = 4$) - component can be compared directly with the island width in Fig. 5.5b. In the case of the other island chains the spectrum must be recalculated at the respective flux surface; b) Spectrum of the configuration (3 : 1) at the $q = 3$ surface for I_d=1.5 kA. I_p and B_t are almost the same as before. We see that the component (m=2, n=1) is somewhat larger than the component (m=3, n=1) because of its better penetration.

5.3.2 Spectra

The DED-configuration generates the radial field B_r which depends mainly on the coil currents. Here we investigate the aforementioned cases (12:4) and (3:1).

($m = 12, n = 4$) configuration

This spectrum was computed at the $q = 3$ surface for the parameters $I_d = 7.5$ kA, $I_p = 400$ kA, $B_t = 1.9$ T). The spectrum is peaked at $m = 11$, $n = 4$ and has a minimum at $m = 9$. Since the winding is not interrupted toroidally, mainly $n = 4$ components are available. At $n = 8$ weak harmonics can be seen (Fig. 5.4 a).

(m=3, n=1) - configuration

The helical field of this configuration has the longest penetration length. Therefore it was under intensive experimental investigation. The spectrum (Fig. 5.4 b) peaks at m=2 because this amplitude penetrates better than $b_{3,2}$. The minimum of the spectrum (n=1) cannot be seen because it appears for negative m, corresponding to a reverted plasma current or a reverted toroidal field. This case, however is not discussed here. The uneven harmonics $n = 2, 4, 6, \ldots$ are excited because in the (m=3, n=1) case there is no symmetry with respect to the plane $\varphi = 0$.

5.4 Poincaré plots

These plots are obtained under the assumption that the winding does not have a periodicity. For each initial point 400 toroidal revolutions are are calculated. The initial points are in the vicinity of the equatorial plane and they are chosen to move radially (in the cylindrical coordinate system around the axis of symmetry) to the outside.

5.4.1 (m=12, n=4) configuration

The Poincaré plot (I_p=400 kA, B_t=1.9 T) without compensation coils (Fig. 5.5 a) reveals the jump in the island chain in crossing the $\theta = 180°$ as expected from the above considerations. Using the compensation coils with $I_{comp} = \frac{1}{2} I_d$ (Fig. 5.5 b) a chain of 12 islands which are aligned along the unperturbed q=3 surface is generated.

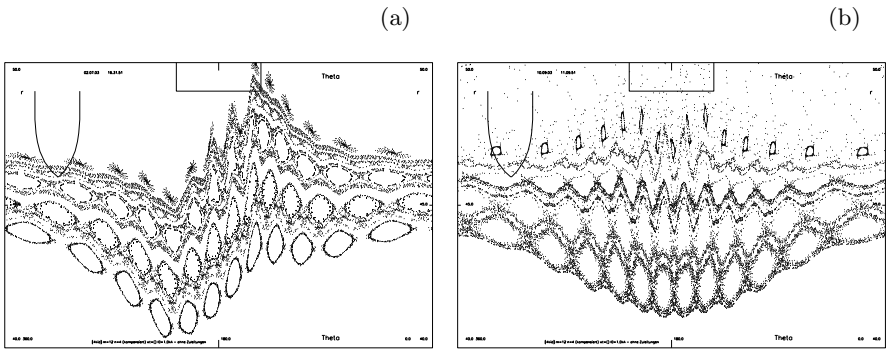

Fig. 5.5. a) Poincaré plot without currents in the compensation coils shows a pronounced step in the island chain (m=12, n=4); b) Poincaré plot with the currents $I_{comp} = I_d/2$ in the compensation coils (I_d=1.5 kA). The islands are now well aligned at the q=3 surface.

The (m=12, n=4), (m=13, n=4) (m=14, n=4), (m =15, n=4) island chains can be seen in accordance with the spectrum of the winding (Fig. 5.4 a).

5.4.2 (m=3, n=1 - configuration

The Poincaré plot (Fig. 5.6 a) shows big islands at the $q = 2$ - surface underlining the good penetration ability of this mode. The $\frac{5}{2}$ - and the $\frac{7}{3}$ - island chain have according to the spectrum a small width. The islands at $q = 3$ are embedded in an ergodic sea which arises by the interaction with the $q = 4$ islands which are shown in Fig. 5.6 b. There the field line tracing (at reduced

(a) (b)

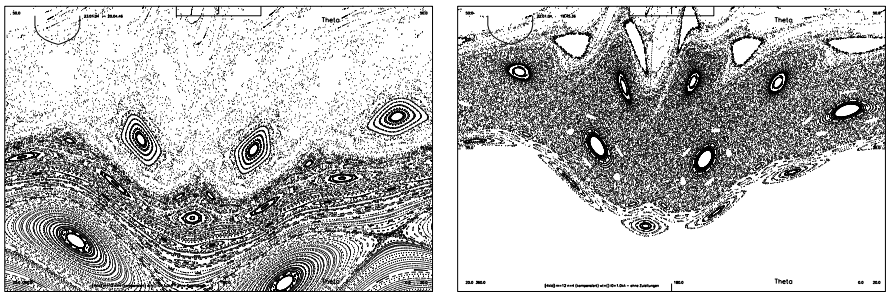

Fig. 5.6. a) The Poincaré plot of the configuration ($m = 3, n = 1$) (I_d=3 kA) shows large islands at the $q = 2$ and the q= 3 surface. Also the (5 : 2) island chain can be seen. The islands at the $q = 3$ surface seem to be embedded in an ergodic sea because helical field increases strongly in approaching the DED. A calculation with slightly different equilibrium confirms this (Fig. 5.6); b) The Poincaré plot of the configuration ($m = 3, n = 1$) (I_d=3 kA, I_p=315 kA) shows residual islands at the q = 3 and the q= 4 surface. Also the strongly distorted q=5 island chain can be seen. The islands are embedded in an ergodic sea because helical field increases strongly in approaching the DED.

plasma current I_p=315 kA) was shifted to the region 35 cm $< r <$ 50cm. The strongly distorted $q = 5$ islands can be seen as well.

A

Calculations of amplitudes and phases in Eq. (2.4)

Eq. (2.4) can be presented in the following complex form

$$I_j = \frac{I_d}{2} \sum_{n=-\infty}^{\infty} \iota_n e^{in2\pi j/16 + i\tilde{\chi}_n}. \tag{A.1}$$

where

$$\tilde{\chi}_n = (\chi_n - \pi/2) \begin{cases} 1, & \text{for } n > 0 \\ -1, & \text{for } n < 0 \end{cases}.$$

Using the formula

$$\sum_{j=1}^{N} e^{i(n-n')2\pi j/N} = N\delta_{nn'},$$

we obtain the following formula for the coefficients $\tilde{\iota}_n$:

$$\iota_n e^{i\tilde{\chi}_n} = \frac{1}{8I_d} \sum_{j=1}^{16} I_j e^{-in2\pi j/16}. \tag{A.2}$$

A.1 The 3:1 operational mode

The case 1. Consider the first case of current distribution (2.5). Inserting the last one into Eq. (A.2) we have

$$\iota_n e^{i\tilde{\chi}_n} = \frac{1}{8}\left[\sum_{j=1}^{8} e^{-in2\pi j/16} - \sum_{j=9}^{16} e^{-in2\pi j/16}\right] = \frac{1}{8I_d}\left[1 - e^{-in\pi}\right] \sum_{j=1}^{8} e^{-in2\pi j/16}$$

$$= \frac{1}{8} e^{-in\pi/8}\left[1 - (-1)^n\right] \sum_{j=0}^{7} e^{-in2\pi j/16} = \frac{1}{8} e^{-in\pi/8}\left[1 - e^{-in\pi}\right] \frac{1 - e^{-in\pi}}{1 - e^{-i2n\pi/16}}$$

$$= \frac{1}{16} e^{-i\pi/2 - in\pi/16} \frac{(1 - (-1)^n)^2}{\sin(n\pi/16)}.$$

From the last expression we obtain the following non-zero components of the amplitude, ι_n and the phase $\tilde{\chi}_n$ or (χ_n):

$$\iota_{2s+1} = \frac{1}{4\sin(n\pi/16)}, \qquad \tilde{\chi}_{2s+1} = -\frac{\pi}{2}\left(1 + \frac{(2s+1)}{8}\right),$$
$$\chi_{2s+1} = -\frac{(2s+1)\pi}{16}, \qquad s = 0, 1, 2, 3. \tag{A.3}$$

Particularly,

$$\iota_1 = \frac{1}{4\sin(\pi/16)} = 1.2814577, \qquad \chi_1 = \frac{7\pi}{16},$$
$$\iota_3 = \frac{1}{4\sin(3\pi/16)} = 0.44998811, \qquad \chi_3 = -\frac{11\pi}{16}, \tag{A.4}$$

The finite number of terms in Eq. (2.4) gives the exact values of I_j:

$$I_j = I_d \sum_{s=1}^{3} \iota_{2s+1} \sin\left((2s+1)\frac{2\pi j}{16} + \chi_{2s+1}\right), \qquad 1 \le j \le 16. \tag{A.5}$$

The case 2. Using the current distribution Eq. (2.9) we have

$$\iota_n e^{i\bar{\chi}_n} = \frac{x(1-x^8)(1-x^4)}{8(1-x)}, \qquad x = e^{-i2\pi n/16}.$$

It is easy to see that

$$x^8 = (-1)^n, \qquad 1 - x^8 = 1 - (-1)^n = \begin{cases} 2, & \text{for } n = 2k+1 \\ 0, & \text{for } n = 2k \end{cases}$$

$$1 - x^4 = x^2(x^{-2} - x^2) = 2ie^{-i\pi n/4}\sin(\pi n/4),$$
$$1 - x = x^{1/2}(x^{-1/2} - x^{1/2}) = 2ie^{-i\pi n/16}\sin(\pi n/16).$$

The non-zero terms are

$$\iota_n e^{i\bar{\chi}_n} = e^{-i5\pi n/16}\frac{\sin(\pi n/4)}{4\sin(\pi n/16)}, \text{ for } n = 2s+1, \text{ (s=0, 1, 2, } \dots).$$

or

$$\iota_{2s+1} = \frac{\sin(\pi(2s+1)/4)}{4\sin(\pi(2s+1)/16)}, \qquad \chi_{2s+1} = \frac{\pi}{16}(3 - 10s). \tag{A.6}$$

Particularly, we have

$$\iota_1 = \frac{\sin(\pi/4)}{4\sin(\pi/16)}, \qquad \chi_1 = \frac{3\pi}{16}.$$

By similar calculations one finds the Fourier coefficients τ_k and phases χ_k for the current distributions of the DED coils for the 6:2 and 12:4 operational modes.

B

Current density of coils

B.1 Continuous current density

Using the coil positions (2.1), (2.2) we present the current distribution given by Eq. (2.31) as

$$j^{(n)}(r,\theta,\varphi) = \delta(r-r_c)\frac{I_d}{r_c}g(\theta,\varphi)\sum_{j=-\infty}^{\infty}\sin\left(n\frac{2\pi j}{16}+\chi_n\right)\delta\left(\theta-\theta_\varphi+j\delta\theta\right), \tag{B.1}$$

where θ_j is a poloidal position of the $j-$th coil at the toroidal section $\varphi = 0$, i.e.,

$$\begin{aligned}\theta_j &= \theta_{01} - (j-1)\delta\theta - \frac{\theta_c}{\pi}\varphi = \theta_\varphi - j\delta\theta,\\ \theta_\varphi &= \theta_{01} + \delta\theta - \frac{\theta_c}{\pi}\varphi = \theta_0 - \frac{\theta_c}{\pi}\varphi,\\ \theta_0 &= \theta_{01} + \delta\theta.\end{aligned} \tag{B.2}$$

The angle θ_{01} is a poloidal position of the first coil at the toroidal section $\varphi = 0$.

Using the representation of delta function

$$\delta(x) = \frac{1}{2\pi}\int_{-\infty}^{\infty} e^{ixp}dp,$$

one write

$$j^{(n)}(r,\theta,\varphi) = \delta(r-r_c)\frac{I_d}{2\pi r_c}g(\theta,\varphi)$$
$$\times\mathrm{Im}\left\{e^{i\chi_n}\int_{-\infty}^{\infty}dpe^{ip(\theta-\theta_\varphi)}\sum_{j=-\infty}^{\infty}\exp\left[ij\left(\frac{2\pi n}{16}+p\delta\theta\right)\right]\right\}.$$

Using the Poisson rule

$$\sum_{j=-\infty}^{\infty} e^{i2\pi jx} = \sum_{s=-\infty}^{\infty} \delta(s-x),$$

one obtains

$$j(r,\theta,\varphi) = \delta(r-r_c)g(\theta,\varphi)\frac{I_d}{2\pi r_c}$$

$$\times \mathrm{Im}\left\{ e^{i\chi_n} \int_{-\infty}^{\infty} dp e^{i(\theta-\theta_\varphi)p} \sum_{s=-\infty}^{\infty} \delta\left(s - \frac{n}{16} - p\frac{\delta\theta}{2\pi}\right)\right\}$$

$$= \delta(r-r_c)g(\theta,\varphi)\frac{I_d}{r_c\delta\theta}\mathrm{Im}\left\{ e^{i\chi_n} \sum_{s=-\infty}^{\infty} e^{i2\pi(s-n/16)(\theta-\theta_\varphi)/\delta\theta}\right\}$$

$$= \delta(r-r_c)g(\theta,\varphi)\frac{2m_0 I_d}{\pi r_c} \sum_{s=-\infty}^{\infty} \sin\left(\frac{2\pi(s-n/16)}{\delta\theta}(\theta-\theta_\varphi)+\chi_n\right). \quad \text{(B.3)}$$

Using the dependence of θ_φ on φ given in Eq. (B.2) we obtain the relation (2.32)

B.2 Nonideal coil configuration

Consider the integral

$$f_{m,\hat{n}} = \frac{1}{(2\pi)^2} \int_0^{2\pi}\int_0^{2\pi} d\theta d\varphi g(\theta,\varphi) e^{-im\theta - i\hat{n}\varphi}.$$

Using the definition of the function $g(\theta,\varphi)$ (2.44), (2.45), (2.46) and integrating with respect to θ it is reduced to

$$f_{m,\hat{n}} = e^{im\pi}\frac{i}{(2\pi)^2 m}\int_0^{2\pi} d\varphi e^{-i\hat{n}\varphi}\left(e^{-im\theta_c(\varphi)} - e^{im\theta_c(\varphi)}\right).$$

One can show that

$$\int_0^{2\pi} d\varphi e^{-i\hat{n}\varphi} e^{\pm im\theta_c(\varphi)} = \delta_{\hat{n},4s}\exp\left[\pm im\left(\theta_{c0} - \frac{\Delta\theta}{2}\right) - i\hat{n}\left(\varphi_c - \frac{\pi}{4}\right)\right]$$

$$\times \frac{8\sin[(\hat{n} \pm m\alpha)\pi/4]}{\hat{n} \pm m\alpha}, \qquad s = 0, \pm 1, \pm 2, \ldots, \text{(B.4)}$$

where $\alpha = 2\Delta\theta/\pi$, $\delta_{n,k}$ is the Kronecker symbol, i.e., $\delta_{n,k} = 0$ for $n \neq k$ and $\delta_{n,n} = 1$. Introducing a notation $\theta_c = \theta_{c0} - \Delta\theta/2$, we obtain the coefficients $f_{m\hat{n}}$

$$f_{m\hat{n}} = -e^{-i\pi m}\delta_{\hat{n},4s}e^{-i\hat{n}\varphi_c} \ \frac{2\sin(m\alpha\pi/4)}{\pi^2 m} \times \frac{2[i\hat{n}\cos(m\theta_c) + m\alpha\sin(m\theta_c)]}{\hat{n}^2 - (m\alpha)^2}. \qquad \text{(B.5)}$$

According to Eq. (2.36) we obtain the following expression for the Fourier components of the current density $j_{m\hat{n}}(r)$,

$$j_{m\hat{n}}(r)e^{i\chi_{m\hat{n}}} = \delta(r - r_c)e^{i\chi_0^{(n)}}J_0 \ \ f_{m-nm_0/4,\hat{n}-n}. \qquad \text{(B.6)}$$

From Eq. (B.6) follows that due to nonideal configuration the current distribution (2.32) creates the toroidal modes $\hat{n} = n + 4s$, $(s = 0, \pm 1, \pm 2, \ldots)$.

The main contribution to the toroidal spectrum $\hat{n}$ comes from the terms $\hat{n} = n$. In this case $s = 0$, and one obtains

$$f_{m,0} = e^{-i\pi m}\frac{\sin[\pi m\alpha/4]}{\pi m\alpha/4} \ \ \frac{\sin(m\theta_c)}{m\pi}, \qquad \text{(B.7)}$$

and from Eq. (B.6) we obtain

$$j_{m\hat{n}}(r) = \delta(r - r_c)J_0 g_m C_m,$$
$$\chi_{m\hat{n}} = -\chi_0^{(n)} + \frac{\pi n m_0}{4} = -\chi_n + \frac{nm_0}{4}(\pi - \theta_0) + \frac{\pi}{2}, \qquad \text{(B.8)}$$

where g_m is given by Eq. (2.42), and

$$C_m = \frac{\sin[\pi(m - nm_0/4)\alpha/4]}{\pi(m - nm_0/4)\alpha/4} = \frac{\sin[(m - nm_0/4)\Delta\theta/2]}{(m - nm_0/4)\Delta\theta/2} \qquad \text{(B.9)}$$

is a correction factor due to nonideal configuration. For the ideal configuration $\alpha = 0$ and therefore $C_m = 1$.

One should note that the current distribution (2.3) with $n = 4$ creates also the toroidal mode $\hat{n} = 0$. (see Eq. (B.6)). This mode may disturb the plasma equilibrium. For this reason in the $m : n$=12:4 operational mode of the TEXTOR-DED one applies the compensation coils which annuls the effect of the $\hat{n} = 0$ mode.

C

Modified Bessel functions $I_m(z)$ and $K_m(z)$

For small arguments, $z < 1$, the Bessel functions and their derivatives have the following asymptotics (see Abramowitz and Stegun (1965)) :

$$I_m(z) = \frac{1}{\Gamma(m+1)}\left(\frac{z}{2}\right)^m\left(1 + \frac{1}{m+1}\frac{z^2}{4} + \frac{1}{2(m+1)(m+2)}\frac{z^4}{16} + \dots\right),$$

$$K'_m(z) = -\frac{m}{4}\Gamma(m)\left(\frac{z}{2}\right)^{-m-1}.\left(1 - \frac{m-2}{m(m-1)}\frac{z^2}{4} + \frac{m-4}{2m(m-1)(m-2)}\frac{z^4}{16} + \dots\right).$$

The product of these functions with different arguments has the following asymptotics

$$K'_m(z_0)I_m(z) \approx -\frac{1}{2z_0}\left(\frac{z}{z_0}\right)^m(1+C)\,, \tag{C.1}$$

where

$$C = \frac{1}{m+1}\frac{z^2}{4} - \frac{m-2}{m(m-1)}\frac{z_0^2}{4} + \frac{1}{2m(m+1)(m+2)}\frac{z^4}{16} + \frac{(m-4)}{2m(m-1)(m-2)}\frac{z_0^4}{16} - \frac{(m-2)}{m(m^2-1)}\frac{z^2 z_0^2}{16} + \cdots.$$

For large mode numbers, $m \gg 1$, the term C can be neglected.

D

Model of a current density profile $j(r)$ in the DED operation

Suppose that $j(r)$ is given by

$$j(r) = \begin{cases} j_0 + (j_q - j_0)\left(\frac{r}{r_q - w}\right)^{\nu_i}, & \text{for } r < r_q - w, \\ j_q, & \text{for } r_q - w < r < r_q + w, \\ j_q\left(\frac{a-r}{a-r_q-w}\right)^{\nu_o}, & \text{for } r_q + w < r < a \end{cases} . \quad \text{(D.1)}$$

The current flowing inside the magnetic surface of radius r,

$$I(r) = 2\pi \int_0^r j(r')r'dr', \quad \text{(D.2)}$$

is

$$I(r) = \pi r^2 \left(j_0 + \frac{2(j_q - j_0)}{\nu_i + 2}\left(\frac{r}{r_q - w}\right)^{\nu_i}\right) \equiv I_1(r), \quad \text{for } r < r_q - w, \quad \text{(D.3)}$$

$$I(r) = I_1(r_q - w) + \pi j_q\left(r^2 - (r_q - w)^2\right) \equiv I_2(r), \quad \text{for } r_q - w < r < r_q + w, \quad \text{(D.4)}$$

$$I(r) = I_2(r_q + w) + 2\pi j_q\left[\frac{a(a - r_q - w)}{\nu_o + 1}\left\{1 - \left(\frac{a-r}{a-r_q-w}\right)^{\nu_o+1}\right\} - \frac{(a - r_q - w)^2}{\nu_o + 2}\left\{1 - \left(\frac{a-r}{a-r_q-w}\right)^{\nu_o+2}\right\}\right], \quad \text{for } r_q + w < r < a. \quad \text{(D.5)}$$

The full plasma current I_p is given by

$$I_p = I(a) = I_2(r_q + w) + 2\pi j_q(a - r_q - w)\left[\frac{a}{\nu_o + 1} - \frac{a - r_q - w}{\nu_o + 2}\right]$$
$$= \pi(r_q - w)^2\left(j_0 + \frac{2(j_q - j_0)}{\nu_i + 2}\right) + 4\pi j_q r_q w + 2\pi j_q(a - r_q - w)$$
$$\times\left[\frac{a}{\nu_o + 1} - \frac{a - r_q - w}{\nu_o + 2}\right]. \tag{D.6}$$

We suppose that the following parameters, the full plasma current I_p, the minor radius, r_q, of the magnetic surface $q = 2$, its a half width, w, the value of the safety factor at the magnetic axis, q_0, are given. The parameters j_0 and j_p in the current density distribution (D.1) should be determined from the above parameters.

The safety factor $q(r)$ is given by

$$q(r) = \frac{I_t}{I(r)}\frac{r^2}{R^2(r)}\left(1 + \frac{a_2}{2}\frac{r^2}{R^2(r)} + \frac{3a_4}{8}\frac{r^4}{R^4(r)}\right),$$

where

$$R(r) = \left[R_0^2 + (\Lambda + 1)(a^2 - r^2)\right]^{1/2}.$$

Near the magnetic axis $r \to 0$ we have $I(r) = \pi j_0 r^2$,

$$q(0) = \frac{I_t}{\pi j_0 R^2(0)} \equiv q_0.$$

Therefore we have

$$j_0 = \frac{I_t}{\pi q_0 R^2(0)}.$$

The second parameter j_q is determined from (D.6):

$$I_p = \pi(r_q - w)^2 j_0\left(1 - \frac{2}{\nu_i + 2}\right)$$
$$+2\pi j_p\left\{\frac{(r_q - w)^2}{\nu_i + 2} + 2r_q w + (a - r_q - w)\left[\frac{a}{\nu_o + 1} - \frac{a - r_q - w}{\nu_o + 2}\right]\right\}.$$

or

$$j_q = \frac{I_p - \pi(r_q - w)^2 j_0\left(1 - \frac{2}{\nu_i + 2}\right)}{2\pi\left\{\frac{(r_q - w)^2}{\nu_i + 2} + 2r_q w + (a - r_q - w)\left[\frac{a}{\nu_o + 1} - \frac{a - r_q - w}{\nu_o + 2}\right]\right\}}. \tag{D.7}$$

E

Asymptotic estimation of the integral $S_{mm'}$ (3.44)

We write down the integral (3.44) as the Fourier integral

$$S_{mm'}(\psi) = \frac{1}{2\pi}\int_0^{2\pi} f(\vartheta)e^{im'\Phi(\vartheta)}d\vartheta, \tag{E.1}$$

where

$$\Phi(\vartheta) = \theta(\vartheta) - \frac{m}{m'}\vartheta, \qquad f(\vartheta) = 1 + \varepsilon\cos\theta(\vartheta)$$

are slowly varying functions of ϑ. Integrals of type (E.1) may be evaluated using the methods of asymptotic expansions in a series of inverse powers of $m' \gg 1$. However, as we will see below, the method of stationary phase cannot be directly applied to estimate the integral (E.1) for the values ofm' being of interest because of the specific behavior of the phase function $\Phi(\vartheta)$.

According to the localization principle (see Fedoryuk (1989)) for $m' \gg 1$ the integral (E.1) is equal to sum of the contributions at the critical points for $S_{mm'}$. There are two critical points for the phase function $\Phi(\vartheta)$:

$$\vartheta_1 = 0, \qquad \vartheta_2 = \pi.$$

As will be shown below, for $m' < m$ the main contribution to the integral comes from the first critical point, ϑ_1, and for $m' > m$ the second critical point contributes to the integral.

Consider first the case $m' > m$. One can expand the angle θ in terms of $(\vartheta - \pi)$ around the second critical point $\vartheta_2 = \pi$:

$$\theta(\vartheta) \approx \pi + \beta_1(\vartheta - \pi) + \frac{1}{6}\beta_3(\vartheta - \pi)^3, \tag{E.2}$$

where β_1, β_3 are defined by (3.45). In (E.2) we have taken into account that $d^2\theta/d\vartheta^2\Big|_{\theta=\pi} = 0$. Since $0 < \beta_1 < 1$ and $\beta_3 > 0$ the first derivative

$$\frac{d\Phi(\vartheta)}{d\vartheta} = (\beta_1 - m/m') + \frac{1}{2}\beta_3(\vartheta - \pi)^2,$$

has two real zeros

$$\vartheta_{1,2} = \pi \pm \left(\frac{2|m'\beta_1 - m|}{m'\beta_3}\right)^{1/2},$$

for $m' < m/\beta_1$, and complex roots for $m' > m/\beta_1$. When the values of m' which are sufficiently close to m/β_1 the singular points $\vartheta_{1,2}$ are close to each other, and the integral cannot be estimated by the ordinary method of stationary phase. In the case of degenerate stationary points one should apply the method described by Fedoryuk (1989).

Using the expansion (E.2), and introducing the integration variable $x = \vartheta - \pi$, the integral (E.1) may be written as

$$S_{mm'} = (-1)^{m+m'}\frac{1}{2\pi}\int_{-\pi}^{\pi} f(x+\pi)e^{i\lambda(\alpha x + x^3/3)}dx \tag{E.3}$$

where

$$\alpha = \frac{m'\beta_1 - m}{m'\beta_3/2}, \qquad \lambda = m'\beta_3/2.$$

For large values of λ and for the small values of α, the leading term of the asymptotic expansion of the integral (E.3) may be estimated by replacing $f(x+\pi)$ by $f(\pi)$ and expressing the integral by the Airy function $\mathrm{Ai}(z)$:

$$\begin{aligned} S_{mm'}(\psi) &= f(\pi)(-1)^{m+m'}\frac{1}{2\pi}\int_{-\pi}^{\pi} e^{i\lambda(\alpha x + x^3/3)}dx \\ &= (-1)^{m+m'}\left(\frac{2}{\beta_3 m'}\right)^{1/3}\mathrm{Ai}\left(\frac{\beta_1 m' - m}{(\beta_3 m'/2)^{1/3}}\right), \end{aligned} \tag{E.4}$$

where

$$\mathrm{Ai}(z) = \frac{1}{\pi}\int_0^{\infty}\cos(zt + t^3/3)dt$$

is the Airy function (Abramowitz and Stegun (1965)).

The asymptotic formula (E.4) is valid for small values of α. Comparison with the exact numerical calculations of the integral (E.1) shows that (E.4) is a good approximation for $S_{mm'}$ in the interval

$$m' - m/\beta_1 > -c(m'\beta_3/2)^{1/3}. \tag{E.5}$$

where $c \approx 3$.

A similar asymptotic estimation of $S_{mm'}$ can be obtained for the small values of m' satisfying the condition

$$m' - m/\gamma_1 < c(m'|\gamma_3|/2)^{1/3}. \tag{E.6}$$

There is the following formula for these m':

$$S_{mm'}(\psi) = f(0)\left(\frac{2}{|\gamma_3|m'}\right)^{1/3} \mathrm{Ai}\left(-\frac{\gamma_1 m' - m}{(|\gamma_3|m'/2)^{1/3}}\right), \tag{E.7}$$

where $\gamma_1 > 1$ and $\gamma_3 < 0$ are defined by (3.45).

Outside the intervals (E.4) and (E.5) the integrals $S_{mm'}(\psi)$ may be estimated by the method of stationary phase. These integrals are fast oscillating functions of m', and have an order of $(m')^{-1/2}$. We will not evaluate them here because of their small contribution.

The formulas (E.4) and (E.7) are the leading terms of an asymptotic expansion into a series of inverse powers of m'. The full asymptotic expansions may be found by the method described in Ref. Fedoryuk (1989).

F

The calculation of the Jacobi matrix

Consider the mapping (3.21)– (3.23) determined by the generating function (3.26). Use the presentation of the mapping in the form

$$\hat{M} = \hat{T}_{-}\hat{T}_0\hat{T}_{+}, \tag{F.1}$$

of three successive mappings, $\hat{T}_{-}\hat{T}_0\hat{T}_{+}$, each of them are given by Eqs. (3.21), (3.22) and (3.23), respectively. Then the Jacobian matrix (4.13) can be written as a product of three Jacobian matrices, corresponding to three successive mappings,

$$\mathbf{J}_k = \hat{M}_{k+1}\hat{M}_0\hat{M}_k, \tag{F.2}$$

where

$$\hat{M}_k = \begin{pmatrix} \frac{\partial J_k}{\partial \psi_k} & \frac{\partial J_k}{\partial \vartheta_k} \\ \frac{\partial \bar{\psi}_k}{\partial \psi_k} & \frac{\partial \bar{\psi}_k}{\partial \vartheta_k} \end{pmatrix}, \tag{F.3}$$

$$\hat{M}_0 = \begin{pmatrix} \frac{\partial J_k}{\partial J_k} & \frac{\partial J_k}{\partial \bar{\psi}_k} \\ \frac{\partial \bar{\psi}_k}{\partial J_k} & \frac{\partial \bar{\psi}_k}{\partial \bar{\psi}_k} \end{pmatrix} = \begin{pmatrix} 1 & 0 \\ \omega'(J_k)(t_{k+1}-t_k) & 1 \end{pmatrix}, \tag{F.4}$$

$$\hat{M}_{k+1} = \begin{pmatrix} \frac{\partial \psi_{k+1}}{\partial J_k} & \frac{\partial \psi_{k+1}}{\partial \bar{\psi}_k} \\ \frac{\partial \vartheta_{k+1}}{\partial J_k} & \frac{\partial \vartheta_{k+1}}{\partial \bar{\psi}_k} \end{pmatrix}. \tag{F.5}$$

The derivatives in the matrices (F.3), (F.5) are easily calculated from the mappings given by Eq. (3.21) and Eq. (3.23):

$$\begin{aligned} \frac{\partial J_k}{\partial \psi_k} &= \frac{1}{1+\epsilon A_{12}(t_k)}, \qquad \frac{\partial J_k}{\partial \vartheta_k} = -\frac{\epsilon A_{22}(t_k)}{1+\epsilon A_{12}(t_k)}, \\ \frac{\partial \psi_k}{\partial \psi_k} &= \frac{\epsilon A_{11}(t_k)}{1+\epsilon A_{12}(t_k)}, \qquad \frac{\partial \psi_k}{\partial \vartheta_k} = 1+\epsilon A_{12}(t_k) - \frac{\epsilon^2 A_{11}(t_k)A_{22}(t_k)}{1+\epsilon A_{12}(t_k)}, \end{aligned} \tag{F.6}$$

$$\frac{\partial\psi_{k+1}}{\partial J_k} = 1 + \epsilon A_{12}(t_{k+1}) - \frac{\epsilon^2 A_{11}(t_{k+1})A_{22}(t_{k+1})}{1+\epsilon A_{12}(t_{k+1})}, \qquad \frac{\partial\psi_{k+1}}{\partial\bar{\psi}_k} = \frac{\epsilon A_{22}(t_{k+1})}{1+\epsilon A_{12}(t_{k+1})},$$
$$\frac{\partial\vartheta_{k+1}}{\partial J_k} = -\frac{\epsilon A_{11}(t_{k+1})}{1+\epsilon A_{12}(t_{k+1})}, \qquad \frac{\partial\vartheta_{k+1}}{\partial\bar{\psi}_k} = \frac{1}{1+\epsilon A_{12}(t_{k+1})}, \tag{F.7}$$

where

$$A_{11}(t) = \frac{\partial^2 S_1(\vartheta, J, t, t_0)}{\partial J^2}, \qquad A_{12}(t) = \frac{\partial^2 S_1(\vartheta, J, t, t_0)}{\partial J \partial\vartheta},$$
$$A_{22}(t) = \frac{\partial^2 S_1(\vartheta, J, t, t_0)}{\partial\vartheta^2}. \tag{F.8}$$

References

Finken, K.H. (ed.) (1997) "Dynamic Ergodic Divertor" Special issue. *Fusion Eng. Design*, **37**, 335-450.

Abdullaev, S.S. and Finken, K.H. (1998) "Widening the magnetic footprints in a poloidal divertor tokamak: a proposal", *Nuclear Fusion*, **38**, 531 - 544.

Abdullaev, S.S., Zaslavsky, G.M. (1995b) "Self-similarity of stochastic magnetic field lines near the X-point", *Phys. Plasmas* **2**, 4533- 4540.

Abdullaev, S.S., Zaslavsky, G.M. (1996) "Application of the separatrix map to study perturbed field lines near the separatrix", *Phys. Plasmas* **3**, 516-528.

Abdullaev, S.S., Finken, K.H., Kaleck, A., and Spatschek, K.H. (1998) "Twist mapping for the dynamics of magnetic field lines in a tokamak ergodic divertor", *Phys. Plasmas*, **5**, 196-210.

Abdullaev, S.S., Finken, K.H., and Spatschek, K.H. (1999) "Asymptotical and Mapping Methods in Study of Ergodic Divertor Magnetic Field in a Toroidal System", *Phys. Plasmas*, **6**, 153-174.

Abdullaev, S.S. (1999) "A new integration method of Hamiltonian systems by symplectic maps", *J. Phys. A: Math. & Gen.*, **32**,2745- 2766.

Abdullaev, S.S. (2002) "The Hamilton-Jacobi method and Hamiltonian maps", *J. Phys. A: Math. & Gen.*, **35**, 2811-2832.

Abdullaev, S.S., Eich, Th., Finken, K.H. (2001) "Fractal structure of the magnetic field in the laminar zone of the Dynamic Ergodic Divertor of the Torus Experiment for Technology-Oriented Research (TEXTOR-94)", *Phys. Plasmas*, **8**, 2739-2749.

Abdullaev, S.S., Finken, K.H., Jakubowski, M., Kasilov, S.V., Kobayashi, M., Reiser, D., Reiter, D., Runov, A.M., and Wolf, R., (2003) "Overview of magnetic structure induced by the TEXTOR-DED and the related transport", *Nuclear Fusion*, **43**, 299-313.

Abdullaev, S.S. (2004) "On mapping models of field lines in a stochastic magnetic field", *Nuclear Fusion*, **44**, S12-S27.

Abdullaev, S.S., Finken, K.H., Jakubowski, M., Lehnen, M., (2006) "Mappings of stochastic field lines in poloidal divertor tokamaks", *Nuclear Fusion*, (to be published).

Abramowitz, M. and Stegun, I. (Eds.), *Handbook on Mathematical Functions*, (Dover Publ., New York, 1965).

Ali, H., Punjabi, A., Ali, H., Boozer, A.H., and Evans, T. (2004) "The low MN map for single–null divertor tokamaks", *Phys. Plasmas*, **11**, 1908-1919.

Arnold, V.I., (1989) *Mathematical methods of classical mechanics*, (Springer-Verlag: Berlin).

Balescu, R. (1988) *Transport processes in plasmas*, (North–Holland, Amsterdam).

Bleher, S., Ott, E., and Grebogi, C. (1989) "Routes to chaotic scattering" *Phys. Rev. Lett.*, **63**, 919-922.

Bleher, S., Grebogi, C., and Ott, E., (1990) "Bifurcation to chaotic scattering", *Physica*, **D 46**, 87-121.

Boozer, A.H. (1983) "Evaluation of the structure of ergodic zone", *Phys. Fluids*, **26**, 1288-1291.

Boozer, A.H. (1992) *Plasma confinement*, in "Encyclopedia of Physical Science and Technology" (Academic Press, New York), vol. 13.

Caldas, I.L, Pereira, J.M., Ullmann, K., Viana, R.L. (1996) "Magnetic field line mappings for a tokamak with ergodic limiters", *Chaos, Solitons and Fractals*, **7**, 991-1010.

Caldas, I.L., Viana, R.L., Araujo, M.S., et.al. (2002) "Control of chaotic magnetic fields in tokamaks", *Braz. J. Phys.*, **32**, 980-1004.

Cary, J.R. and Littlejohn, R.G. (1983) "Noncanonical Hamiltonian mechanics and its applications to magnetic field line flow", *Annals of Physics* (N.Y.) **151**, 1-34.

Chirikov, B.V. (1979) "A universal instability of many-dimensional oscillator", *Physics Reports*, **52**, 265-379.

Da Silva, E.C., Caldas, I.L., and Viana, R.L. (2001a) "Field line diffusion and loss in a tokamak with an ergodic magnetic limiter", *Phys. Plasmas*, **8**, 2855-2865.

Da Silva, E.C., Caldas, I.L., and Viana, R.L. (2001b) "The structure of chaotic magnetic field lines in a tokamak with the external non-symmetric magnetic perturbations", *IEEE Trans. on Plasma Science*, **29**, 617-631.

da Silva, E.C., Caldas, I.L., Viana, R.L., and Sanjuán, M.A.F. (2002) "Escape patterns, magnetic footprints, and homoclinic tangles due to ergodic magnetic limiter", *Phys. Plasmas*, **9**, 4917-4928.

da Silva, E.C., Caldas, I.L., Viana, R.L., and Sanjuán, M.A.F. (2002) "Escape patterns, magnetic footprints, and homoclinic tangles due to ergodic magnetic limiter", *Phys. Plasmas*, **9**, 4917-4928.

de Rover, M., Lopes Cardozo, N.J., and Montvai, A. (1996) "Motion of relativistic particles in axially symmetric and perturbed magnetic fields in a tokamak", *Phys. Plasmas*, **3**, 4478-4488.

Eckhard, B., (1988) "Irregular scattering", *Physica*, **D 33**, 89 -98.

Eich, Th., Finken, K.H., Kaleck, A. (1998) "Modelling efforts on the helical near field divertor of the Dynamic Ergodic Divertor (DED) for TEXTOR", *Contrib. to Plasma Physics*, **38**, 112-117.

Eich, Th., Reiser, D., and Finken, K.H. (2000) "Two dimensional modeling approach to transport properties of the TEXTOR-DED laminar zone", *Nucl. Fusion*, **40**, 1757-1772.

Engelhardt, W. and Feneberg, W., (1978) "Influence of an ergodic magnetic limiter on the impurity content in a tokamak", *J. Nucl. Mater.* **76 & 77**, 518-520.

Evans, T., J. S. Degrassie, H. R. Garner, A. W. Leonard, N. Ohyabu and L. S. Peranich ICRF, NBI, JIPP T-IIU Operation Groups, A. Mohri, Y. Hamada, K. Ida et al. (1989), *J. Nucl. Mater.*, "Resonant helical divertor experiments in ohmic and auxiliary heated JIPP T-IIU plasmas" **162 & 164**, 636-642.

Evans, T., Moyer, R.A., and Monat, P. (2002) "Modeling of stochastic magnetic flux loss from the edge of a poloidally diverted tokamak", *Phys. Plasmas* **9**, 4957-4967.

Evans, T., Moyer, R.A., Thomas, P.R., et.al. (2004) "Suppression of large edge-localized modes in high-confinement DIII-D plasmas with a stochastic magnetic boundary", *Phys. Rev. Lett.*, **92**, 235003.

Evans, T., Moyer, R.A., Watkins, J.G., et.al. (2005a) "Suppression of large edge localized modes with edge resonant magnetic fields in high confinement DIII-D plasmas", *Nuclear Fusion*, **45**, 595-607.

Evans, T., Roeder, R.K.W., Carter, J.A., et. al. (2005b) "Experimental signatures of homoclinic tangles in poloidally diverted tokamaks", *J. Phys.: Conf. Series*, **7**, 174–190.

Fedoryuk, M.V., *Asymptotic methods in analysis*, in Encyclopedia of Mathematical Sciences", v.13 (Springer-Verlag: Berlin, 1989), pp. 83-192.

Feng, Y., Sardei, F., Grigull, P., McCormick, K., Kisslinger, J., Reiter, D., and Igitkhanov, Y. (2002) "Transport in island divertors: physics, 3D modelling and comparison to first experiments on W7-AS", *Plasma Phys. Control. Fusion*, **44**, 611-625.

Feneberg, W., and Wolf, G.H. (1981) "A helical magnetic limiter for boundary-layer control in large tokamaks", *Nucl. Fusion* **21**, 669-676.

Finken, K.H., Fuchs, G., Giesen, B., Hassler, M., Koch, R., Mank, G., Nicolai, A., Rogister, A., Tokar, M.Z., van Niewenhove, R., van Oost, G., and Wolf,G.H. (1995) "A scheme for a dynamic ergodic divertor in TEXTOR", *J. Nucl. Materials*, **220-222**, 448-451.

Finken, K.H. and Wolf, G.H. (1997) "Background, motivation, concept and scientific aims for building a dynamic ergodic divertor", *Fusion Eng. Design*, **37**, 337-340.

Finken, K.H., Eich, Th., and Kaleck, A. (1998) "First Modelling of the TEXTOR DED Near Field Divertor", *Nucl. Fusion*, **38**, 515-529.

Finken, K.H., Abdullaev, S.S., Kaleck, A., and Wolf, G.H., (1999) "Operating Space of the Dynamic Ergodic Divertor for TEXTOR-94", *Nuclear Fusion*, **39**, 637-661.

Finken, K.H., Abdullaev, S.S., Biel, W. et.al. (2004) "The dynamic ergodic divertor in the TEXTOR tokamak: plasma response to dynamic helical

magnetic field perturbations", *Plasma Phys. Control. Fusion*, **46**, B143-B155.

Finken, K.H., Abdullaev, S., Biel, W., de Bock, M.F.M., Brezinsek, S., et. al. (2006), "Overview of experiments with the Dynamic Ergodic Divertor on TEXTOR", *Contribution to Plasma Physics*, 2006 (submitted).

Fischer, O. and Cooper, W.A. (1998) "Mapping of a stochastic magnetic field in toroidal systems", *Plasma Phys. Reports*, **24**, 727 - 731.

Gentle, K.W., (1981) "The Texas experimental tokamak (TEXT) facility", *Nucl. Technol. Fusion*, **1**, 479.

Ghendrih,Ph., Capes, H., Nguyen, J., Samain, A., (1992) "Control of the edge transport with the Ergodic Divertor", *Contrib. to Plasma Physics*, **32**, 179-191.

Ghendrih Ph., Grossman A., Capes H, (1996) "Theoretical and experimental investigations of stochastic boundaries in tokamaks", *Plasma Phys. Control. Fusion*, **38**, 1653-1724.

Gourdon, C., (1970) Report IPP P12 483, Garching, Oktober (translated by J.Eisert).

Hattori, K., Seike,Y., Yoshida, Z., Hamaguchi, S., Yamada, H., Suzuki,N., Itami, K.,, Kamada, Y., Inoue, N., and Uchida, T. (1984), "Shrinkage of tokamak current channel by external ergodization", *J. Nucl. Mater.*, **121**, 368-373.

Jackson, G.L., Anderson, P.M., Bialek, J., et.al. (2003) "Initial results from the new internal magnetic field coils for resistive wall mode stabilization in the DIII-D tokamak", *30th EPS Conference on Contr. Fusion and Plasma Phys.,* St. Petersburg, 7-11 July 2003 ECA Vol. 27A, P-4.47.

Jakubowski, M., Abdullaev, S.S., Finken, K.H., and TEXTOR Team, (2004) "Modelling of the magnetic field structures and first measurements of heat fluxes for TEXTOR-DED operation", *Nuclear Fusion*, **44**, S1-S11.

Jakubowski. M.W., Abdullaev, S.S., Finken, K.H., Lehnen, M., and the TEXTOR team (2005a) "Heat deposition patterns on the target plates dynamic ergodic divertor", *Journal of Nuclear Materials*, **337-339**, 176-180.

Jakubowski. M.W., Schmitz, O., Abdullaev, S.S., Brezinsek, S., Finken, K.H., Krämer-Flecken, A., Lehnen, M., Samm, U., Spatschek, K.H., Unterberg, B., Wolf, R.C. (2005b) "Effect of the change in magnetic field topology due to an ergodic divertor on the plasma structure and transport", *Phys. Rev. Lett*, submitted.

Kadomtsev, B.B., (1988) *Collective phenomena in plasmas*, 2-nd Ed. (Nauka, Moscow) (in Russian).

Kaleck, A., Hassler, M., and Evans, T. (1997) "Ergodization of the magnetic field at the plasma edge by the dynamic ergodic divertor", *Fusion Eng. Design*, **37**, 353-378.

Kaleck, A. (1999) "On island formation in a locally perturbed tokamak equilibrium", *Contrib. to Plasma Physics*, **39**, 367-379.

Karger, F., Wobig, H., Corti, S., Gernhardt, J., Klüber, O., Lisitano, G., McCormick, K., Meisel, D., and Sesnic, S., "Influence of resonant helical

fields on tokamak discharges", *Proc. 5th IAEA Int. Conf. on Plasma Phys. Control. Fusion* (Tokyo, 1974), (IAEA, Vienna, 1975), IAEA-CN-33/PD-2, vol.1, pp.207-213.

Kasilov, S.V., Moiseenko, V.E., and Heyn, M.F. (1997) "Solution of the drift kinetic equation in the regime of weak collisions by stochastic mapping techniques", *Phys.Plasmas*, **4**, 2422-2435.

Kawamura, T., Abe, Y., and Tazima, T., (1982) "Formation of magnetic islands and ergodic magnetic layers in wall-lapping plasma as a non-divertor concept for a reactor - relevant tokamak", *J. Nuclear Mater.*, **111-112**, 268-273.

Kikuchi, Y., Uesugi, Y., Takamura, S., and Elfimov, A.G., (2004) "Direct observation of tokamak plasma responses to the externally applied rotating helical magnetic field in the small tokamak HYBTOK-II", *Nuclear Fusion*, **44**, S28-S36.

Kobayashi, M., Tuda, T., Tashiro, K., Zhai, K., and Takamura, S., (2000a) "Interaction of externally applied rotating helical field with tokamak plasma", *Nuclear Fusion*, **40**, 181-193.

Kobayashi, M., Kojima, H., Zhai, K., and Takamura, S., (2000b) "Frequency dependence of tokamak plasma response to the externally applied rotating helical field", *Phys. Plasmas*, **7**, 3288-3300.

Lehnen, M., Abdullaev, S., Biel, W., de Bock, M.F.M., S. Brezinsek, C. Busch, I. Classen, K. H. Finken, M. von Hellermann, S. Jachmich, M. Jakubowski, R. Jaspers, H.R. Koslowski, A. Krämer-Flecken, Y. Kikuchi, Y. Liang, A. Nicolai, A. Pospieszczyk, T. Van Rompuy, U. Samm, O. Schmitz, G. Sergienko, B. Unterberg, R. Wolf, O. Zimmermann and the TEXTOR team, (2005) "Transport and divertor properties of the dynamic ergodic divertor", *Plasma Phys. Contr. Fusion*, **47**, B237-B248.

Lichtenberg, A.J. and Lieberman, M.A. (1992) *Regular and Stochastic Motion* 2-nd Ed. (Springer, New York).

McCool, S.C., Wootton, A.J., Kotschenreuther, M., Aydemir, A.Y., Bravenec, R.V., DeGrassie, J.S., Evans, T.E., Hickok, R.L., Richards, B., Rowan, W.L., and Schoch, P.M. (1990) "Particle transport studies with the applied resonant fields on TEXT", *Nuclear Fusion*, **30**, 167- 173

Martin, T.J., Taylor, J.B. (1984) "Ergodic behavior in a magnetic limiter ", *Plasma Phys. Contr. Fusion*, **26**, 321-334.

de Michelis, C., Grosman, A., Garbet, X., et al., (1995) "Characteristics of Ergodic Divertor Plasmas in the TORE SUPRA Tokamak", *Nucl. Fusion*, **35**, 1133-1153.

Montvai, A., and Düchs, D.F. (1993) in *Proc. Physics Computing'92. Prague, 1992* (World Scientific: Singapore) p. 417.

Morozov, A.I. and Solov'ev, L.S., (1966) "The structure of magnetic field", in *Reviews of Plasma Physics*, edited by M.A. Leontovich (Consultants Bureau, New York), Vol. 2, pp. 1-101.

Morrison, P.J. (2000) "Magnetic field lines, Hamiltonian dynamics, and nontwist systems", *Phys. Plasmas*, **7**, 2279 - 2289.

Moyer, R.A., Evans, T., Osborne, T.H., et.al. (2005) "Edge localized mode control with an edge resonant magnetic perturbations", *Physics of Plasmas*, **12**, 056119.

Nguyen, F., Ghendrih, Ph., and Samain, A. (1995) "Calculation of Magnetic Field Topology of Ergodized Zone in Real Tokamak Geometry. Application to the Tokamak TORE-SUPRA through the MASTOC Code", (CEA, Cadarache)DFRC/CAD Preprint EUR-CEA-FC-1539.

Nicolai, A., and Börner, P. (1989) "A computational model describing confinement and performance of circular and D-shaped Tokamak plasmas", *J. of Comput. Phys.*, **80**, 98-136.

Nicolai, A., (1997) "Characteristic parameters of the magnetic field due to the dynamics ergodic divertor", *Fusion Eng. Design*, **37**, 347-352.

Okabayashi, M., Bialek, J., Chance, M.S., et.al. (2001) "Active feedback stabilization of the resistive wall mode on the DIII-D device", *Phys. Plasmas*, **8**, 2071-2082.

Okabayashi, M., Bialek, J., Bondeson, A., et.al. (2004) "Control of the resistive wall mode with internal coils in the DIII-D tokamak", *Proc. 20th IAEA Fusion Energy Conference*, (Vilamoura, Portugal, 1-6 November, 2006) IAEA-CN-116/EX/3-1Ra.

Ott, E. (1993) *Chaos in Dynamical Systems* (Cambridge University Press: Cambridge). x+385.

Pires C.J.A., Saettonne, E.A.O., Kucinski, M.Y., Vannucci, A., and Viana, R.L. (2005) "Magnetic field structure in the TCABR tokamak due to ergodic limiters with a non-uniform current distribution: theoretical and experimental results", *Plasma Phys. Control. Fusion*, **47**, 1609-1632.

Portela, J.S.E., Viana, R.L., and Caldas, I.L., (2003) "Chaotic magnetic field lines in tokamaks with ergodic limiter", *Physica* A, **317**, 411-431.

Punjabi, A., Verma, A., and Boozer, A.H. (1992) "Stochastic broadening of the separatrix of tokamak divertor", *Phys. Rev. Lett.* **69**, 3322-3325.

Punjabi, A., Verma, A., and Boozer, A.H. (1994) "Tokamak divertor map", *J. Plasma Phys.* **52**, 91 - 111.

Punjabi, A., Verma, A., and Boozer, A.H. (1996) "The simple map for a single-null divertor tokamak", *J. Plasma Phys.*, **56**, 569-603.

Punjabi, A., Ali, H., and Boozer, A.H. (1997) "Symmetric simple map for a single-null divertor tokamak", *Phys. Plasmas* **4**, 337-345.

Punjabi, A., Ali, H., and Boozer, A.H. (2003) "Effects of dipole perturbation on the stochastic layer and magnetic footprint in single-null divertor tokamaks", *Phys. Plasmas* **10**, 3992-4003.

Regianni, N., Sakanaka, P.H., (1994) "The effect of the magnetic limiter current on the peripheral chaotic region of a tokamak", *Plasma Phys. Control. Fusion*, **36**, 513-522.

Roeder, R.K.W., Rapoport, B.I., and Evans, T., (2003) "Explicit calculations of homoclinic tangles in tokamaks", *Phys. Plasmas*, **10**, 3796-3799.

Runov, A.M., Reiter, D., Kasilov, S.V., Heyn, M.F., and Kernbichler, W. (2001) "Monte Carlo study of heat conductivity in stochastic boundaries: Application to the TEXTOR ergodic divertor", *Phys. Plasmas*, **8**, 916-930.

Samain, A., Grosman, A., Feneberg, W., (1982) "Plasma motion and purification in an ergodic divertor", *J. Nucl. Mater.* **111 & 112**, 408-412.

Samain, A., Grosman, A., Blenski, T., Fuchs, G, and Steffen, B., (1984) "An ergodic divertor for tore supra", *J. Nucl. Mater.* **128 & 129**, 395-399.

Samain, A., Blenski, T., Ghendrih, Ph., et al., (1990) "Theory of the Ergodic Divertor", *Contrib. to Plasma Physics*, **30**, 157-165.

Sanz-Serna, J.M. (1991) "Symplectic integrators for Hamiltonian problems: an overview", *Acta Numerica*, 243-286.

Shen, Y., Miyake, M., Takamura, S., Kuroda, T., and Okuda, T., (1989) "Ergodic magnetic limiter experiments in the HYBTOK-II tokamak", *J. Nucl. Mater.*, **168**, 295-303.

Shoji, T., Tamai, H., Miura, Y., et. al. (1992) "Effects of ergodization on plasma confinement in JFT-2M", *J. Nucl. Mater.*, **196 & 198**, 296-300.

Strait,E.J., Bialek, J., Bogatu, N., et.al. (2003) "Resistive wall stabilization of high-beta plasmas in DIII D", *Nuclear Fusion*, **43**, 430-440.

Takamura, S., Ohnishi, N. Yamada, H., and Okuda, T. (1987) "Electric and magnetic structure of an edge plasma in a tokamak with a helical magnetic limiter", *Phys. Fluids*, **30**, 144-147.

Takamura, S., Yamada, H., and Okuda, T. (1988) "Control of the tokamak edge plasma by static and rotating helical magnetic limiters", *Nuclear Fusion*, **28**, 183-191.

Takamura, S., Shen, Y., Yamada, H., Miyake, M., Tamakoshi, T., and Okuda, T. (1989), "Electric and magnetic structure of tokamak edge plasma with static and rotating helical magnetic limiter", *J. Nucl. Mater.*, **162-164**, 643-647.

Tel, T. and Ott, E., (1993) "Chaotic Scattering: An Introduction", *Chaos*, **3**, 417 - 426.

Tongue, B.H. (1987) "On obtaining global nonlinear system characteristics through interpolated cell mapping", *Physica* D, **28**, 401-408.

Ullmann, K. and Caldas, I.L., (2000) "A symplectic mapping for the ergodic magnetic limiter and its dynamical analysis", *Chaos, Solitons and Fractals*, **11**, 2129 - 2140.

Unterberg, B., Abdullaev, S.S., Brezinsek, S., Busch, C., Finken, K.H., Harting, D., Jakubowski, M., et. al. (2004) "The impact of the Dynamic Ergodic Divertor on transport and plasma edge structure in the tokamak TEXTOR", Proc. 20th IAEA Fusion Energy Conference, (01-06 November 2004, Volamoura, Portugal). (IAEA, Vienna, 2004) EX/P5-33.

Viana, R.L. and Caldas, I.L., (1992) "Peripheral stochasticity in tokamak with an ergodic magnetic limiter", *Z. Naturforsch.* **47a**, 941 - 944.

Viana, R.L. and Vasconcelos, D.B, (1997) "Field-line stochasticity in tokamak with an ergodic magnetic limiter", *Dynamics Stability Systems*, **12**, 75.

Viana, R.L., (2000) "Chaotic magnetic field lines in a tokamak with resonant helical windings", *Chaos, Solitons and Fractals*, **11**, 765-778.

Wesson J., (2004) *Tokamaks*, 3-rd Edition, Oxford Engineering Science Series: **48**, (Clarendon Press: Oxfor).

Wolf, R.C., Biel, W., de Bock, M.F.M., Finken, K.H., Günter, S., Hogeweij, G. M. D., Jakubowski, M., et.al. (2005) "Effect of the Dynamic Ergodic Divertor in the TEXTOR Tokamak on MHD Stability, Plasma Rotation and Transport", *Nuclear Fusion* (submitted).

Yamagishi, T. (1995) "Evaluation of the stochastic layer near separatrix in toroidal divertor", *Fusion Technology*, **27**, 505-508.

Zehrfeld, H. P. (1999) private communication.

Schriften des Forschungszentrums Jülich
Reihe Energietechnik / Energy Technology

1. **Fusion Theory**
   Proceedings of the Seventh European Fusion Theory Conference
   edited by A. Rogister (1998); X, 306 pages
   ISBN: 3-89336-219-3

2. **Radioactive Waste Products 1997**
   Proceedings of the 3rd International Seminar on Radioactive Waste Products
   held in Würzburg (Germany) from 23 to 26 June 1997
   edited by R. Odoj, J. Baier, P. Brennecke et al. (1998), XXIV, 506 pages
   ISBN: 3-89336-225-8

3. **Energieforschung 1998**
   Vorlesungsmanuskripte des 4. Ferienkurs „Energieforschung“
   vom 20. bis 26. September 1998 im Congrescentrum Rolduc und
   im Forschungszentrum Jülich
   herausgegeben von J.-Fr. Hake, W. Kuckshinrichs, K. Kugeler u. a. (1998),
   500 Seiten
   ISBN: 3-89336-226-6

4. **Materials for Advances Power Engineering 1998**
   Abstracts of the 6th Liège Conference
   edited by J. Lecomte-Beckers, F. Schubert, P. J. Ennis (1998), 184 pages
   ISBN: 3-89336-227-4

5. **Materials for Advances Power Engineering 1998**
   Proceedings of the 6th Liège Conference
   edited by J. Lecomte-Beckers, F. Schubert, P. J. Ennis (1998),
   Part I XXIV, 646, X pages; Part II XXIV, 567, X pages; Part III XXIV, 623, X
   pages
   ISBN: 3-89336-228-2

6. **Schule und Energie**
   1. Seminar Energiesparen, Solarenergie, Windenergie. Jülich, 03. und
   04.06.1998
   herausgegeben von P. Mann, W. Welz, D. Brandt, B. Holz (1998), 112 Seiten
   ISBN: 3-89336-231-2

7. **Energieforschung**
   Vorlesungsmanuskripte des 3. Ferienkurses „Energieforschung“
   vom 22. bis 30. September 1997 im Forschungszentrum Jülich
   herausgegeben von J.-Fr. Hake, W. Kuckshinrichs, K. Kugeler u. a. (1997),
   505 Seiten
   ISBN: 3-89336-211-8

8. **Liberalisierung des Energiemarktes**
   Vortragsmanuskripte des 5. Ferienkurs „Energieforschung“
   vom 27. September bis 1. Oktober 1999 im Congrescentrum Rolduc und
   im Forschungszentrum Jülich
   herausgegeben von J.-Fr. Hake, A. Kraft, K. Kugeler u. a. (1999), 350 Seiten
   ISBN: 3-89336-248-7

9. **Models and Criteria for Prediction of Deflagration-to-Detonation Transition (DDT) in Hydrogen-Air-Steam-Systems under Severe Accident Conditions**
   edited by R. Klein, W. Rehm (2000), 178 pages
   ISBN: 3-89336-258-4

10. **High Temperature Materials Chemistry**
    Abstracts of the 10th International IUPAC Conference, April 10 - 14 2000, Jülich
    edited by K. Hilpert, F. W. Froben, L. Singheiser (2000), 292 pages
    ISBN: 3-89336-259-2

11. **Investigation of the Effectiveness of Innovative Passive Safety Systems for Boiling Water Reactors**
    edited by E. F. Hicken, K. Verfondern (2000), X, 287 pages
    ISBN: 3-89336-263-0

12. **Zukunft unserer Energieversorgung**
    Vortragsmanuskripte des 6. Ferienkurs „Energieforschung“
    vom 18. September bis 22. September 2000 im Congrescentrum Rolduc und
    im Forschungszentrum Jülich
    herausgegeben von J.-Fr. Hake, S. Vögele, K. Kugeler u. a. (2000),
    IV, 298 Seiten
    ISBN: 3-89336-268-1

13. **Implementing Agreement 026**
    For a programme of research, development and demonstration on advances fuel cells
    Fuel Cell Systems for Transportation
    Annex X. Final Report 1997 - 1999
    edited by B. Höhlein; compiled by P. Biedermann (2000), 206 pages
    ISBN: 3-89336-275-4

14. **Vorgespannte Guß-Druckbehälter (VGD) als berstsichere Druckbehälter für innovative Anwendungen in der Kerntechnik**
    Prestressed Cast Iron Pressure Vessels as Burst-Proof Pressure Vessels for Innovative Nuclear Applications
    von W. Fröhling, D. Bounin, W. Steinwarz u. a. (2000) XIII, 223 Seiten
    ISBN: 3-89336-276-2

Schriften des Forschungszentrums Jülich
Reihe Energietechnik / Energy Technology

15. **High Temperature Materials Chemistry**
Proceedings of the 10th International IUPAC Conference
held from 10 to 14 April 2000 at the Forschungszentrum Jülich, Germany
Part I and II
edited by K. Hilpert, F. W. Froben, L. Singheiser (2000), xvi, 778, VII pages
ISBN: 3-89336-259-2

16. **Technische Auslegungskriterien und Kostendeterminanten von SOFC- und PEMFC-Systemen in ausgewählten Wohn- und Hotelobjekten**
von S. König (2001), XII, 194 Seiten
ISBN: 3-89336-284-3

17. **Systemvergleich: Einsatz von Brennstoffzellen in Straßenfahrzeugen**
von P. Biedermann, K. U. Birnbaum, Th. Grube u. a. (2001), 185 Seiten
ISBN: 3-89336-285-1

18. **Energie und Mobilität**
Vorlesungsmanuskripte des 7. Ferienkurs „Energieforschung“
vom 24. September bis 28. September 2001 im Congrescentrum Rolduc und im Forschungszentrum Jülich
herausgegeben von J.-Fr. Hake, J. Linßen, W. Pfaffenberger u. a. (2001),
205 Seiten
ISBN: 3-89336-291-6

19. **Brennstoffzellensysteme für mobile Anwendungen**
von P. Biedermann, K. U. Birnbaum, Th. Grube u. a. (2002)
PDF-Datei auf CD
ISBN: 3-89336-310-6

20. **Materials for Advances Power Engineering 2002**
Abstracts of the 7th Liège Conference
edited by J. Lecomte-Beckers, M. Carton, F. Schubert, P. J. Ennis (2002),
c. 200 pages
ISBN: 3-89336-311-4

21. **Materials for Advances Power Engineering 2002**
Proceedings of the 7th Liège Conference
Part I, II and III
edited by J. Lecomte-Beckers, M. Carton, F. Schubert, P. J. Ennis (2002),
XXIV, 1814, XII pages
ISBN: 3-89336-312-2

22. **Erneuerbare Energien: Ein Weg zu einer Nachhaltigen Entwicklung?**
Vorlesungsmanuskripte des 8. Ferienkurs „Energieforschung“
vom 23. bis 27. September 2002 in der Jakob-Kaiser-Stiftung, Königswinter
herausgegeben von J.-Fr. Hake, R. Eich, W. Pfaffenberger u. a. (2002),
IV, 230 Seiten
ISBN: 3-89336-313-0

23. **Einsparpotenziale bei der Energieversorgung von Wohngebäuden durch Informationstechnologien**
    von A. Kraft (2002), XII, 213 Seiten
    ISBN: 3-89336-315-7

24. **Energieforschung in Deutschland**
    Aktueller Entwicklungsstand und Potentiale ausgewählter nichtnuklearer Energietechniken
    herausgegeben von M. Sachse, S. Semke u. a. (2002), II, 158 Seiten, zahlreiche farb. Abb.
    ISBN: 3-89336-317-3

25. **Lebensdaueranalysen von Kraftwerken der deutschen Elektrizitätswirtschaft**
    von A. Nollen (2003), ca. 190 Seiten
    ISBN: 3-89336-322-X

26. **Technical Session: Fuel Cell Systems of the World Renewable Energy Congress VII**
    Proceedings
    edited by D. Stolten and B. Emonts (2003), VI, 248 pages
    ISBN: 3-89336-332-7

27. **Radioactive Waste Products 2002 (RADWAP 2002)**
    Proceedings
    edited by R. Odoj, J. Baier, P. Brennecke and K. Kühn (2003), VI, 420 pages
    ISBN: 3-89336-335-1

28. **Methanol als Energieträger**
    von B. Höhlein, T. Grube, P. Biedermann u. a. (2003), XI, 109 Seiten
    ISBN: 3-89336-338-6

29. **Hochselektive Extraktionssysteme auf Basis der Dithiophosphinsäuren: Experimentelle und theoretische Untersuchungen zur Actinoiden(III)-Abtrennung**
    von S. A. H. Nabet (2004), VI, 198 Seiten
    ISBN: 389336-351-3

30. **Benchmarking-Methodik für Komponenten in Polymerelektrolyt-Brennstoffzellen**
    von Matthias Gebert (2004), 194 Seiten
    ISBN: 3-89336-355-6

31. **Katalytische und elektrochemische Eigenschaften von eisen- und kobalthaltigen Perowskiten als Kathoden für die oxidkeramische Brennstoffzelle (SOFC)**
    von Andreas Mai (2004), 100 Seiten
    ISBN: 3-89336-356-4

32. **Energy Systems Analysis for Political Decision-Making**
edited by J.-Fr. Hake, W. Kuckshinrichs, R. Eich (2004), 180 pages
ISBN: 3-89336-365-3

33. **Entwicklung neuer oxidischer Wärmedämmschichten für Anwendungen in stationären und Flug-Gasturbinen**
von R. Vaßen (2004), 141 Seiten
ISBN: 3-89336-367-X

34. **Neue Verfahren zur Analyse des Verformungs- und Schädigungsverhaltens von MCrAlY-Schichten im Wärmedämmschichtsystem**
von P. Majerus (2004), 157 Seiten
ISBN: 3-89336-372-6

35. **Einfluss der Oberflächenstrukturierung auf die optischen Eigenschaften der Dünnschichtsolarzellen auf der Basis von a-Si:H und µc-Si:H**
von N. Senoussaoui (2004), 120 Seiten
ISBN: 3-89336-378-5

36. **Entwicklung und Untersuchung von Katalysatorelementen für innovative Wasserstoff-Rekombinatoren**
von I.M. Tragsdorf (2005), 119 Seiten
ISBN: 3-89336-384-X

37. **Bruchmechanische Untersuchungen an Werkstoffen für Dampfkraftwerke mit Frischdampftemperaturen von 500 bis 650°C**
von L. Mikulová (2005), 149 Seiten
ISBN: 3-89336-391-2

38. **Untersuchungen der Strukturstabilität von Ni-(Fe)-Basislegierungen für Rotorwellen in Dampfturbinen mit Arbeitstemperaturen über 700 °C**
von T. Seliga (2005), 106 Seiten
ISBN: 3-89336-392-0

39. **IWV-3 Report 2005. Zukunft als Herausforderung**
(2005), 115 Seiten
ISBN: 3-89336-393-9

40. **Integrierter Photodetektor zur Längenmessung**
von E. Bunte (2005), XI, 110 Seiten
ISBN: 3-89336-397-1

41. **Microcrystalline Silicon Films and Solar Cells Investigated by Photoluminescence Spectroscopy**
by T. Merdzhanova (2005), X, 137 Seiten
ISBN: 3-89336-401-3

Schriften des Forschungszentrums Jülich
Reihe Energietechnik / Energy Technology

42. **IWV-3 Report 2005. Future as a challenge**
(2005), 115 Seiten
ISBN: 3-89336-405-6

43. **Electron Spin Resonance and Transient Photocurrent Measurements on Microcrystalline Silicon**
by T. Dylla (2005), X, 138 Seiten
ISBN: 3-89336-410-2

44. **Simulation und Analyse des dynamischen Verhaltens von Kraftwerken mit oxidkeramischer Brennstoffzelle (SOFC)**
von M. Finkenrath (2005), IV, 155 Seiten
ISBN: 3-89336-414-5

45. **The structure of magnetic field in the TEXTOR-DED**
by K.H. Finken, S.S. Abdullaev, M. Jakubowski, M. Lehnen, A. Nicolai, K.H. Spatschek (2005), 113 Seiten
ISBN: 3-89336-418-8

46. **Entwicklung und Modellierung eines Polymerelektrolyt-Brennstoffzellenstapels der 5 kW Klasse**
von T. Wüster (2005), 211 Seiten
ISBN: 3-89336-422-6

Forschungszentrum Jülich
in der Helmholtz-Gemeinschaft

Band/Volume 45
ISBN 3-89336-418-8

Energietechnik
Energy Technology